

Quantum stochastic phase-space theorems lead to hidden causal loops in a model for measurement consistent with macroscopic realism, Bell nonlocality and no-signalling

M. D. Reid and P. D. Drummond

*Centre for Quantum Science and Technology Theory,
Swinburne University of Technology, Melbourne 3122, Australia*

While Bell nonlocality can be explained through mechanisms such as retrocausality, it is not clear the extent to which any such theory is fully equivalent to quantum theory. It is also not clear why such mechanisms do not manifest macroscopically, and whether macroscopic realism (arguably a requirement for causality at an everyday level) holds. In this paper, we show how quantum measurement and nonlocality can be explained consistently with macroscopic realism and no-signaling. We analyze a measurement \hat{x} on a system prepared in a superposition of eigenstates $|x_j\rangle$ of \hat{x} , with measurement modeled as amplification of \hat{x} , realized by interacting the system with an amplifier for a time t . More generally, we consider measurement of $\hat{x}_\theta = \hat{x} \cos \theta + \hat{p} \sin \theta$. Deriving quantum stochastic path-integral theorems, we prove an equivalence between a phase-space probability distribution $Q(x, p, t)$ (which uniquely represents the quantum state) and stochastic trajectories for the amplified and attenuated variables, x and p , that propagate backwards and forwards in time, respectively. The sampling for x is determined by a future boundary condition. For the superposition, but not the mixture, the backward- and forward- propagating trajectories are connected by the initial-time conditional distribution $Q(p|x)$, leading to a causal loop. The joint densities for $x(t)$ and $p(t)$ yield $Q(x, p, t)$, confirming causal consistency, a prediction that can be experimentally tested. A feature is “hidden” noise associated with an eigenstate. Unlike the eigenvalue x_j , this noise is not amplified. This motivates an ontological model for measurement, where the amplified amplitude $x(t)$ gives the detected outcome, from which Born’s rule follows. For macroscopic superpositions of $|x_j\rangle$, we demonstrate consistency with macroscopic realism: the outcome for \hat{x} is considered a real property, as given by a variable λ_x , prior to measurement (if measurement settings θ remain invariant). Further, we evaluate the initial-time distribution $Q_{loop}(x, p, 0|x_j)$ for the coupled trajectories conditioned on the given outcome x_j , showing that this cannot correspond to any quantum state $|\psi\rangle$. The eigenstate $|x_j\rangle$ is retrieved, when information about p is lost. Finally, we analyze Einstein-Podolsky-Rosen and Bell nonlocality, where the setting θ is adjusted. Our conclusion is a model for the collapse of the wave-function and nonlocality, consistent with three “weak” local realistic premises. We deduce a hybrid causal structure involving causal relations for amplified variables, along with “hidden” causal loops and feedback for unobservable quantities, demonstrating through an explicit simulation how a microscopic retrocausality can explain measurement and entanglement, without leading to retrocausality at an observable, macroscopic level.

I. INTRODUCTION

All local, strictly causal hidden variable theories are falsifiable, since quantum predictions and experiments lead to a violation of Bell inequalities [1–4]. However, it is known that violations of Bell inequalities can indeed arise using the advanced solutions of classical electrodynamics [5–8]. Classical electrodynamics with future boundary conditions has been widely studied [9–14], and is essential to the theory of radiating fields. Following from Bohr [15] who considered delayed-choice experiments [16], Wheeler speculated that retrocausality due to future boundary conditions may explain quantum paradoxes [17, 18]. Bell’s work also motivated the question of potential superluminal disturbances, leading to no-signaling theorems [19]. These results have inspired analyses of causality in quantum physics [16, 20–77].

Studies of causal structure are closely related to studies of realism in quantum mechanics. Classical models assume real properties that describe the system at a given time; retrocausality allows these properties to be influenced by future events. Proposals to explain Bell violations and wave-function collapse include superluminal

causal influences [78–83], retrocausality [5, 8, 28, 29, 47, 84–89] cyclic causation [90, 91] and unobservable loops [92–94], or super-determinism [95] – but an open question is why then are such mechanisms not apparent at a macroscopic level? Causal models based on superluminal or retrocausal mechanisms require a fine-tuning of parameters in order to explain no-signaling, which seemed undesirable [53, 54, 56]. The fine-tuning is not always a problem however, and no-signaling does not rule out retrocausal or cyclic causation [29, 87, 90, 91].

As well as no-signaling, we argue that macroscopic realism is a natural requirement for a model complying with causality at a macroscopic level. Macroscopic realism (MR) posits that a system in a superposition of two macroscopically distinct states, “will at all times *be* in one or other of these states” [96]. In other words, at a given time, the outcome of a measurement distinguishing between the macroscopic states will be predetermined and fixed i.e. *not changed by a future event* [97]. The assumption of MR goes hand-in-hand with that of causality at a macroscopic level. Yet, Schrodinger argued that MR is inconsistent with the notion that quantum mechanics is a complete description of reality (“readings”)

[98]: If the macroscopic outcome is predetermined, then it is not apparent what “state” the system is in. Quantum causal models have been developed to address these problems [57, 58, 60–64, 77]. It is not clear however whether one can present a unified framework combining causality and realism, and there remains the fundamental question of the level (from microscopic to macroscopic) at which causal concepts, or MR, will hold.

In this paper, we show how phase-space solutions from quantum theory lead to *probabilistic stochastic simulations of real amplitudes x and p* that may contribute to a resolution of these questions. The resolution we propose involves future boundary conditions but avoids traditional notions of retrocausality, instead leading to a “hidden” (i.e. unobservable) cyclic causation, originating from microscopic quantum noise inputs at the future boundary. The amplitudes are based on the Q function $Q(x, p)$ [99]. Following Bohr and Glauber [15, 100], we treat a measurement of an observable \hat{x} as an amplification of \hat{x} . Applying a phase-space equivalence theorem, we solve for the evolution of the system in terms of x and p . The dynamical solutions for x propagate backwards in time; those for p propagate forwards in time (Fig. 1). The theorems we derive establish a boundary condition involving a conditional constraint at the initial time. This defines a connection between the forward- and backward-propagating trajectories for systems in a superposition state, thereby giving rise to a hidden causal loop. By tracking the amplitudes in the simulations, a causal structure is revealed (Fig. 2), motivating to a model for the collapse of the wave function and the emergence of macroscopic reality. The model posits that after amplification of \hat{x} , the detected outcome *is* the amplitude $x(t)$ (as $t \rightarrow \infty$), the inferred outcome for \hat{x} being $x(t)/G$, where G is the amplification factor. Although limited to bosonic fields, the stochastic equations are derived within the framework of quantum field theory, thereby ensuring compatibility with quantum predictions.

Entanglement is also analyzed, which leads to a model for Einstein-Podolsky-Rosen (EPR) correlations and Bell nonlocality consistent with three “*weak*” *local realistic premises*. Fine-tuning is explained by the presence of the “hidden” (unobservable) noise. The weak premises are summarized as: (1) Macroscopic realism (MR): the value for the outcome of the measurement \hat{x} at A is determined (as, say, $\tilde{\lambda}_x^A$) for the system once the measurement setting is fixed and after sufficient amplification G ; (2) This value ($\tilde{\lambda}_x^A$) is not impacted by any subsequent change of setting at another spacelike-separated system B , implying consistency with no-signalling; (3) Once the value $\tilde{\lambda}_x^A$ for the outcome (as in (1)) for system A is determined, a retrocausal feedback implies restrictions on the state at B . For EPR states, the premise (3) gives a model to explain the correlation that arises between the two positions, and also between the two momenta, of separated particles, in a way that does not require both position and momentum to be predetermined simultaneously prior to the choice of measurement settings.

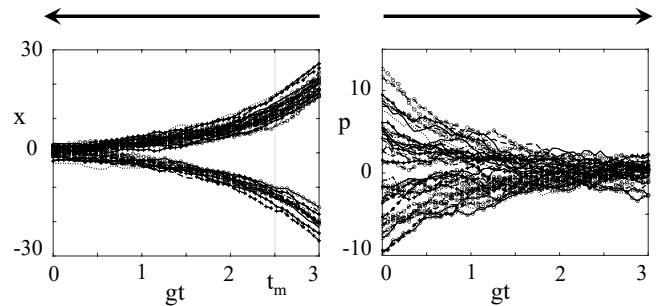


Figure 1. Stochastic solutions (simulations) showing individual trajectories for x and p modelling a measurement \hat{x} on a system prepared in a superposition $|\psi_{sup}\rangle$ (Eq. (1.1)) of eigenstates $|x_1\rangle$ and $| -x_1\rangle$ of \hat{x} . The variable x is amplified (left) and p deamplified (right). The trajectories for x propagate in the negative-time direction from a boundary condition at time $t_f = 3/g$; those for p propagate forward in time. Two branches for x are evident at time t_m . The noise $\delta x(t)$ about each branch is constant throughout the amplification, being determined by the noise inputs at the final time t_f , and contributing an unobservable “hidden” noise level. This gives a model for measurement: we assume the detected outcome is given by $x(t_f)$ ($t_f \rightarrow \infty$) in each run. The argument for consistency with macroscopic realism at time t_m is possible, because each $x(t_m)$ belongs to one or other branch, and (for each trajectory) the $x(t_f)$ traces back to a $x(t_m)$ which is on the same branch. Here, $x_1 = 0.8$, $G = e^{gt}$, $c_1 = -ic_2 = \frac{1}{\sqrt{2}}$. Refer to Sec. IV for details.

The main result of this paper is the equivalence of the quantum state, as represented by the Q function, to forward- and backward-propagating amplitudes in time, as the system evolves through the dynamics of a measurement process. This result, illustrated for both superposition and entangled states, can be experimentally tested (Fig. 3). The results of this paper also give stochastic solutions for continuous-variable EPR entanglement [101, 102], in which consistency with MR can be illustrated. Particularly relevant is the recent experiment of Colciaghi et al [103], which reported EPR correlations between macroscopic atomic clouds, for which a strong argument can be given that MR holds for the system defined after the adjustment of the settings.

Summary and Layout of paper

Forward-backward simulations: Based on earlier work [104–107], we treat quantum measurement by solving for the dynamics of a quantum phase-space distribution function $Q(x, p)$, the Q function which is positive and uniquely defines the quantum state for a single-mode boson field [99]. In this paper, the measurement problem is analyzed using *amplification*: Measurement of the quadrature phase amplitude \hat{x} of the field occurs through an interaction H_{amp} with a parametric amplifier, which amplifies \hat{x} by a factor G . This originates in Bohr’s approach of regarding measurement as amplification [15].

The dynamics is determined from the Hamiltonian H_{amp} and the equation of motion for $Q(x, p, t)$ (derived from the density operator ρ), meaning that the operator formalism of quantum mechanics is removed from the calculations (refer Sec. II).

Stochastic theorems lead from the equation of motion of $Q(x, p, t)$ to an equivalent stochastic dynamics of the amplitudes x and p (Sec. III). The path-integral theorem and stochastic equivalence theorem are derived in Appendix A. The stochastic equations for x and p are separable, with the amplified variable x propagating in the negative time direction, and the de-amplified variable p propagating in the positive time direction (Fig. 1). The equation for x is hence determined by a future boundary condition, based on the marginal distribution $Q(x, t_f)$ for the amplified variable x , where t_f is the interaction time ($t_f \rightarrow \infty$). In the simulation, part of the future boundary condition stems deterministically from the initial condition at t_1 , and a part is undetermined at t_1 , being microscopic inputs at the future time t_f (Fig. 2). The boundary condition for p is determined by the Q function $Q(x, p, t_1)$ for the state, defined at time t_1 .

The equations modeling a measurement \hat{x} on the system prepared in a superposition $|\psi_{sup}\rangle$ of eigenstates of \hat{x} are solved by simulation in Sec. IV. We also solve for superpositions of coherent states (cat states), and for the measurement of the observable \hat{p} on $|\psi_{sup}\rangle$. The solutions reveal that for a system prepared in the superposition of eigenstates $|x_j\rangle$ of \hat{x} (with probability amplitudes c_j),

$$|\psi_{sup}\rangle = \sum_j c_j |x_j\rangle, \quad (1.1)$$

the dynamics leads to *amplified* amplitudes $x(t_m)$ at t_m which are *always associated with one or other* branches, corresponding to the *eigenvalues* x_j (Fig. 1 top left).

A hidden-variable model for measurement and Born's rule: The simulations motivate a stochastic retrocausal model to explain quantum measurement and entanglement. The assumptions of this model are given in Sec. III. It is assumed that as the system is amplified, the detected outcome *is* the individual amplitude $x(t)$ (as $t \rightarrow \infty$), the inferred outcome for \hat{x} being $x(t)/G$. This is consistent with the assumption that each run of the simulation represents an individual realization. Hence, in this model, the outcomes are always *just one* of the *eigenvalues* x_j , since for each branch the amplified value Gx_j dominates over a background hidden noise level that is *not* amplified (Fig. 1). The probability of an outcome x corresponds to $Q(x, t_f)$, which gives the probability density of amplitudes $x(t_f)$. We show in Secs. II and IV that Born's rule follows naturally from this assumption. We note that the measurement dynamics results from the interaction Hamiltonian – thus requiring no special physical assumption for wave-function collapse: Our analysis is therefore compatible with Bell's requirement [108] that there should be no “split” between system and measurement apparatus. The “collapse” to the single outcome x_j

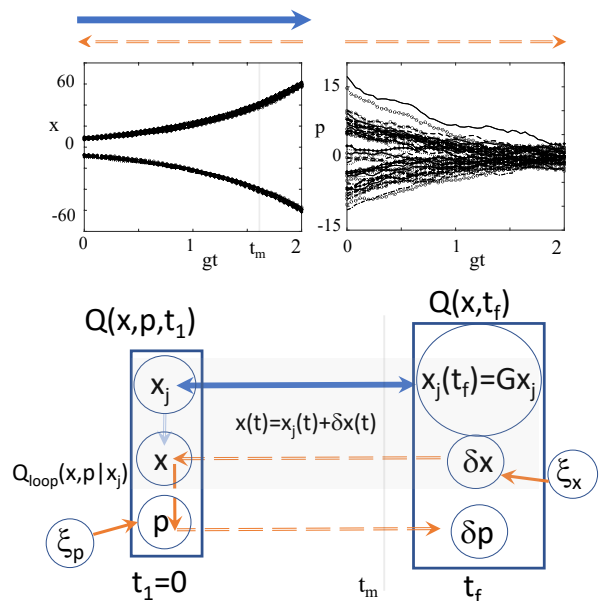


Figure 2. Causal structure: *Top*: As for Fig. 1, but with $x_1 = -x_2 = 8$ and $t_f = 2/g$. *Lower*: Diagram of the causal relations of the simulation. The Q function $Q(x, p, t_1)$ represents the quantum state $|\psi_{sup}\rangle$. A future boundary condition for x , after amplification for a time t_f . The eigenvalues $x_j \in \{x_1, -x_1\}$ correspond to the means of two Gaussian peaks in $Q(x, p, t_1)$. A deterministic relation (denoted by the solid two-way blue arrow) connects the means x_j at time t_1 to amplified values Gx_j at time t_f . Noise ξ_x and $\delta x(0)$ enters at the future time t_f ; noise ξ_p at time t_1 . The noise inputs at the future boundary are not amplified nor attenuated: the trajectory for x in the top figure hence appears as a thin exponential curve. In the measurement model, the inferred outcome for \hat{x} is $x(t_f)/G$, giving either x_1 or $-x_1$ with negligible relative error as $t_f \rightarrow \infty$. There is consistency with the assumption that the amplitude value $x(0)$ at $t = 0$ corresponds to the final value $x(t_f) \sim Gx(0)$, giving a *macroscopic causal relation* (solid blue line). The theorems derived in this paper predict feedback at the origin t_1 . This connects forward and backward trajectories to define the distribution $Q_{loop}(x, p|x_j)$, giving rise to a hidden loop (orange dashed lines). Details are given in Secs. IV and V.

is explained by a process that treats measurement as any other process.

Macroscopic realism (MR) and causal structure: It may seem counter-intuitive that a theory involving future boundary conditions (at a time t_f) can adequately describe macroscopic realism, which posits a predetermination of outcome of \hat{x} at the time $t_m < t_f$. The mechanism is explained by the causal structure of the simulation which involves noise inputs (Fig. 2). The argument for MR is given in Sec. IV. After sufficient interaction, at a time t_m , there is a one-to-one correspondence between the branch-value of $x(t_f)$ and that of $x(t_m)$ for each trajectory: There is consistency with the definition of MR: that at t_m , the value $x(t_m)$ prede-

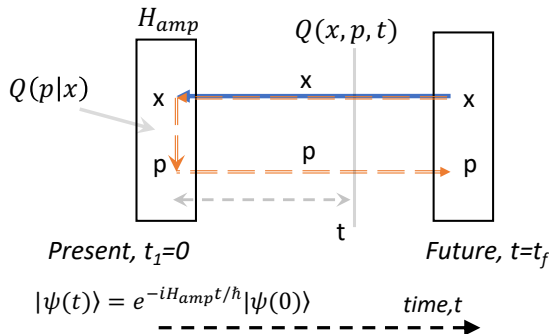


Figure 3. Test of causal consistency: How can a future boundary condition be consistent with the causal behaviour of the Q function? The diagram illustrates the equivalence of the forward-backward trajectories $p(t)$ and $x(t)$ to the Q function $Q(x, p, t)$, which defines the quantum state $|\psi(t)\rangle$. The system evolves under the amplification H_{amp} . After a time t_f , the initial Q-function evolves to $Q(x, p, t_f)$, in which $x(t)$ has been amplified. The probability density of $x(t)$ and $p(t)$ is given by $Q(x, p, t)$, and this is true for all t_f , even when t_f is increased far into the future. The question of why the state at time t does not depend on the future inputs at the time t_f (as in a Grandfather paradox) is explained by the causal structure of the simulation. An experimental test of this prediction is feasible.

terminates the final outcome, if the measurement is to be completed at time $t_f \geq t_m$: The branch is not changed by the noise inputs at the future boundary. There is no contradiction with claims that might suggest a falsification of MR (e.g. [49, 96, 97, 109–113]), since we assume here that the outcome will come from an amplification and detection of the field after t_m , with no further intervening measurements or changes of measurement settings.

Hidden causal loops: The theorems derived in this paper provide a link between the backward-propagating trajectories for x , and the forward-propagating trajectories for p . There is a microscopic feedback. The hidden loop and the mechanism for the collapse of the wave function is given in Sec. V. For the superposition (but not for the mixture of eigenstates), there is a connection between the backward and forward trajectories for x and p , to form a loop (Fig. 2). The forward trajectories in p decay to the background noise level: p is de-amplified and therefore unobservable. This provides a model for the collapse of the wave-function: In Sec. V, we show that the amplitudes of a given branch x_j propagate backwards to the origin t_1 , where they connect to certain forward-going amplitudes p . The associated distribution $Q_{loop}(x, p|x_j)$ is evaluated, and shown to be not equivalent to any quantum wave-function (Figs. 2 and 4). The eigenstate $|x_j\rangle$ associated with the outcome x_j is obtained on averaging over the unobservable variable p : There is a “collapse” to the eigenstate occurring on amplification of x , when information is lost about the complementary variable p .

Grandfather paradoxes: The main result of this

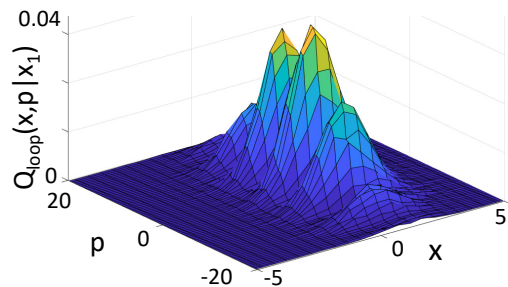


Figure 4. Test to explain how cat states are consistent with macroscopic realism: A system is prepared in the superposition $|\psi_{sup}\rangle = \frac{1}{\sqrt{2}}(|x_1\rangle + i| -x_1\rangle)$ of eigenstates $|x_j\rangle$ of \hat{x} (or else of two coherent states $|\alpha_0\rangle$ and $|-\alpha_0\rangle$). The measurement of “which state the cat is in” proceeds by amplification of \hat{x} , via H_{amp} . The Q functions before and after amplification are measurable. The simulation based on the two Q functions enables evaluation of $Q_{loop}(x, p|x_1)$, the distribution at the initial time given that the final outcome is x_1 (the positive branch for \hat{x}), by tracing the positive trajectories back from t_f (refer Fig. 2). It can be shown that $Q_{loop}(x, p, t_1)$ is not equivalent to a quantum state $|\psi\rangle$, but becomes $|x_1\rangle$ on integrating over p (refer Sec. V). However, as $|x_1| \rightarrow \infty$, $Q_{loop}(x, p, t_1)$ approaches the Q function of $|x_1\rangle$. Here, $x_1 = -x_2 = 1$.

paper is the equivalence of the forward- and backward-propagating trajectories $x(t)$ and $p(t)$ at the time t to the evolved quantum state $e^{-iH_{amp}t}|\psi(t)\rangle$, as denoted by the Q function, $Q(x, p, t)$. The dependence of the dynamics on a future boundary condition (BC) seems likely to lead to grandfather-type paradoxes. However, there is consistency with macroscopic realism (Fig. 1). This is possible because the future BC is in part deterministically linked to the initial state, and the noise inputs ξ_x and δx at the future boundary are independent of the evolution time t_f . We confirm numerically that, in the simulations, $Q(x, p, t)$ is equivalent to the joint density of $x(t)$ and $p(t)$, thus verifying *causal consistency*, as in absorber theory [8, 13, 14] and theories of closed timelike curves [114, 115] (refer Appendix B). We propose an experimental test of this prediction (Fig. 3 and Sec. X).

Schrodinger’s cat paradox: We claim that the simulations are consistent with macroscopic realism, meaning that the system at time t_m which is in a macroscopic superposition state $|\psi_{sup}\rangle = (|x_1\rangle + i| -x_1\rangle)/\sqrt{2}$ (x_1 is large) can be regarded as having a predetermined outcome, either x_1 or $-x_1$ i.e. the system in the “cat state” is *either dead or alive*. However, there is no contradiction with the paradox raised by Schrodinger [98], because the predetermined “state” of the cat given by the amplitude $x(t_m)$ does not correspond to any quantum state. This is demonstrated by the evaluation of the distributions $Q_{loop}(x, p|x_j)$ at the initial time t_1 , conditioned on the final outcome x_j where $x_j \in \{x_1, -x_1\}$: We show that each distribution $Q_{loop}(x, p|x_j)$ has associated variances for \hat{x} and \hat{p} that would violate the uncertainty relation, implying that the “states” defined by the distributions are not preparable, hence justifying the terminology of a

“hidden” causal loop. An experimental proposal is given in Fig. 4 (refer Sec. X for details).

EPR entanglement and Bell nonlocality: In Secs. VII and VIII, we present simulations for bipartite continuous-variable experiments, involving quadrature phase amplitude measurements $\hat{x}_{\theta A} = \hat{x}_A \cos \theta + \hat{p}_A \sin \theta$ and $\hat{x}_{\phi B} = \hat{x}_B \cos \phi + \hat{p}_B \sin \phi$ on two separated systems, A and B , respectively. The measurement occurs as an independent amplification of $\hat{x}_{\theta A}$ and $\hat{x}_{\phi B}$, using amplifiers H_{amp}^A and H_{amp}^B . We find that the causal model involving the microscopic “hidden” feedback (Fig. 2) can be extended to explain EPR correlations and Bell nonlocality, showing agreement with quantum predictions via the causal model presented in Sec. IX that does not conflict with Bell’s theorem.

It is assumed that at the time t_0 , the system has been physically prepared for measurement of \hat{x}_{θ} at A and \hat{x}_{ϕ} at B , so that an amplification H_{amp} at each site will complete the measurement. The system at time t_0 is described by the distribution $Q(\lambda, t_0)$ written in terms of coordinates $\lambda = (x_{\theta A}, p_{\theta A}, x_{\phi B}, p_{\phi B})$. Entanglement entails correlations between A and B as evident in $Q(\lambda, t_0)$, implying correlations in the final distribution $Q(\lambda, t_f)$ after amplification. As before, there is “hidden noise” associated with the Q function $Q(\lambda, t_0)$ that is not detectable in the outcome, $\tilde{\lambda}_{\theta}^A = x_{\theta_j}^A$ say, of the measurement $\hat{x}_{\theta A}$ at A , which is dominated by the eigenvalue $x_{\theta_j}^A$. However, tracing *all* amplitudes of the branch associated with $\tilde{\lambda}_{\theta}^A = x_{\theta_j}^A$ of system A back to time t_0 , there is defined a conditioned state $Q_{loop}(\mathbf{x}, \mathbf{p} | \tilde{\lambda}_{\theta}^A)$ where $\mathbf{x} = (x_{\theta A}, x_{\phi B})$ and $\mathbf{p} = (p_{\theta A}, p_{\phi B})$, associated with these amplitudes (Fig. 5). The outcome $\tilde{\lambda}_{\theta}^A$ at one site implies a *restricted* quantum state $\rho_{\tilde{\lambda}_{\theta}^A}^B$ with Q function $Q(x_B, p_B | \tilde{\lambda}_{\theta}^A)$ for system B , determined by integrating $Q_{loop}(\mathbf{x}, \mathbf{p} | \tilde{\lambda}_{\theta}^A)$ over the complementary variable $p_{\theta A}$. Hence, there is a microscopic retrocausal feedback, which determines correlations of outcomes for system B given the outcome for A . We give an evaluation of the conditioned state $Q(x_B, p_B | \tilde{\lambda}_{\theta}^A)$ for an entangled system in Appendix E. The state for B is fixed, once the amplified outcome $\tilde{\lambda}_{\theta}^A$ emerges, and hence the correlations are also fixed relative to $\tilde{\lambda}_{\theta}^A$, if there is then a change of setting to ϕ' at B . This gives a model for the nonlocal effect observed with an EPR state, when the outcome for \hat{p}_B (say) is known from the outcome for \hat{p}_A , and similarly, the outcome for \hat{x}_B is known from that for \hat{x}_A . EPR proposed that the correlation is explained by predetermined values for $\hat{x}_A, \hat{p}_A, \hat{x}_B, \hat{p}_B$ existing simultaneously at time t_0 , for any given realisation. The simulations of this paper explain the correlations differently, because the outcomes for \hat{x}_A and \hat{p}_A are not described jointly at time t_0 , only one or other being defined after amplification.

Continuing, we will see that in the model, a change of setting at B to ϕ' does not change the value for the outcome $\tilde{\lambda}_{\theta}^A$ which is already fixed and determined by the local amplification at A . There is however a microscopic

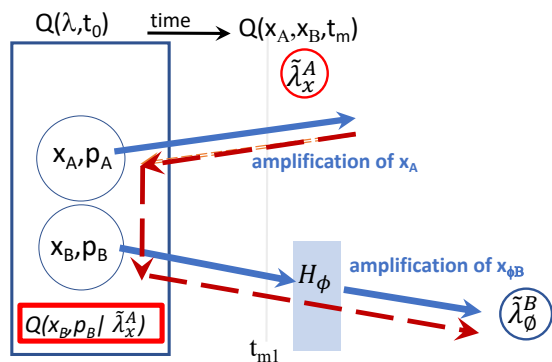


Figure 5. Measurement on entangled systems A and B , where \hat{x} is measured at A . After amplification, at time t_m , the outcome at A is determined, to be the value $\tilde{\lambda}_x^A$. The retrocausal trajectories $x_A(t)$ correlate with certain trajectories for system B at the original time t_0 , as consistent with $Q(\lambda, t_0)$. The outcome $\tilde{\lambda}_x^A$ of A implies feedback (red dashed line) which ensures the quantum state given by $Q(x_B, p_B | \tilde{\lambda}_x^A)$ for system B . This constrains the outcomes at B , if there is a change of setting by a physical device H_ϕ at B to measure $\hat{x}_{\phi B}$ at B (provided the setting at A is fixed). Details are given in Sec. IX and Appendix E, where $Q(x_B, p_B | \tilde{\lambda}_x^A)$ is evaluated for the example of a system B entangled with a meter A , illustrating a model for the collapse of the wave function.

retrocausal feedback from B to A , which means that the state at A conditioned on an amplified outcome $\tilde{\lambda}_\phi^B$ at B fixes the state at A from the loop, as $\rho_{\tilde{\lambda}_\phi^B}^A$. The *absence of signaling* is explained because this change is “hidden” (being not observable with the setting θ fixed). If there is a further change of setting from θ to θ' at the second site A , however, then this feedback becomes important. *Bell nonlocality* can emerge. As two changes of setting is required, so that no Bell nonlocality is observed when $\phi' = \phi$ or $\theta' = \theta$, there is no conflict with conclusions that classical causal-model explanations of Bell nonlocality require *fine-tuning* [53, 54, 56] (refer Appendix F).

Models for reality: weak macroscopic (local) realism: The dynamics of the amplitudes x, p in the simulations motivates a model of reality proposed previously: an *objective-field realism* or *Q-based model*, where the system is regarded at time t to be in a state with amplitudes $x(t)$ and $p(t)$. Here, similar to classical electrodynamics and Wheeler and Feynman’s absorber theory, the x, p are fields, independent of any observer [105]. Each run of the simulation represents an individual realization. The amplitudes x and p are not directly measurable.

Weaker models of reality can also be considered. In Secs. IX and X, we examine the causal structure of the simulation that would illustrate Bell nonlocality. There is consistency with a set of three premises referred to as *weak macroscopic realism* (wMR) where there is predetermination of the measurement outcome on amplification *after* any dynamics (e.g. passing through a Stern-Gerlach analyzer) which (in a Bell experiment) deter-

mines the measurement setting [49, 97, 113, 116, 117].

Connection with Bell’s theorem: Bell’s local hidden variable theories exclude Bell nonlocality. The simulations of this paper involve hidden variables, defined as the coordinates $\lambda = (x_A, p_A, x_B, p_B)$ of the bipartite Q function. In the Conclusion (Sec. X), the assumptions of Bell’s local hidden variables are analysed, and it is explained precisely how the hidden variables λ differ from those of Bell’s model.

Layout of paper: In Sec. II, we explain the measurement Hamiltonian and the Q function. The path-integral and stochastic equivalence theorems on which the paper is based are presented in Appendix A, along with the numerical verification of the computed distribution in Appendix B. In Sec. III, we give the corresponding stochastic equations. The equations modeling a measurement \hat{x} on the system in a superposition $|\psi_{sup}\rangle$ of eigenstates of \hat{x} are solved in Sec. IV. We also solve for superpositions of coherent states and for the measurement of \hat{p} on $|\psi_{sup}\rangle$. Born’s rule is deduced, and justification of MR and macroscopic causality given. The hidden loop and the mechanism for the collapse of the wave function is presented in Sec. V, with details of the causal relations in Sec. VI. In Secs. VII and VIII, we present the solutions for continuous-variable EPR correlations and Bell nonlocality. The associated causal model that does not conflict with Bell’s theorem is given in Sec. IX. Fine-tuning is explained in Appendix F. In the Conclusion (Sec. X), it is shown how the results support consistency with a subset of Bell’s local realistic premises. The distinction between the hidden variables of the simulations and those of Bell’s local hidden variables is analyzed. Experiments are proposed.

II. MEASUREMENT MODEL

In this paper, the system dynamics is described by a unified stochastic model motivated by the Q function [99]. The examples of this paper use bosonic fields. Our approach requires the measurement process to be included in the dynamics. For this purpose, we use a model of a common measuring device that produces macroscopic outputs, namely the parametric amplifier [118].

By comparison with theories using a collapse of the wavefunction, or coupling to an environment, our measurement requirement is simply that the output of the meter is macroscopic. The importance of amplification is explained by Bohr, who regarded measurement as amplification [15]. This model can be readily generalized. Fermionic Q-functions exist [119, 120], and have similar properties and equations. We expect other models of meters to have analogous behavior. A model of measurement which takes into account the coupling the microscopic system to a second macroscopic device, a meter [121], is examined in Appendix E and Ref. [122].

We compare our results with the Copenhagen measurement approach, which addresses a quantum state ex-

pressed as a linear combination $|\psi_{sup}\rangle = \sum_j c_j |x_j\rangle$ of eigenstates $|x_j\rangle$ of \hat{x} where c_j are probability amplitudes. The Copenhagen measurement postulate asserts that for such a state, the set of possible outcomes of the measurement \hat{x} is the set $\{x_j\}$ of eigenvalues of \hat{x} . The probability of a given outcome x_j is $P_j = |c_j|^2$. After measurement, the system “collapses” into eigenstates $|x_j\rangle$ associated with each outcome x_j . The measurement problem is to understand the transition from the state $|\psi\rangle$ to the final state $|x_j\rangle$.

A. Measurement model: parametric amplification

First, restricting our analysis to a single mode for clarity, we define the complementary quadrature phase amplitude \hat{x} and \hat{p} observables

$$\begin{aligned}\hat{x} &= \hat{a} + \hat{a}^\dagger \\ \hat{p} &= (\hat{a} - \hat{a}^\dagger)/i\end{aligned}\quad (2.1)$$

where \hat{a} is the boson destruction operator [123]. Hence $\hat{a} = (\hat{x} + i\hat{p})/2$. This implies the uncertainty relation

$$\langle(\Delta\hat{x})^2\rangle\langle(\Delta\hat{p})^2\rangle \geq 1 \quad (2.2)$$

where $\langle(\Delta\hat{x})^2\rangle = \langle\hat{x}^2\rangle - \bar{x}^2$ and $\langle(\Delta\hat{p})^2\rangle = \langle\hat{p}^2\rangle - \bar{p}^2$ are the variances of \hat{x} and \hat{p} .

We analyze the simplest measurement procedure that can take place – that of direct amplification to a macroscopic signal. We take a simple model of measurement using a parametric amplifier in a rotating frame, as in current low noise photonic or superconducting experimental measurements. To measure \hat{x} , the system prepared in $|\psi_{sup}\rangle$ is amplified according to the Hamiltonian [118]

$$H_{amp} = \frac{i\hbar g}{2} [\hat{a}^{\dagger 2} - \hat{a}^2] \quad (2.3)$$

where $g > 0$ is real. The system evolves under H_{amp} for a time t_f , to give the final measurement output. The measurement is completed simply by the fields being amplified to become macroscopic, and hence detectable to macroscopic devices or observers. No special “collapse” is required, only normal physical processes.

For $g > 0$, it is known that the dynamics of H_{amp} gives solutions that amplify the “position” \hat{x} but attenuate the orthogonal “momentum” quadrature \hat{p} . This is clear from the standard operator Heisenberg equations which give solutions

$$\begin{aligned}\hat{x}(t) &= \hat{x}(0) e^{gt} \\ \hat{p}(t) &= \hat{p}(0) e^{-gt}.\end{aligned}\quad (2.4)$$

H_{amp} induces squeezing in \hat{p} [118]. The interaction H_{amp} has been realized experimentally, often with the motivation to generate reduced quantum fluctuations [124, 125]. A related model of measurement based on amplification was presented by Glauber, for a two-slit experiment [100, 126].

B. Single-mode Q function

To solve for single-mode evolution, we use the Q function [99]

$$Q(\alpha) = \frac{1}{\pi} |\langle \alpha | \psi \rangle|^2, \quad (2.5)$$

defined for a quantum state $|\psi\rangle$ with respect to the nonorthogonal basis of coherent states $|\alpha\rangle$. The coherent state $|\alpha\rangle$ satisfies $\hat{a}|\alpha\rangle = \alpha|\alpha\rangle$ where α is a complex number. Here the phase-space coordinates $\boldsymbol{\lambda}$ are the real coordinates x and p , given by $\alpha = (x + ip)/2$. The single-mode Q function defines the quantum state $|\psi\rangle$ uniquely as a positive probability distribution. The moments evaluated from the Q function distribution are anti-normally ordered operator moments [127]. The anti-normally ordered variances $\sigma_x^2(t)$ and $\sigma_p^2(t)$ are precisely the variances of x and p as defined by the Q function $Q(x, p, t)$.

The Q function for the eigenstate $|x_j\rangle$ of \hat{x} is readily evaluated. Applying the definition (2.5) and using the overlap function [123]

$$\langle x_j | \alpha \rangle = \frac{1}{\pi^{1/4}} \exp\left(-\frac{(x - x_j)^2}{4} + \frac{i}{4}p(2x_j - x)\right), \quad (2.6)$$

the Q function for the eigenstate is given as the Gaussian

$$\begin{aligned} Q(x, p) &\sim |e^{-\frac{1}{4}(x-x_j)^2} e^{i\frac{p}{4}(2x_j-x)}|^2 \\ &\rightarrow e^{-\frac{1}{2}(x-x_j)^2} \end{aligned} \quad (2.7)$$

where we note that without a momentum cut-off, the distribution is not normalizable, as usual with pure position eigenstates in quantum mechanics. We resolve this below by modeling the eigenstates in \hat{x} as highly squeezed states. We see that the Gaussian has a variance $\langle x^2 \rangle - \langle x \rangle^2$ of 1, which corresponds to the level of the quantum-vacuum noise (2.2). This vacuum noise in the Q function is ‘‘hidden’’, since for the eigenstate the measurable noise level for \hat{x} is zero, $\langle (\Delta\hat{x})^2 \rangle = 0$.

C. The superposition state

We will consider a measurement on the system prepared at time t_0 in the superposition $|\psi_{sup}\rangle = \sum_i c_i |x_i\rangle$, where $|x_j\rangle$ is an eigenstate of \hat{x} of the ‘‘position’’ quadrature with eigenvalue x_j . Applying the definition (2.5), the Q function for this state is given by

$$Q(x, p) \sim \left| \sum_j c_j e^{-\frac{1}{4}(x-x_j)^2} e^{i\frac{p}{4}(2x_j-x)} \right|^2, \quad (2.8)$$

which comprises a sum of Gaussians centered at each eigenvalue x_j and additional interference cross-terms that we symbolize by \mathcal{I} [128].

For the sake of simplicity without losing the essential features, we examine the simple superposition

$$|\psi_{sup}\rangle = c_1 |x_1\rangle + c_2 |x_2\rangle. \quad (2.9)$$

where c_1 real and $c_2 = |c_2|e^{i\varphi}$. We will also take, without loss of the essential features, $x_2 = -x_1$. Here the c_j are complex amplitudes satisfying $|c_1|^2 + |c_2|^2 = 1$. The Q function simplifies to

$$\begin{aligned} Q_{sup}(x, p) &\sim |c_1|^2 e^{-(x_1-x)^2/2} + |c_2|^2 e^{-(x_1+x)^2/2} \\ &\quad - 2c_1|c_2| e^{-x_1^2/2} e^{-x^2/2} \sin(x_1 p) \end{aligned} \quad (2.10)$$

where we take $c_2 = i|c_2|$. A different choice of the phase φ introduces a phase shift in the sinusoidal term, which we comment on later. The Q function for the superposition differs from the Q function, $Q_{mix}(x, p)$, for the mixture of eigenstates,

$$\rho_{mix} = \frac{1}{2} \{ |x_1\rangle\langle x_1| + |x_2\rangle\langle x_2| \}, \quad (2.11)$$

only by the addition of the third term \mathcal{I} corresponding to fringes. Since the limiting two-dimensional Q function cannot be normalized due to the infinite variance in \hat{p} , in the last line of (2.10) we have written the normalized projection along the x axis for a given p .

To obtain a more physical solution for (2.9), we model the position eigenstates as highly squeezed states in \hat{x} . The squeezed state is defined as [118]

$$|\beta_j, z\rangle_{sq} = D(\beta_j)S(z)|0\rangle. \quad (2.12)$$

Here, $|0\rangle$ is the vacuum state satisfying $\hat{a}|0\rangle = 0$, and $D(\beta_j) = e^{\beta_j \hat{a}^\dagger - \beta_j^* \hat{a}}$ and $S(z) = e^{\frac{1}{2}(z^* \hat{a}^2 - z \hat{a}^{\dagger 2})}$ are the displacement and squeezing operators, with z and β_j being complex numbers. For the state with squeezed fluctuations in \hat{x} , we note that $z = r$ is a real, positive number, referred to as the *squeeze parameter*. Defining $\bar{x} = \langle \hat{x} \rangle$, $\bar{p} = \langle \hat{p} \rangle$, we find

$$\begin{aligned} \langle (\Delta\hat{x})^2 \rangle &= \langle \hat{x}^2(t) - \bar{x}^2 \rangle = e^{-2r} \\ \langle (\Delta\hat{p})^2 \rangle &= \langle \hat{p}^2(t) - \bar{p}^2 \rangle = e^{2r}. \end{aligned} \quad (2.13)$$

The parameter r determines the variances and hence the amount of squeezing in \hat{x} . The mean values are given by $\langle \hat{a} \rangle = (\bar{x} + i\bar{p})/2 = \beta_j$ where $\beta_j = (x_j + ip_j)/2$ and x_j and p_j are real. A position eigenstate denoted $|x_j\rangle$ is thus a squeezed state with $r \rightarrow \infty$, where x_j is real and $p_j = 0$.

The superposition (2.9) is approximated as the superposition of two squeezed states

$$|\psi_{sup}(r)\rangle = c_1 \left| \frac{x_1}{2}, r \right\rangle_{sq} + c_2 \left| -\frac{x_1}{2}, r \right\rangle_{sq} \quad (2.14)$$

where x_1 and x_2 are real, $p_j = 0$. We select c_1 real and $c_2 = i|c_2|$ for convenience so that the normalization procedure gives the above form for all values of r and x_1 . Otherwise, the normalization involves an extra term

which vanishes in the limit where the two states forming the superposition are orthogonal. Here, this requires large r , i.e. $r \rightarrow \infty$.

The Q function for the squeezed state (2.12) is

$$Q(x, p) = \frac{1}{2\pi\sigma_x\sigma_p} e^{-(x-x_0)^2/2\sigma_x^2} e^{-(p-p_0)^2/2\sigma_p^2}, \quad (2.15)$$

where $\sigma_x^2 = 1 + e^{-2r}$, and $\sigma_p^2 = 1 + e^{2r}$. Here, σ_x^2 and σ_p^2 are the variances of x and p in the Q function distribution, in agreement with the different variances (2.13) for the squeezed state (2.12), once anti-normal ordering is accounted for.

The Q function for the superposition (2.14) of two squeezed states is

$$Q_{sup}(x, p) = \frac{e^{-p^2/2\sigma_p^2}}{2\pi\sigma_x\sigma_p} \left\{ |c_1|^2 e^{-(x-x_1)^2/2\sigma_x^2} + |c_2|^2 e^{-(x+x_1)^2/2\sigma_x^2} - 2|c_1c_2| e^{-(x^2+x_1^2)/2\sigma_x^2} \sin(px_1/\sigma_x^2) \right\}, \quad (2.16)$$

where $\sigma_x^2 = 1 + e^{-2r}$ and $\sigma_p^2 = 1 + e^{2r}$. We have restricted to $c_2 = i|c_1|$. In the limit $r \rightarrow \infty$ where the system becomes the superposition $|\psi_{sup}\rangle$ of two eigenstates, the Q function has two Gaussian peaks with fixed variance $\sigma_x^2 = 1$, centered at the eigenvalues x_1 and x_2 , along with a central peak centered at $\bar{x} = 0$ whose amplitude has a fringe pattern damped by a term $e^{-x_1^2/2}$.

D. Evolution: measurement dynamics

In the following sections, we will solve for *trajectories* $x(t)$ and $p(t)$ of the amplitudes defined in the Q function $Q(x, p)$, as the measurement of \hat{x} on the superposition state evolves (Fig. 1). This involves a detailed derivation of the stochastic equations. However, much can be inferred from the evolution of the Q function alone. We give a brief summary.

The Q function (2.16) evolves according to H_{amp} to give a final Q distribution which is calculable: We will see that the marginal probability for observing x at the final time t_f , after the interaction H_{amp} has been completed, is

$$Q_{sup}(x, t_f) \rightarrow |c_1|^2 e^{-(x-Gx_1)^2/2\sigma_x^2} + |c_2|^2 e^{-(x-Gx_2)^2/2\sigma_x^2} \quad (2.17)$$

where $G = e^{|g|t_f}$. Since only the means are amplified, *not* the variances, this gives two *sharp* peaks located at Gx_1 and Gx_2 respectively, with relative probabilities $|c_1|^2$ and $|c_2|^2$. The values x_i which correspond to the means of the Gaussians in (2.8) and (2.10) are *amplified* according to

$$x_j \rightarrow X_j = e^{|g|t_f} x_j \quad (2.18)$$

In the model for measurement proposed here, given by amplification, the final values $x(t_f)$ are *assumed to be ultimately observed* (refer to the left plot of Fig. 1). The amplification factor G is accounted for in the final detection, and the inferred result of the measurement is deduced to be $x(t_f)/G$. This corresponds to the means x_j of the Gaussians, the eigenvalues x_j , which are the results of the measurement, consistent with the measurement postulates.

In the amplification process H_{amp} , the interference terms \mathcal{I} appearing in (2.8) and (2.10) are attenuated because of the proportionality to terms $e^{-x_j^2}$, which decay on amplification of x_j where $x_j \rightarrow e^{gt}x_j$. The measurement of \hat{x} amplifies the x_j variables, but attenuates the p variables to the minimum possible level of the vacuum (Fig. 1, right). The complementary observable p therefore does not appear in the final measured probability. (In fact, where $\varphi = \pi/2$, the sine term in (2.16) ensures that the interference term \mathcal{I} will completely vanish in the marginal for x .) The probability for the outcomes x_j , given $t_f \rightarrow \infty$, is therefore

$$P(x_j) \equiv Q_{sup}(x_j, t_f) = |\langle x_j | \psi \rangle|^2, \quad (2.19)$$

in agreement with the quantum prediction (Born's rule).

While the eigenvalues x_j are amplified, the "hidden" noise about these values (as evident in the Q function for the eigenstate of \hat{x} , Eq. (2.7)) is not amplified. Hence, a "hidden" vacuum fluctuation $x_\delta = \delta x = x - x_j$ is not measurable, and does not lead to a macroscopic value. The values for the trajectories of the *full* amplitudes $x(t)$ are determined by a *future* boundary condition [104, 106], as shown in Fig. 2, which depicts the causal structure of the simulation.

E. Equation of motion for Q: Generalised Fokker-Planck equation (GFPE)

We can calculate directly how the Q function evolves in time for a Hamiltonian H . In general terms, the Q function probability density $Q(\boldsymbol{\lambda}, t)$ for a phase-space coordinate $\boldsymbol{\lambda}$ is defined with respect to a non-orthogonal operator basis $\hat{\Lambda}(\boldsymbol{\lambda})$ as

$$Q(\boldsymbol{\lambda}, t) \equiv Tr \left(\hat{\Lambda}(\boldsymbol{\lambda}) \hat{\rho}(t) \right), \quad (2.20)$$

where ρ is the density operator of the system. As $Q(\boldsymbol{\lambda}, t)$ is normalized to unity, it is necessary to normalize the basis so it integrates to unity, and the normalization condition is that $\int \hat{\Lambda}(\boldsymbol{\lambda}) d\boldsymbol{\lambda} = \hat{1}$. The basis satisfies $\hat{\Lambda}^2(\boldsymbol{\lambda}) = \mathcal{N}(\boldsymbol{\lambda}) \hat{\Lambda}(\boldsymbol{\lambda})$, which is different to the condition for projectors that $\hat{P}^2 = \hat{P}$, because it is a continuous nonorthogonal basis.

From the Schrodinger equation, the dynamics of the probability distribution is obtained from the usual equation $i\hbar d\hat{\rho}/dt = [\hat{H}, \hat{\rho}]$. As a result, one obtains an equa-

tion for the Q function time-evolution:

$$\frac{dQ(\boldsymbol{\lambda}, t)}{dt} = \frac{i}{\hbar} \text{Tr} \left\{ \left[\hat{H}, \hat{\Lambda}(\boldsymbol{\lambda}) \right] \hat{\rho}(t) \right\}. \quad (2.21)$$

This is equivalent to a zero-trace diffusion equation for the variables $\boldsymbol{\lambda}$, of form $\dot{Q}(\boldsymbol{\lambda}, t) = \mathcal{L}(\boldsymbol{\lambda}) Q(\boldsymbol{\lambda}, t)$, where $\mathcal{L}(\boldsymbol{\lambda})$ is the differential operator for Q function dynamics. The examples given in this paper are bosonic, the Q function (2.5) in terms of the density operator being $Q(x, p) = \frac{1}{\pi} \langle \alpha | \rho(t) | \alpha \rangle$ for the single-mode field [99]. Such distributions can be extended to include fermions as well [119, 120, 129]. For the single-mode, the phase-space coordinates $\boldsymbol{\lambda}$ are the real coordinates x and p , given by $\alpha = (x + ip)/2$.

For the system evolving according to the Hamiltonian $H_{amp} = \frac{i\hbar g}{2} [\hat{a}^{\dagger 2} - \hat{a}^2]$ given by (2.3), a dynamical equation for the Q function can be derived [104]. Applying the correspondence rules to transform operators into differential operators, one obtains a generalized Fokker-Planck type equation in terms of complex coherent state variables α :

$$\frac{dQ}{dt} = - \left[g \frac{\partial}{\partial \alpha} \alpha^* + \frac{g}{2} \frac{\partial^2}{\partial \alpha^2} + h.c. \right] Q. \quad (2.22)$$

Using the quadrature definitions where the vacuum has unit noise in x and p , one has $\alpha = (x + ip)/2$, or $\hat{x} = \hat{a} + \hat{a}^\dagger$. We obtain

$$\frac{dQ}{dt} = [\partial_p(gp) - \partial_x(gx) + g(\partial_p^2 - \partial_x^2)] Q. \quad (2.23)$$

This demonstrates a diffusion matrix which is traceless and equally divided into positive and negative definite parts, and a drift matrix:

$$\mathbf{A} = \begin{bmatrix} \dot{x} \\ \dot{p} \end{bmatrix} = \begin{bmatrix} gx \\ -gp \end{bmatrix}. \quad (2.24)$$

III. FORWARD-BACKWARD STOCHASTIC EQUATIONS

The next step is to derive from the equation of motion (2.23) for $Q(x, p)$ the forward-backward stochastic equations that determine the dynamics of the Q function amplitudes $\boldsymbol{\lambda} = (x, p)$, for the interaction H_{amp} . This requires the proof of the connection between the stochastic equations for $x(t)$ and $p(t)$ and the Generalised Fokker-Planck equation (2.21) governing the evolution of the Q function. There is an equivalent time-symmetric stochastic action principle for $Q(\boldsymbol{\lambda}, t)$, leading to probabilistic path integrals [106]. These have sample trajectories $\boldsymbol{\lambda}$ that define the realistic path for all times.

In this paper, we derive two Theorems generalizing these results to the case of an initial superposition state, where a feedback leading to hidden loops is possible. The Theorems have a general applicability, applying to

a wider range of systems than those treated in this paper, and are hence presented as a distinct result in Appendix A. The Theorems are formulated and derived in Appendix A. We prove the equivalence between the averages calculated from the trajectories $\boldsymbol{\lambda}(t)$ (x and p) and those calculated from the Q function, $Q(x, p, t)$. This result is *independently* confirmed by statistical comparisons of the numerical simulations with the Q function, as presented in Appendix B.

The stochastic equations motivates a closely-connected ‘‘hidden-variable’’ model for quantum measurement. We can regard the Q function amplitudes $\boldsymbol{\lambda}$ (x and p in this paper) as representing a realization of the quantum state at the time t_1 , immediately prior to the measurement, as well as during and after the measurement. The physical assumptions made here for the meter that defines the measurement process are:

- Measurement is identified as an amplification process (after measurement settings are fixed).
- The field amplitudes x and p are ontological variables, with distribution $Q(x, p, t)$ at time t .
- The probability of an observation is $Q(x, t_f) = \int Q(x, p, t_f) dp$ where t_f is the time of interaction with the amplifier. Here, we denote x as the amplified variable.
- Amplified variables satisfy future boundary conditions.
- Attenuated variables satisfy past boundary conditions.
- The amplifier does not couple amplified and attenuated quadratures.

The last condition can be relaxed for meters where one quadrature is macroscopic so that cross-coupling noise is negligible, as explained in examples in the accompanying paper.

We explain that the third assumption leads to Born’s rule, as verified in Section IV.D, and is hence supported by it. The fourth and fifth assumptions can also be deduced within the framework of the stochastic method, and are justified by the numerical validation in the Appendix B that the distribution for the stochastic variables $x(t)$ and $p(t)$ is given by $Q(x, p, t)$ where $Q(x, p, t)$ is the Q function of the quantum solution for the evolution. The third, fourth and fifth assumptions are hence self-consistent.

Using the equivalence theorems in Appendix A, we solve the measurement dynamics for the dynamics of H_{amp} . Here, the x and p dynamics decouple. However, to obtain a mathematically tractable equation for the traceless noise matrix, we follow [104] and the sign of t is reversed in the amplified dynamics of x .

The corresponding integrated stochastic equations for $g > 0$ are:

$$\begin{aligned} p(t) &= p(t_0 | x_0) - \int_{t_0}^t g p dt' + \int_{t_0}^t dw_p \\ x(t) &= x(t_f) - \int_t^{t_f} g x dt' + \int_t^{t_f} dw_x \end{aligned} \quad (3.1)$$

where $\langle dw_\mu dw_\nu \rangle = 2g\delta_{\mu\nu}dt$, and both $x(t_f)$ and $p(t_0 | x_0)$ represent random boundary conditions with a specified marginal and conditional probability respectively.

Alternatively, in differential form, we obtain for p the equation [104, 105]

$$\frac{dp}{dt} = -gp + \sqrt{2g}\xi_p \quad (3.2)$$

which has a boundary condition in the past i.e. determined by the Q function at the initial time $t_1 = 0$. The equation for x is

$$\frac{dx}{dt_-} = -gx + \sqrt{2g}\xi_x \quad (3.3)$$

where $t_- = -t$. These equations form the basis for the phase-space simulations presented in this paper. The equation is solved backwards in time, and therefore has a boundary condition in the future, defined as the time t_f when the amplification is completed. Defining $\xi = (\xi_p, \xi_x)$, the Gaussian random noises $\xi_\mu(t)$ satisfy: $\langle \xi_\mu(t) \xi_\nu(t') \rangle = \delta_{\mu\nu} \delta(t - t')$. Thus, there is a forward-backward stochastic differential equation (FBSDE), for individual trajectories. This describes two individual stochastic trajectories, such that the average of the dynamical trajectories equals the Q function averages. The trajectories are decoupled dynamically, with decay and stochastic noise occurring in each of the time directions. One propagates forward, and one backwards in time.

In examples treated here, the trajectory in x has a future marginal, $P(x, t_f)$, while the trajectory in p has a past conditional distribution, $P(p | x, t_0)$, which depends on x in the future (Figs. 6 and 7), giving a cyclic causal behavior. It is possible to exchange these, by time-reversal symmetry. There is an apparent Grandfather-type paradox arising from the present seeming to depend on the future. This will be examined later in Sec. V by proposing a causal model based on the simulations.

However, the result of causal consistency is proved by the Theorems in Appendix A (refer Fig. 3 for a depiction and proposed experiment): The quantum state $|\psi\rangle$ as determined uniquely by the Q function $Q(x, p, t)$ depends *only* on the time t of evolution, starting from an initial time $t_1 = 0$. This is despite the trajectory $x(t)$ depending on the future boundary, which can be an arbitrary infinite time t_f in the future. The adjustment of the future time t_f cannot change the quantum state Q at time t . Similar consistencies are well known in absorber theory for electromagnetic fields [8, 13, 14] and in

theories of closed time-like curves [114]. The consistency ensures that the trajectories at large time $t_f \rightarrow \infty$ satisfy the conditional relations connecting $x(t_f)$ and $p(t_f)$ for the amplified state, which quantifies the end part of the loop. In this case, of the measurement interaction H_{amp} , at the future time $t_f \rightarrow \infty$, the p decouples completely from x , and there is no further feedback in the simulation from p to x : the loop is hence incomplete in this sense.

IV. SOLVING THE STOCHASTIC EQUATIONS: MACROSCOPIC REALISM AND BORN'S RULE

A. Measuring \hat{x} : A system in a superposition of eigenstates of \hat{x}

We solve the trajectories for the field amplitudes, by stochastically sampling according to the noise terms, $\xi_\mu(t)$. From Eq. (3.3), the x solution at t depends on the boundary condition for x imposed in the *future* final time t_f , after the measurement has been completed. We solve this equation by propagating the trajectories for x backwards in time (Figs. 6 and 7).

To evaluate the sampling distribution for the future boundary at time t_f , we calculate the evolving Q function $Q_{sup}(x, p, t)$ at the time $t = t_f$, from the Hamiltonian H_{amp} of (2.3) that amplifies \hat{x} . The original Q function in the initial time t_1 is given by (2.16). We calculate the Q function for the amplified system with respect to x , after the measurement H_{amp} has acted for a time t . This calculation can be done in two ways. The state formed after the unitary evolution H_{amp} is $e^{-iH_{amp}t/\hbar}|\psi_{sup}(r)\rangle$, for which the Q function can be evaluated directly as

$$\begin{aligned} Q_{sup}(x, p, t) &= \frac{e^{-p^2/2\sigma_p^2(t)}}{2\pi\sigma_x(t)\sigma_p(t)} \left\{ |c_1|^2 e_1^{-(x-G(t)x_1)^2/2\sigma_x^2(t)} \right. \\ &\quad + |c_2|^2 e^{-(x+G(t)x_1)^2/2\sigma_x^2(t)} \\ &\quad \left. - 2|c_1||c_2| e^{-(x^2+G^2(t)x_1^2)/2\sigma_x^2(t)} \right. \\ &\quad \left. \times \sin\left(\frac{pG(t)x_1}{\sigma_x^2(t)}\right) \right\}. \end{aligned} \quad (4.1)$$

Here $G(t) = e^{gt}$ is the amplification factor, and the variances becomes

$$\sigma_{x/p}^2(t) = 2(1 \pm \tanh(r - gt))^{-1} = 1 + e^{\pm 2(gt-r)}. \quad (4.2)$$

The solutions can also be found from the dynamical equation (2.21) for the Q function. We denote the Q function at the future time $t = t_f$ as $Q_{sup}(x, p, t_f)$.

Due to the separation of variables x and p in Eqs. (3.2)-(3.3), the *marginal* distribution $Q_{sup}(x, t_f) = \int Q_{sup}(x, p, t_f) dp$ for x at the future time $t = t_f$ determines the initial sampling distribution for the x trajectories. The marginal for x at the time $t \geq 0$ is

$$\begin{aligned} Q_{sup}(x, t) &= \frac{1}{\sqrt{2\pi}\sigma_x(t)} \left\{ |c_1|^2 e^{-(x-G(t)x_1)^2/2\sigma_x^2(t)} \right. \\ &\quad \left. + |c_2|^2 e^{-(x+G(t)x_1)^2/2\sigma_x^2(t)} \right\} \end{aligned} \quad (4.3)$$

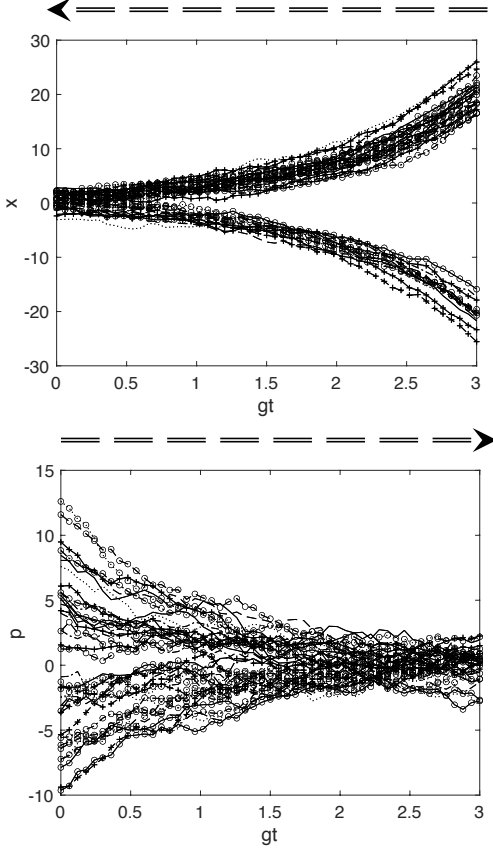


Figure 6. Measurement of \hat{x} on a system prepared in a superposition given by $|\psi_{sup}\rangle = \frac{1}{\sqrt{2}}(|x_1\rangle + i|x_2\rangle)$. Here, $x_1 = -x_2 = 1$, so that $|\psi_{sup}\rangle$ models a microscopic superposition. The top plot shows trajectories for x as the system evolves for a time t according to H_{amp} which amplifies \hat{x} . The trajectories originating from the boundary at $t_f = 3/g$ are sampled from a distribution that is a 50/50 mixture of two Gaussians, with means $e^{gt}x_1$ and $-e^{gt}x_1$, and variance $\sigma_x^2 = 1$. The trajectories propagate backwards from the future boundary at $gt = 3$, from either e^{gt} or $-e^{gt}$ ($g > 0$), but subject to a noise input δx with variance at the vacuum level, $\sigma_x^2 = 1$. The noise $\delta x(t) = x(t) - x_j$ ($j = 1, 2$) is not amplified nor attenuated. The lower plot shows the forward-propagating trajectories for the complementary variable p . Here, the values are attenuated to the vacuum noise level, $\sigma_p^2 = 1$. The superposition is approximated by (2.14) with $r = 2$.

which comprises two Gaussian peaks (one for each outcome x_j) with equal variance $\sigma_x^2(t) = 1 + G^2(t) [\sigma_x^2(0) - 1]$ where $G(t) = e^{gt}$. The initial condition for a given run of the equation (3.3) for $x(t)$ is

$$Gx_j + \delta x \quad (4.4)$$

where j is selected to be 1 or 2 with probability $|c_j|^2$, and where δx is a random Gaussian noise term with zero mean and variance $\sigma^2 = 1$, independent of the value j . The sampling is determined by the future marginal, which is identical to that for the system prepared in a

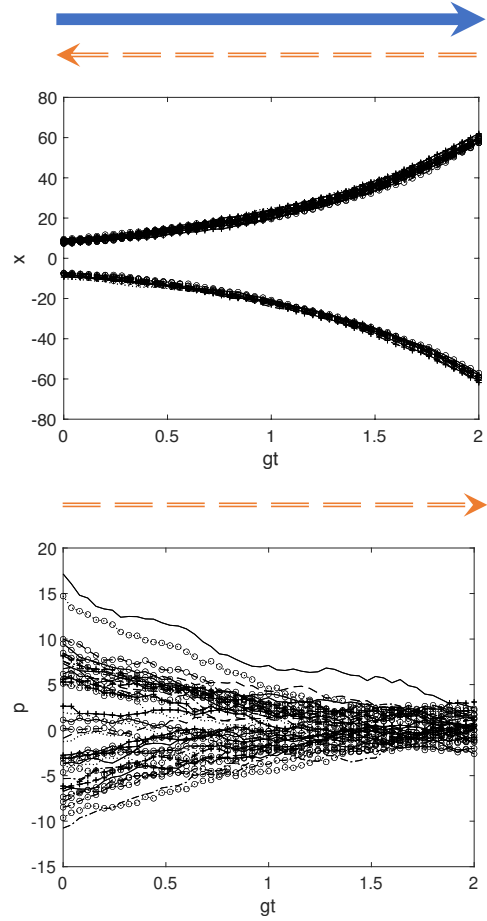


Figure 7. Simulations as for Fig. 6 and 2, describing measurement of \hat{x} for a macroscopic superposition, where $x_1 = -x_2 = 8$. The top figure shows the stochastic trajectories propagating backwards from the future boundary at $gt = 2$, from either Gx_1 or $-Gx_1$ ($G = e^{gt}$), but subject to a future noise input δx with variance at the vacuum level, $\sigma_x^2 = 1$. The noise $\delta x(t) = x(t) - x_j$ ($j = 1, 2$) for each branch is not amplified nor attenuated. The inferred outcome for \hat{x} after amplification is $x(t)/G$, giving either x_1 or $-x_1$ with an error that becomes smaller with G . For the macroscopic superposition, the amplitudes $x(0)$ at $t = 0$ are connected to the final inferred outcome to be either x_1 or $-x_1$. This gives a macroscopic causal relation (solid blue line). The actual individual trajectories stemming from each final value are retrocausal however, being subject to the noises δx and $\xi_x(t)$. The orange dashed lines represent retrocausal (right to left) and causal (left to right) influences for x and p . The p and δx are not amplified and hence not measured. The conditional distribution $P_Q(p|x)$ at the boundary t_1 determines the correlation between x and p at t_1 , which ensures connection between forward and backward trajectories.

mixture of eigenstates, ρ_{mix} , (Eq. (2.11)). This is a precise result for the examples we consider here where for the superposition (2.9), $\varphi = \pi/2$, and true in a limiting sense more generally, because the interference terms \mathcal{I} associated with the superposition *do not amplify*, under H_{amp} .

The *procedure* of the simulation hence implies a *forward causal relation*, as well as the *microscopic retro-causal* trajectory with input, δx . The causal relations involved in the simulation are depicted in Fig. 2 and examined in detail in Sec. VI. The initial Q function at time t_0 involves a set of Gaussians with means corresponding to the eigenvalues x_j : The final Q function at time t_f directly follows from the initial Q function, with the means being amplified to Gx_j . This is depicted by the deterministic forward causal relation $x_j \rightarrow Gx_j$ given by the solid blue line in Figs. 7 and 2. The relation being deterministic can also be considered in the reverse time direction, $Gx_j \rightarrow x_j$ (double arrows in Fig. 2).

The backward trajectories for $r = 2$ are shown in Figs. 1, 6 and 7 and are depicted by the dashed arrows indicating the negative time direction. The important result is that regardless of the separation $\sim |x_1|$ between the eigenvalues associated with the eigenstates $|x_1\rangle$ and $| -x_1\rangle$, the eigenstates are always distinguishable upon measurement for large $G = gt$. This occurs in the limit of large squeezing, $r \rightarrow \infty$, where the squeezed states become eigenstates. The result arises because the hidden vacuum noise (given in Eq. (2.16) by $\sigma_x = 1$) associated the Q function eigenstate (2.15) is *not* amplified by H_{amp} . This feature ensures the realization of the measurement postulate and Born's rule, as we explain in Section IV.D.

The important feature is that the noise level defined by

$$\delta x(t) = x(t) - x_j,$$

(where $j = 1$ and $j = 2$ corresponds to the top and lower branches respectively) is at a *constant level* throughout the simulation. This is despite that the amplitudes are amplified, and is a consequence of the retrocausality, that the noise δx enters at the *final* time t_f . The noise ξ_x due to the parametric amplification has a size of order g , but because of the retrocausal nature of the equation (3.3) this is balanced by a decay e^{-gt} .

The forwards trajectories for the attenuated variable p are shown in Figs. 1, 6 and 7. These are depicted by the forward-going orange dashed arrows. The trajectories are calculated by solving (3.2) using the boundary condition at time $t_1 = 0$, which we refer to as the past, or present, time. The forwards and backwards equations decouple, and hence it is the marginal $Q_{sup}(p, 0) = \int Q_{sup}(x, p) dx$ for p at time $t_1 = 0$ that is relevant to the sampling. We find

$$Q_{sup}(p, 0) = \frac{e^{-p^2/2\sigma_p^2}}{\sqrt{2\pi}\sigma_p} \left\{ 1 - e^{-x_1^2/2\sigma_x^2} \sin(px_1/\sigma_x^2) \right\}. \quad (4.5)$$

From this solution, we see that with increasing separation of the two eigenstates $|x_1\rangle$ and $| -x_1\rangle$ (so that $|x_1|$ increases), the fringes become less prominent (compare with Fig. 8). The evolution of $Q_{sup}(p, t)$ is shown in Fig. 9. The trajectories decay to the vacuum-noise level $\sigma_p^2 = 1$ (Fig. 10).

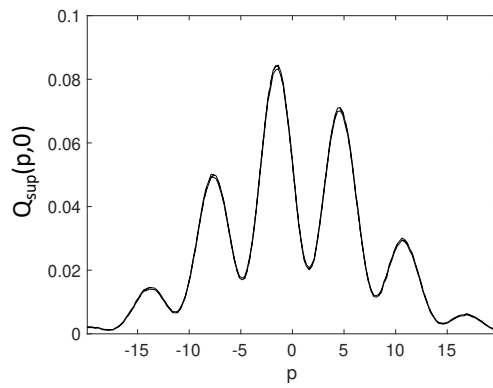


Figure 8. Measurement of \hat{x} . As for Fig. 6, with $r = 2$ and $x_1 = 1$, showing the marginal distribution $Q_{sup}(p, 0)$ for p at the *initial* time $t = t_1 = 0$, where fringes are evident.

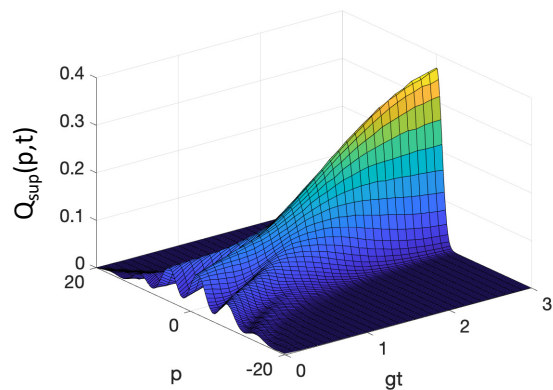


Figure 9. The distribution $Q_{sup}(p, t)$ for the forward-propagating trajectories of p , for measurement of \hat{x} . As for Fig. 6, with $r = 2$ and $x_1 = 1$. The plot shows the evolution of $Q_{sup}(p, t)$ as evaluated from 10^6 multiple trajectories, a sample of which is given in Fig. 8. The fringes are evident at $t = t_1 = 0$.

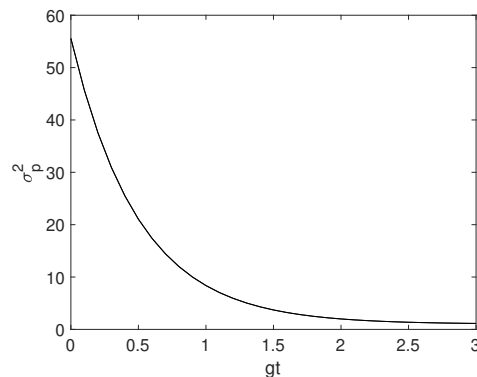


Figure 10. Measurement of \hat{x} . Plot showing the variance associated with the trajectories for p given in Fig. 6, with $r = 2$ and $x_1 = 1$. The plot shows the reduction in the variance σ_p^2 to the value of 1.

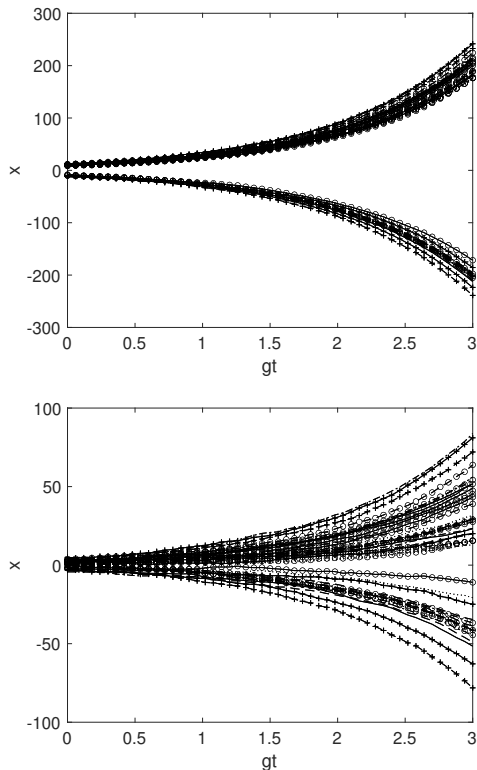


Figure 11. Measurement of \hat{x} on a cat state. Plot of backward-propagating trajectories for the amplified variable x versus time t in units of g , for the system prepared in $|cat\rangle$ (Eq. (4.6)), where $r = 0$. The plots show that the noise $\langle(\Delta\hat{x})^2\rangle = 1$ associated with a coherent state is amplified. The top plot shows $x_1 = 10$ ($\alpha_0 = 5$) where the coherent states are well separated. The second plot shows $x_1 = 2$ ($\alpha_0 = 1$), where the “hidden” noise $\sigma_x^2 = 1$ in the Q function ensures that the two peaks associated with the coherent states $|\pm\alpha_0\rangle$ overlap at $t_1 = 0$. There is no overlap however in the amplified distribution at time t_f . Here $t_f = 3/g$.

B. Measuring \hat{x} : A system in a cat state

We consider the measurement of \hat{x} on the system prepared in a superposition of two coherent states [123]

$$|cat\rangle = \frac{e^{-i\pi/4}}{\sqrt{2}}\{|\alpha_0\rangle + e^{i\pi/2}|\alpha_0\rangle\}, \quad (4.6)$$

which for large α_0 is the “cat state” [130]. This corresponds to $r = 0$ in the expression (2.14) for the Q function, with $x_1 = 2\alpha_0$. We take α_0 real.

The quantum noise associated with the Q function for the coherent state $|\alpha_0\rangle$ has *two* contributions: The first noise contribution is the “hidden” vacuum noise which exists for the eigenstate $|x_1\rangle$ itself, and is *not* amplified. The second noise contribution corresponds to the *measured* vacuum noise level $\langle(\Delta\hat{x})^2\rangle = 1$ of a coherent state. This noise level, being measurable, is *amplified* by the measurement interaction H_{amp} . The additional vacuum

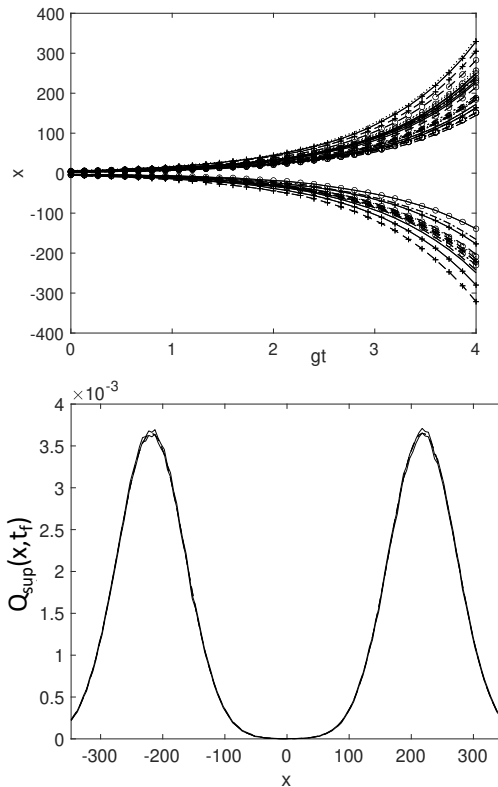


Figure 12. Measurement of \hat{x} on a cat state. Plot of backward-propagating trajectories for the amplified variable x versus gt , for the system prepared in a cat state $|cat\rangle$ (Eq. (4.6)) with $x_1 = 4$ corresponding to $\alpha_0 = 2$. Also plotted is the distribution for $Q_{sup}(x, t_f)$. This plot agrees with the distribution $P_B(x) = |\langle x|cat\rangle|^2$ predicted by quantum mechanics for the cat state. Here, $t_f = 4/g$.

noise appears in the simulations as extra noise in the final amplified outputs at time t_f , evident from Fig. 11.

We demonstrate the effectiveness of the model H_{amp} for the measurement of \hat{x} by evaluating the final marginal distribution $Q_{sup}(x, t_f)$ (in the large amplification limit), as given by (4.3). This corresponds to $P_B(x) = |\langle x|cat\rangle|^2$ as predicted by quantum mechanics (Born’s rule). Here, $|x\rangle$ is the eigenstate for \hat{x} . This is demonstrated analytically, on noting that the marginal for x where $gt \rightarrow \infty$ can be written in terms of the scaled variable $\tilde{x} = x/e^{gt}$ as

$$Q_{sup}(\tilde{x}, t) = \frac{1}{2\sqrt{2\pi}} \left\{ e^{-(\tilde{x}-x_1)^2/2} + e^{-(\tilde{x}+x_1)^2/2} \right\}, \quad (4.7)$$

where we use the result that $\sigma_x^2(t) \rightarrow e^{2gt}$. This agrees with $P_B(x) = |\langle x|cat\rangle|^2$ as predicted by quantum mechanics, and evaluated in [123] using $x_1 = 2\alpha_0$ (after correcting to deduce the inferred result \tilde{x} for the outcome x , given the amplification e^{gt}). The equivalence with $P_B(x)$ is shown in Fig. 12, for $\alpha_0 = 2$.

From Fig. 13, the trajectories for p when \hat{x} is measured

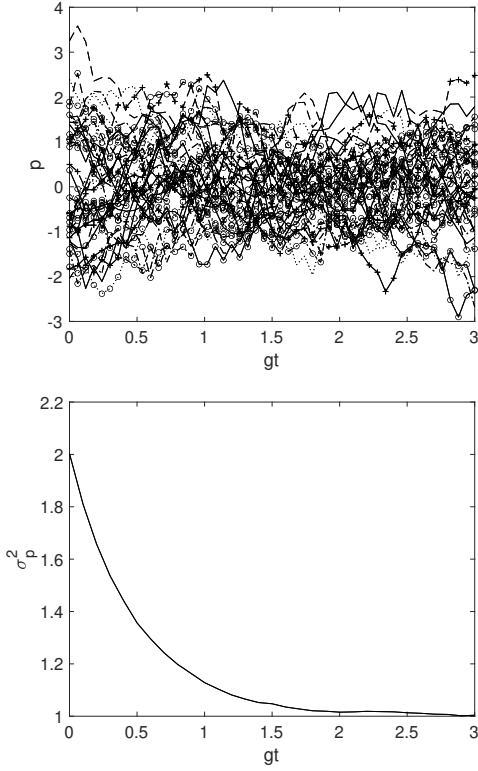


Figure 13. Measurement of \hat{x} on a cat state. Plot of forward propagating trajectories for the attenuated variable p versus time gt , for the system prepared in a cat state $|cat\rangle$ (Eq. (4.6)). The top plot shows $x_1 = 10$ where the coherent states are well separated. Here, $t_f = 3/g$. The lower plot shows the variance σ_p^2 evaluated at each time gt , evaluated over a large sample of trajectories. The final variance $\sigma_p^2(t)$ decays to 1.

are attenuated. The effect is less pronounced compared to that of the superposition of position eigenstates (Fig. 8), because there is a reduced noise in p at the initial time in this case. The measurement H_{amp} of \hat{x} amplifies \hat{x} and squeezes \hat{p} . The noise levels for the initial cat state are approximately at the vacuum level $\langle(\Delta\hat{p})^2\rangle \sim 1$, and H_{amp} has the effect of squeezing the fluctuations in \hat{p} , as shown by the variance in p in Fig. 13.

C. Measurement of \hat{p}

We have analyzed measurement of \hat{x} on the superposition of two eigenstates of \hat{x} . We now consider the complementary measurement, \hat{p} . This is incompatible with an \hat{x} measurement because it requires a different meter setting, which implies a different measurement Hamiltonian. The resulting outputs have the complementary feature of interference fringes.

The \hat{p} measurement requires amplification of p . We use

$$H_{amp} = \frac{i\hbar g}{2} [\hat{a}^{\dagger 2} - \hat{a}^2], \quad (4.8)$$

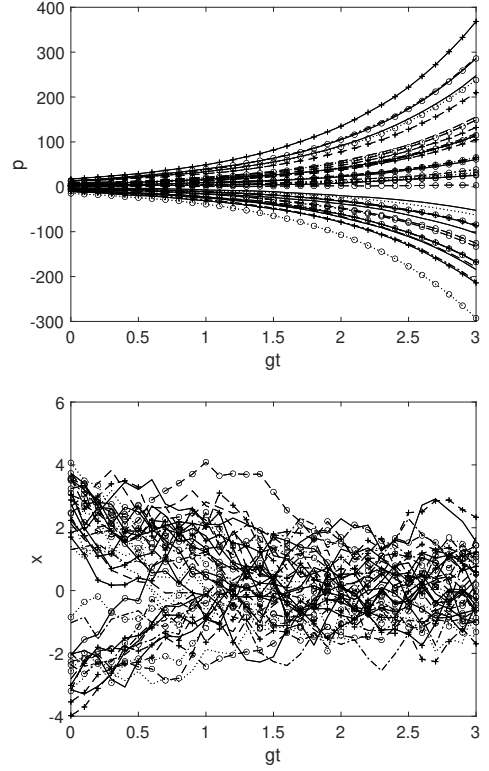


Figure 14. Measurement of \hat{p} for a system prepared in a superposition $|\psi_{sup}\rangle$ of two eigenstates $|x_1\rangle$ and $|x_2\rangle$ of \hat{x} with $x_1 = -x_2 = 3$, modeled as (2.14) with $r = 2$. The top plot shows trajectories for p propagating according to H_{amp} with $g < 0$. The final values of p at t_f are amplified. The trajectories for p propagate backwards, from the future boundary at t_f . The lower plot shows forward-propagating trajectories for the complementary variable x , which are attenuated to the vacuum noise level $\sigma_x^2 = 1$.

where g is real and $g < 0$. The dynamics from the standard operator Heisenberg equations gives the solutions

$$\begin{aligned} \hat{x}(t) &= \hat{x}(0) e^{-|g|t} \\ \hat{p}(t) &= \hat{p}(0) e^{|g|t}, \end{aligned} \quad (4.9)$$

and we see that \hat{p} is amplified. The solutions for the dynamics of the x and p variables of the Q function are as above, except that x and p exchange roles. The trajectories for p are amplified and propagate back in time. Those for x are attenuated and propagate forward in time (Fig. 14).

If we measure \hat{p} by amplifying the \hat{p} quadrature so that $g < 0$, then the full state at the later time is evaluated directly as before. The solution is given by (4.1) except that now $g < 0$. Therefore $G(t) = e^{-|g|t} \rightarrow 0$ and $\sigma_x^2(t) = 1 + e^{-2(|g|t+r)} \rightarrow 1$, in the limit of $|g|t \rightarrow \infty$. Hence, the

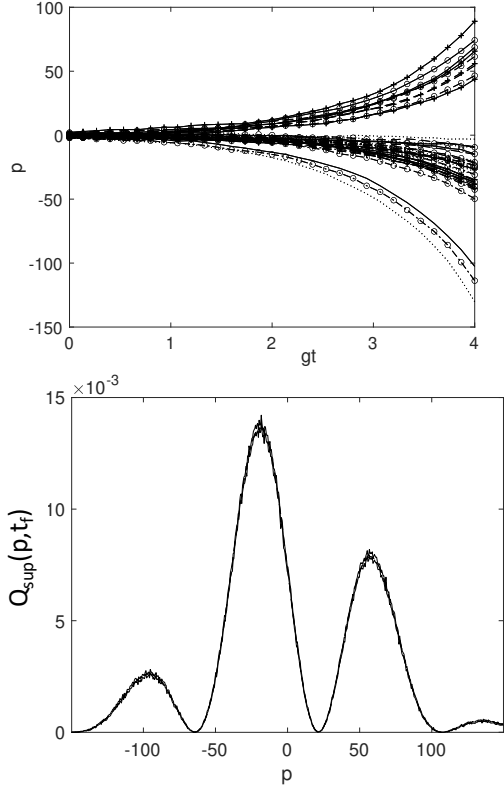


Figure 15. Plotted are the backward trajectories for p for the measurement of \hat{p} , using the Hamiltonian H_{amp} where $g < 0$. We consider the cat state $|cat\rangle$ given by Eq. (4.6) where $r = 0$, with well separated coherent states given by $x_1 = 4$. This corresponds to $\alpha_0 = 2$. Here, $t_f = 4/g$. The final distribution $Q_{sup}(p, t_f)$ is given in the lower plot. The fringes are sharply defined in agreement with $P_B(p)$ as predicted by quantum mechanics. Graphs show the upper and lower ($\pm\sigma$) sampling error values, and the exact result.

future marginal in p at time t_f is

$$\begin{aligned} Q_{sup}(p, t) &= \frac{e^{-p^2/2\sigma_p^2(t)}}{\sqrt{2\pi}\sigma_p} \left\{ 1 - e^{-\frac{G^2(t)x_1^2}{2\sigma_x^2(t)}} \sin\left(\frac{pG(t)x_1}{\sigma_x^2(t)}\right) \right\} \\ &\rightarrow \frac{e^{-p^2/2\sigma_p^2(t)}}{\sqrt{2\pi}\sigma_p} \left\{ 1 - \sin(pG(t)x_1) \right\}. \end{aligned} \quad (4.10)$$

We may write the solution as

$$Q_{sup}(\tilde{p}, t) \rightarrow \frac{e^{-\tilde{p}^2/(2e^{2r})}}{\sqrt{2\pi}} \left\{ 1 - \sin(\tilde{p}x_1) \right\}, \quad (4.11)$$

using the scaled variable $\tilde{p} = p/e^{|g|t} = p/\sigma_p(t)$ and noting that $\sigma_p(t) = e^{|g|t}e^{2r}$ for large $|gt|$, with $g < 0$.

We compare with the quantum prediction for the distribution $P_B(p)$ for the outcome p upon measurement of \hat{P} , given as $P_B(p) = |\langle p|\psi_{sup}\rangle|^2$, where $|p\rangle$ is the eigenstate of \hat{p} . We first compare for the cat state (4.6) with

a real amplitude α_0 , where $r = 0$. In fact, the solution

$$P_B(\tilde{p}) = \frac{e^{-\tilde{p}^2/2}}{\sqrt{2\pi}} \{1 - \sin(2\alpha_0\tilde{p})\} \quad (4.12)$$

given in [123] is in agreement with (4.11) (after accounting for the amplification $e^{|g|t}$), upon noting that $x_1 = 2\alpha_0$. Fig. 15 shows the future marginal and the trajectories for p , for large $|gt|$. As expected, the fringes are prominent. The comparison is done for the superposition $|\psi_{sup}\rangle$ of two eigenstates, giving exact agreement with the standard quantum prediction.

D. Born's rule for measurements \hat{x} and \hat{p}

For sufficiently amplified fields x , we model the final stage of measurement as a direct detection of the amplified amplitude x at t_f . This model is justified because as the amplification G increases to a macroscopic level, the probability distribution evaluated by sampling over the trajectories for x becomes precisely that of $P_B(x)$, given by quantum mechanics: $Q_{sup}(x, t_f) \rightarrow P_B(x) = |\langle x|\psi\rangle|^2$, as $t_f \rightarrow \infty$. Here, $P_B(x) = |\langle x|\psi\rangle|^2$ gives the Born rule for detecting the value x on measurement of \hat{x} for the system prepared in the state $|\psi\rangle$. This mechanism was explained in Sec. II and is evident in the figures which display the probability for the relative outcomes x_1 or $-x_1$ for the simple superposition (2.14). We give a simple proof below.

Result 1: Consider a general superposition $|\psi_{sup}\rangle = \sum_j c_j |x_j\rangle$ of eigenstates $|x_j\rangle$ of \hat{x} , where c_j are the probability amplitudes. We model the eigenstates as the squeezed states $|\frac{x_j}{2}, r\rangle$ (Eq. (2.12) where $r \rightarrow \infty$). The final density $Q_{sup}(x, t_f)$ given by the Q function for the amplified state $e^{-iH_{amp}t/\hbar}|\psi_{sup}\rangle$, where $H_{amp} = \frac{i\hbar g}{2} [\hat{a}^{\dagger 2} - \hat{a}^2]$, agrees with the prediction of Born's rule, that the probability for detection of outcomes x_j is $|c_j|^2$.

Proof: In the limit of $gt \rightarrow \infty$, the marginal distribution for the amplified state is

$$Q_{sup}(x, t) = \frac{1}{\sqrt{2\pi}\sigma_x(t)} \sum_j |c_j|^2 e^{-(x-G(t)x_j)^2/2\sigma_x^2(t)}$$

where $G = e^{gt}$ ($g > 0$) and $\sigma_x^2(t) = 1 + e^{2gt-2r}$. Defining the scaled variable $\tilde{x} = x/e^{gt}$, this becomes

$$Q_{sc}(\tilde{x}, t) = \frac{1}{\sqrt{2\pi}\sigma_{\tilde{x}}(t)} \sum_j |c_j|^2 e^{-(\tilde{x}-x_j)^2/2(e^{-2gt}+e^{-2r})}$$

which is $\frac{1}{\sqrt{2\pi}\sigma_{\tilde{x}}(t)} \sum_j |c_j|^2 e^{-(\tilde{x}-x_j)^2/(2e^{-2r})}$ on taking gt large. The eigenstates of \hat{x} correspond to $r \rightarrow \infty$ where the Gaussian peaks become infinitely narrow. The separation between peaks is much larger than the width of the Gaussian distributions. Hence, the relative probability for observing x_k is given by the relative weighting of the peaks, $|c_k|^2$, in accordance with Born's rule and the measurement postulate. \square

The scaled marginal for the amplified state becomes $P_B(x)$ because with large amplification the hidden vacuum noise term σ_x^2 of the eigenstate is *not* amplified. The example of validation of $P_B(x) = |\langle x|\psi_{sup}\rangle|^2$ where there is a continuum of states $|x_i\rangle$ is given by the example of the cat state, in Fig. 12.

Result 2: We similarly demonstrate Born’s rule for measurement of $\hat{x}_\theta = \hat{x} \cos \theta + \hat{p} \sin \theta \equiv \hat{a}e^{-i\theta} + \hat{a}^\dagger e^{i\theta}$, for which the complementary observable is $\hat{p}_\theta = -\hat{x} \sin \theta + \hat{p} \cos \theta$.

Proof: We expand in eigenstates $|x_{\theta j}\rangle$ of \hat{x}_θ as $|\psi_{sup}\rangle = \sum_j d_j |x_{\theta j}\rangle$, where d_j are probability amplitudes. We define real coordinates x_θ and p_θ as $\alpha e^{-i\theta} = (x_\theta + ip_\theta)/2$. Using the overlap function [123]

$$\langle x_{\theta j}|\alpha\rangle = \frac{1}{\pi^{1/4}} \exp\left(-\frac{(x_\theta - x_{\theta j})^2}{4} + \frac{ip_\theta}{4}(2x_{\theta j} - x_\theta)\right)$$

the Q function is given by

$$Q(x_\theta, p_\theta) \sim \left| \sum_j d_j e^{-\frac{1}{4}(x_\theta - x_{\theta j})^2} e^{i\frac{p_\theta}{4}(2x_{\theta j} - x_\theta)} \right|^2$$

which for $\theta = \pi/2$ when $x_\theta = p$, becomes

$$Q(x, p) \sim \left| \sum_j d_j e^{-\frac{1}{4}(p - p_j)^2} e^{-i\frac{\pi}{4}(2p_j - p)} \right|^2. \quad (4.13)$$

Modelling the eigenstates as squeezed states in \hat{x}_θ , and changing the amplification so that $H_{amp} = i\hbar g(\hat{a}^{\dagger 2}e^{2i\theta} - \hat{a}^2e^{-2i\theta})$ [which gives $\hat{x}_\theta = e^{2gt}\hat{x}_\theta(0)$], the result is proved applying the same analysis as for Result 1. \square

The realization of Born’s rule for \hat{p} is evident in the examples of Sec. IV.C, shown in Fig. 15.

E. Macroscopic realism and causality

We argue that the phase-space simulations give a model for measurement that is consistent with macroscopic realism (MR). First we define MR.

Definition: *Macroscopic realism (MR):* Consider a system in a superposition, say

$$|\psi_M\rangle = c_1|\psi_1\rangle + c_2|\psi_2\rangle \quad (4.14)$$

of two macroscopically distinct states $|\psi_1\rangle$ and $|\psi_2\rangle$, where c_i are probability amplitudes. The states $|\psi_1\rangle$ and $|\psi_2\rangle$ have definite distinct outcomes for \hat{x} (as in Figs. 2 and 7), which we refer to as +1 and -1. The two states are macroscopically distinguished by the measurement \hat{x} . The premise of MR posits that the system has a definite predetermined outcome $\tilde{\lambda}_x$ for the measurement \hat{x} . That is, each realisation of the system can be regarded as *either* in a state with $\tilde{\lambda}_x = 1$ or $\tilde{\lambda}_x = -1$.

This definition is compatible with the definition of MR given by Leggett and Garg [96], that a system with two or more macroscopically distinct states available to it must

be in one of these state at any time. We do not however suppose any details about the nature of the “state” the system is in, except that there is a definite outcome $\tilde{\lambda}_x$ for the measurement \hat{x} .

A further qualification is made for the definition of MR. In the model, we define the measurement of \hat{x} as a direct *amplification*, of type H_{amp} in Eq. (2.3). This means that any interaction or operation that determines the measurement setting has already occurred. It is assumed that the system at time t_1 is physically prepared with respect to the measurement basis. In the work of Refs. [49, 97, 113, 116], this definition of MR is referred to as *weak macroscopic realism* (wMR). We explain that weak MR is not falsified by violations of macrorealism [96, 97, 109, 110, 131] nor violations of Bell inequalities for macroscopic states [97, 111, 112]. These previous analyses, which have suggested a failure of MR, invoke set-ups where there are further changes of settings, as in a violation of a Bell inequality [97, 111, 112], implying that the system for which MR is considered is subject to further dynamics beyond H_{amp} . Similarly, analyses which violate macrorealism do not violate weak MR, since they involve intervening measurements which require an additional assumption (noninvasiveness measurability).

Result 3: Consistency with macroscopic realism: The simulations motivate a model for measurement in which the final stage of measurement is a direct detection of the amplified amplitude $x(t)$ at the time $t = t_f$ ($t_f \rightarrow \infty$) i.e. that the outcome of the measurement of \hat{x} is inferred from $x(t_f)$. The model is consistent with (weak) *macroscopic realism* (MR).

Proof: We examine the simulation (Figs. 2 and 7) of the measurement \hat{x} on the macroscopic superposition state. There are two parts to this proof: (1) For a given $x(t_f)$, the inferred value for the outcome of \hat{x} is $x(t_f)/G$. This value becomes sharper as $G \rightarrow \infty$, approaching either x_1 or $-x_1$, the relative error δ/G due to the noise δ in the branch becoming negligible. Since in the model, for large enough amplification G , the trajectory value $x(t_f)/G$ is the outcome of the measurement, there is consistency with *macroscopic realism*: This is because the value for the outcome of the measurement is determined at the time t_f , prior to the final detection and readout (which forms the irreversible stage of measurement): the system is in “one or other branch” at time t_f . (2) The second part of the proof is to show *consistency* with the value $x(t_f)/G$ for the outcome (by (1)) being determined at time $t = 0$, prior to the amplification H_{amp} (which is the earlier stage of the measurement process). The trajectories stemming from a positive (or negative) x at the time t_f link directly back to a positive (or negative) x at the present time $t_1 = 0$. There is a *one-to-one correspondence* between the initial and final bands e.g. the outcome x_1 can connect only with values of x that are positive, at $t = 0$. For example, if we detect $x(t_f)$ to be on the branch with inferred outcome given by eigenvalue x_1 , then this corresponds to a value $x(0)$ on the same branch, at $t = 0$. It can also be argued that at

time $t = 0$, since the system is already in a macroscopic superposition, a direct detection and readout would also constitute a measurement of \hat{x} (without further amplification). Then, $x(0)$ is the outcome for the measurement. Hence, in the model, there is consistency with MR, that the value for the outcome is determined by $x(0)$. \square

The system at time $t = 0$ can be identified as being *in one or other branch*, identified by the value of $x(t)$, to give a definite result, either x_1 or $-x_1$, for a future readout of \hat{x}_1 . The value is not sensitive to the hidden vacuum noise contribution δ which depends on the inputs δx or $\xi_x(t)$ at t_f . A hidden variable $\tilde{\lambda}_x$ can be assigned to the system, where the value $\tilde{\lambda}_x = 1$ implies the outcome x_1 for \hat{x} , and the value $\tilde{\lambda}_x = -1$ implies the outcome $-x_1$ for \hat{x} .

Result 4a: Consistency with macroscopic causality: The model is consistent with there being no retrocausality at a macroscopic level.

Proof: Once the system is amplified sufficiently under H_{amp} , the original state $|\psi_{sup}\rangle = \sum_j c_j |x_j\rangle$ becomes $\sum_j e^{-iH_{amp}t/\hbar} |x_j\rangle$ which is a superposition of macroscopically distinct states, for which the *outcome of the measurement* \hat{x} for the system in a macroscopic superposition state is specified (to be $\tilde{\lambda}_x$). This occurs at (or by) a time t_m . The causal relation is that the value $\tilde{\lambda}_x$ determines the measurement outcome subsequently, if there is a final detection (assuming no change of meter settings). The value $\tilde{\lambda}_x$ is fixed in the model for that given time t_m . *There is no change to the value $\tilde{\lambda}_x$ defined at the time t_m due to any future measurement event.* We will extend the Result in Sec. IX to include that the model is consistent with no-signaling. \square

Result 5: Hybrid models: micro-retrocausal and macro-causal: There is a retrocausality at a microscopic level:

Proof: There is retrocausality in the simulations. The selection of the *precise* random noise value $x_f - Gx_j$ is retrocausal because this value originates at the time t_f in the simulation. The constraint on the selection of this noise term is only that of the variance $\sigma_x^2 = 1$ (in units $\hbar = 1$). There is retrocausality at the microscopic level of \hbar , but there is no retrocausality in the sense of a future measurement event or choice of setting θ affecting the present qubit value $\tilde{\lambda}_x$ given for the system in the macroscopic superposition state (4.14) (at time t_1).

V. HIDDEN LOOP: MODEL FOR COLLAPSE OF THE WAVE-FUNCTION

How do the trajectories for the superposition $|\psi_{sup}\rangle$ differ from those of the mixture ρ_{mix} of eigenstates $|x_j\rangle$? Although they propagate independently between times $t_1 = 0$ and t_f , the forward and backwards trajectories are linked according to the correlation given by $Q(x, p, 0)$, at the initial time t_0 . At time $t = t_1$, the Q function (2.16) for the superposition $|\psi_{sup}\rangle$ shows a correlation between

x and p . This is not the case for the mixture ρ_{mix} (2.11), the Q function for the single eigenstate $|x_1\rangle$ factorizing with respect to x and p . The x and p trajectories for the *superposition* (but not for a mixture ρ_{mix}) are therefore correlated i.e. connected. This is the origin of a hidden causal loop (Fig. 2). For the mixture ρ_{mix} , there is no such loop. For H_{amp} , we note that the x and p become decorrelated in the limit as $t_f \rightarrow \infty$.

A. Conditional distribution at the boundary

A given $x(t_f)$ from the time t_f propagates back to a single value of $x(0)$ in the present time, at t_1 . For each such $x(0)$, there is a set of $p(0)$ at time t_1 . This set is given by the conditional distribution $Q(p|x) = Q(x, p, 0)/P(x, 0)$ evaluated from the Q function at $t = t_1 = 0$. Here $Q(x, p, 0)$ is given by Eqs. (2.16) and (4.1) and $P(x, 0)$ is the marginal (4.3) at time $t_1 = 0$. Evaluating for the superposition $|\psi_{sup}(r)\rangle$ (Eq. (2.11)), we find that

$$\begin{aligned} Q(p|x) &= Q(x, p, 0)/P(x, 0) \\ &= \frac{e^{-p^2/2\sigma_p^2}}{\sigma_p\sqrt{2\pi}} \left\{ 1 - \frac{\sin(px_1/\sigma_x^2)}{\cosh(xx_1/\sigma_x^2)} \right\}, \end{aligned} \quad (5.1)$$

which becomes $\sim 1 - \sin(px_1)sech(xx_1)$ for r large. Fringes are evident, becoming finer for large x_1 (which is the separation between the states of the superposition) and also increasingly damped, provided $x \neq 0$. For smaller x_1 , the fringes are more prominent. The conditional distribution implies that the trajectories for x and p are coupled i.e. correlated. For a set of values of $x(t_f)$ at the time t_f , we can match the set with a set of p trajectories, by propagating each given $p(0)$ at time $t_1 = 0$ from the sample generated by $Q(p|x)$, back to the future time t_f . We then have sets of variables $\{x(t_f), x(0), p(0), p(t_f)\}$ and all intermediate values on the trajectories. Such sets of trajectories are plotted in Fig. 16.

The coupling of the p trajectories with those for x is determined by $Q(p|x)$. We ask how does this depend on the outcome of \hat{x} , whether the positive or negative branch? The function $Q(p|x)$ is *independent* of the sign of $x \equiv x(0)$ and hence is not sensitive to the outcome. This is evident in Fig. 16 which plots the distribution for the trajectories of p conditioned on a positive final outcome i.e. $x_f > 0$. Considering the causal relations depicted in Fig. 2, this implies that the conditional relation giving p from δx is not dependent on x_j .

The conditional distribution $Q(p|x)$ for the mixture ρ_{mix} of the two eigenstates is given by

$$Q(p|x) = \frac{e^{-p^2/2\sigma_p^2}}{\sigma_p\sqrt{2\pi}}, \quad (5.2)$$

which implies complete independence of the trajectories for x and p . The coupling of these trajectories at the

boundary $t = t_1$ distinguishes a superposition $|\psi_{sup}\rangle$ from a mixture ρ_{mix} . The trajectories for x follow directly from the marginals $P(x, t_f)$ in each case, and are hence identical (since the $P(x, t_f)$ are identical). This tells us that the causal loop is the feature distinguishing the superposition (*and hence ultimately entanglement*) from the mixed state.

B. Inferred initial state for x and p post-selected on a measurement outcome x_j

We ask what happens if we post-select on the condition that the final outcome of the measurement \hat{x} is x_1 : that is, $x_f > 0$? We next consider the joint distribution $Q_{loop}(x, p|x_j)$ for the values x and p at the time $t = t_1 = 0$ that connect to the branch corresponding to the outcome x_j i.e. the distribution for the sets of connected trajectories for x and p , based on the post-selected outcome x_j for the measurement \hat{x} . Here, we will consider $x_j = x_1$, which is the positive outcome for \hat{x} , and evaluate the inferred distribution

$$Q_{loop}(x, p|x_1) \equiv Q(x, p|x(t_f) > 0)$$

as $gt \rightarrow \infty$. We will denote $Q_{loop}(x, p|x_1)$ where x_1 is positive by $Q_+(x, p, t_0)$.

The distribution $Q_+(x, p, 0)$ can be interpreted in the model for reality that we give for measurement as describing the “state” inferred at time $t_1 = 0$, given the positive outcome x_1 for \hat{x} . We evaluate the variances $\sigma_{x,+}^2$ and $\sigma_{p,+}^2$ of the inferred distribution $Q_{loop}(x, p|x_1) \equiv Q_+(x, p, 0)$, and show that they correspond to variances below the level allowed by the Heisenberg uncertainty principle.

We proceed as follows. For sufficiently large gt , each x_f is either positive or negative, associated with the outcome x_1 or $-x_1$ which we denote by $+$ or $-$. We trace the trajectories in x back to the time $t_1 = 0$ given the post-selection of $x_f > 0$, and construct the distribution of x at time $t_0 = 0$ for all such trajectories. At the boundary in the present time $t_0 = 0$, each value of x is connected to a set of trajectories in p , according to (5.1). The distribution for the forward-trajectories $p(t)$ versus gt can be evaluated, but is independent of the outcome (whether x_1 or $-x_1$). This is because the conditional $Q(p|x)$ is independent of sign of x . The distribution is hence identical to that given by Fig. 9.

We next construct the joint distribution $Q_+(x, p, 0)$ describing the correlated values in x and p at the time $t_1 = 0$, conditioned on the positive outcome for \hat{x} (Fig. 4). (In practice, we have taken the superposition (2.14) with $r = 2$). We then determine the variances $\sigma_{x,+}^2 \equiv \sigma_{x,+}^2(0)$ and $\sigma_{p,+}^2 \equiv \sigma_{p,+}^2(0)$ for x and p for this distribution, and define the observed variance for the x and p once anti-normal ordering is accounted for:

$$\begin{aligned} [\Delta(x|+)]^2 &= \sigma_{x,+}^2(0) - 1 \\ [\Delta(p|+)]^2 &= \sigma_{p,+}^2(0) - 1. \end{aligned} \quad (5.3)$$

Similar variances $\sigma_{x,-}^2(0)$, $\sigma_{p,-}^2(0)$, $[\Delta(x|-)]^2$ and $[\Delta(p|-)]^2$ could be determined for the trajectories post-selected on the $x_f < 0$ corresponding to the outcome $-x_1$. This tells us what we infer about the original state (in the reality model) at time $t = 0$ based on the measurement outcome, whether $+$ or $-$. By subtracting the vacuum term 1 associated with the anti-normal ordering operators, we evaluate the variances that would be associated with a measurement of \hat{x} . The variances are given in Fig. 17 versus x_1 (which gives the separation between the states of the superposition) for a large value of gt . We also define the uncertainty product for the inferred initial state:

$$\epsilon = \Delta(x_p|+)\Delta(p_p|+). \quad (5.4)$$

From the Figs. 17, see that $\epsilon < 1$ for all x_1 (and α_0) although $\epsilon \rightarrow 1$ as $x_1 \rightarrow \infty$.

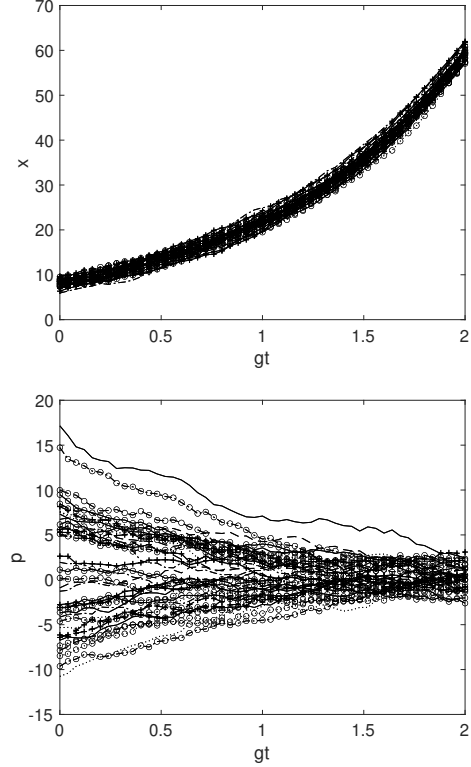


Figure 16. Connected trajectories forming a loop: Plots show trajectories for x and p for the system prepared in a superposition $|\psi_{sup}\rangle$, conditioned on a positive outcome for measurement of \hat{x} , with $x_1 = 8$ and $t_f = 2/g$. We approximate $|\psi_{sup}\rangle$ by $|\psi_{sup}(r)\rangle$ of (2.14) with $r = 2$.

The figures show what happens if we post-select on the positive outcome, x_1 , for a measurement of \hat{x} . This result is highly sensitive to the initial separation (given by x_1) of the eigenstates, or of the coherent states $|\alpha_0\rangle$ and $|- \alpha_0\rangle$. For the cat state where $r = 0$ and $x_1 = 2\alpha_0$ is large, the x -variance $[\Delta(x_p|+)]^2$ is reduced almost to the vacuum level of 1, as would be expected. This is explained as

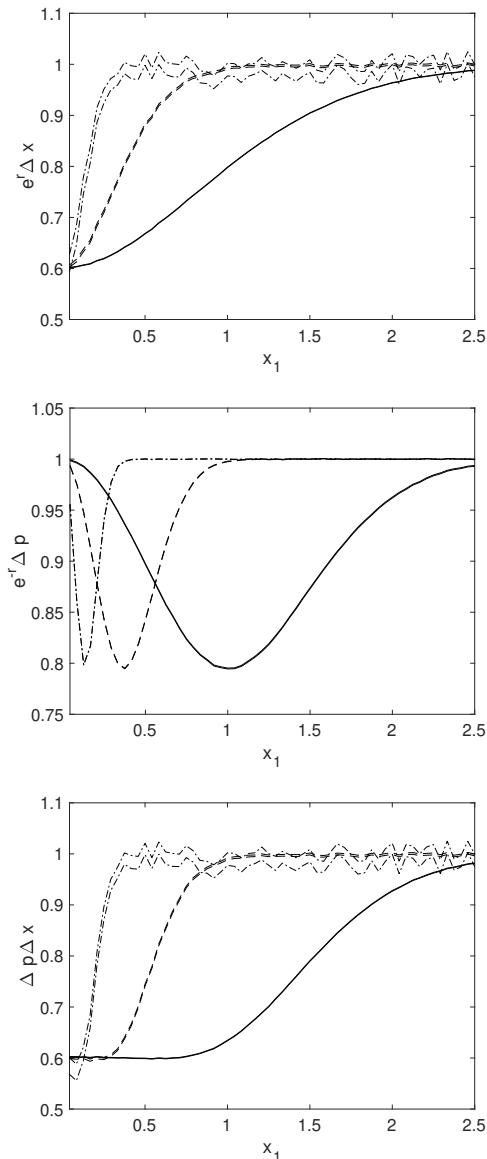


Figure 17. Here we plot the variances $\Delta(x_p|x_f > 0)$, $\Delta(p_p|x_f > 0)$ and the uncertainty product $\epsilon = \Delta(x_p|x_f > 0)\Delta(p_p|x_f > 0)$ conditioned on a positive outcome x_1 for \hat{x} , using Eq. (2.14). The upper dashed-dotted line is for a superposition $|\psi_{sup}\rangle$ of two eigenstates of \hat{x} with $r = 2$. The dashed line is for $|\psi_{sup}(r)\rangle$ with $r = 1$. The solid line is for $r = 0$. In each case, $gt = 4$, which corresponds to an effective measurement of \hat{x} . The two parallel lines indicate the upper and lower error bounds from sampling errors, with 1.2×10^7 trajectories.

follows. The overall variance in x at the time $t_0 = 0$ is large, due to there being two states comprising the superposition, but the final amplified outcome of either $x_1 = 2\alpha_0$ or $-x_1 = -2\alpha_0$ (Fig. 12) links the trajectory back to only *one* of these states, $|\alpha_0\rangle$ or $|- \alpha_0\rangle$, which has a variance in x of 1.

A further reduction for the variance in x is observed

because of the truncation that occurs with the Gaussian function at t_f . The conditioning is done for $x(t_f) > 0$, which does not take account of the negative values in $x(t_f)$ associated with the Gaussian centered at $x(t_f) = gx_1$. This effect becomes negligible for a superposition of true eigenstates of \hat{x} ($r \rightarrow \infty$) in the limit of a true measurement corresponding to $gt \rightarrow \infty$, as observed when comparing the results of Fig. 17. However, the variance $[\Delta(p_p|+)]^2$ in p occurs from the distribution for p that has interference fringes. This is more pronounced with smaller separation x_1 . The fringe pattern leads to a reduction in the variance, as compared to the simple Gaussian in p [132, 133]. This effect is stable for gt and r , although at greater r we see that the optimal dip in the variance occurs at smaller separations x_1 of eigenstates.

The overall result is that the Heisenberg uncertainty principle is *not* satisfied for the coupled x and p trajectories: i.e., the post-selected Q function distribution $Q_+(x, p, 0)$ does not reflect a quantum state $|\psi\rangle$. Due to the fringes becoming finer as $x_1 \rightarrow \infty$, the product approaches 1 with increasing separation of the eigenstates. This reveals that the variables x and p , if we identify them as “hidden variables”, are *inconsistent* with a quantum state (i.e. as given by a wave-function), but become consistent in the limit of large x_1 , where one has a true macroscopic superposition – a “cat state”.

C. Collapse to the eigenstate and the measurement problem

The solutions of this paper give a model for measurement that explains the measurement postulates. The probability density of the amplified amplitudes $x(t_f)$ corresponds to the probability of outcomes deduced from Borns’ rule (Sec. IV.D). In the model, macroscopic realism emerges as the system is amplified and the inferred outcome $x(t_f)/G$ will be one of the eigenvalues x_j .

In the model, we see that amplification also contributes an explanation of the “collapse” of the wave-function. As the system is amplified, a general superposition $|\psi_{sup}\rangle$ will evolve into a macroscopic superposition (Fig. 1, top left). Results from Sec. V.B (Fig. 17) indicate that for a macroscopic superposition (where x_1 is large), the inferred state conditioned on the branch with outcome x_j approaches the eigenstate $|x_j\rangle$, as predicted by the measurement postulates.

However, the amplification H_{amp} that creates the macroscopic superposition state is a *reversible* process. The complete “collapse” to the eigenstate occurs when the process is *not reversible*. In the model, we see that this occurs when information about the complementary variable p is removed at the final detection. In the calculations, this corresponds to integrating the distribution $Q_{loop}(x, p|x_j)$ for the inferred state (given an outcome x_j) over p . The integration over p reduces the distribution Q_{loop} to the Q function of the eigenstate $|x_j\rangle$. A more precise model would allow for a coupling to a meter, as

outlined in Appendix E. The example of a spin coupled to a meter is analyzed in Ref. [122].

VI. CAUSAL STRUCTURE

The simulations involve classical-like amplitudes and individual realizations, and hence we can identify a causal model associated with the procedure of the simulation. The causal relations for the simulation of the measurements \hat{x} or \hat{p} on a system prepared in a superposition of eigenstates are depicted in Fig. 18. We select the simplest relations.

We denote the measurement by \hat{X} , where \hat{X} is either \hat{x} or \hat{p} . The model parameters are the measurement setting θ (in this case, the choice to measure either \hat{x} or \hat{p}) and the variables that describe the state of the system, at the times $t = t_1 = 0$, and $t = t_f$, as well as the noise inputs δx , $\xi_1(t)$ and $\xi_2(t)$. Where we measure \hat{x} , the notation implies $\xi_1(t) \equiv \xi_x(t)$ and $\xi_2(t) \equiv \xi_p(t)$.

The Q function specifies the system variables at time $t_1 = 0$ (or just prior) to be x and p , with joint probability $Q(x, p, t_1)$. To proceed with the simulation, the backward trajectories originate from the *future marginal* that represents the amplified state. This marginal is *subject to the choice of measurement setting* θ and can be derived from the dynamical equation for the Q function. The Q function for a state of the system is unique, but can be written as a superposition of either eigenstates $|x_j\rangle$ or $|p_k\rangle$ as given by equations (2.10) and (4.13) which have a similar form.

Case I: $\varphi = \pi/2$: As we have seen (for $\varphi = \pi/2$) the solutions show that the future marginal (and hence the future boundary condition) is identical to that of the mixture ρ_{mix} of eigenstates of \hat{X} , for which the system is probabilistically in a state with a definite outcome for the measurement \hat{X} , the outcomes being one of the eigenvalues λ . The procedure of sampling for the *backwards* trajectories is hence identical to that used for the mixed state: Each individual trajectory (or run) is specified by a value of λ , the value being one of the set of eigenvalues $\{x_j\}$ (or $\{p_j\}$) of the measurement \hat{x} (or \hat{p}).

The relative weighting for λ in the simulations is determined by the future marginal, and from that we see is given by the probability amplitudes, consistent with Born's rule. We define the conditional $P(\lambda|\theta)$, where $P(\lambda = x_j) = |c_j|^2$ if $\theta \equiv \hat{x}$ and $P(\lambda = p_j) = |d_j|^2$ if $\theta \equiv \hat{p}$. Here, $|c_j|$ and $|d_j|$ are determined by the Q function $Q(x, p)$, from the marginals $P(x)$ (or $P(p)$) found by integrating over the complementary variable p (or x). The variable λ is conditional on the setting θ . We consider at time t_1 that the setting is determined by an interaction with some part of the measurement apparatus, as in a choice of phase. Hence, we do *not* define an underlying joint distribution $P(\lambda_x, \lambda_p)$ for variables that correspond to $\lambda = \lambda_x$ if $\theta \equiv \hat{x}$, and $\lambda = \lambda_p$ if $\theta \equiv \hat{p}$.

The final measured outcome value will be X , which is the *amplified value* of λ . In the model, X is a system

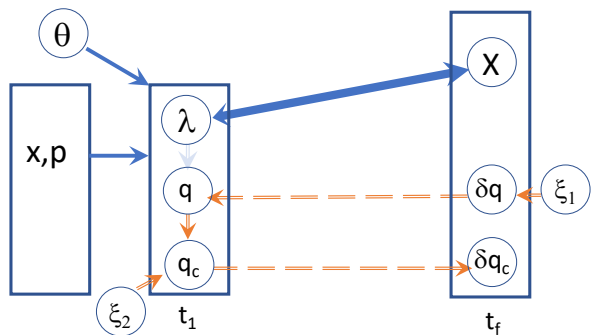


Figure 18. Macro-micro causal relations for the simulation given by the trajectories shown in the figures of this paper. The joint probability for x and p is given by $Q(x, p)$. The θ is the measurement setting, determining whether \hat{x} or \hat{p} is measured, and λ is an eigenvalue x_j (or p_j) of \hat{x} (or \hat{p}) depending on the setting θ . X is the amplified system variable at the time t_f which corresponds to the outcome of measurement. The relation between λ and X is deterministic, X being a direct amplification of the eigenvalue. Here, δq represents the (unmeasurable) fluctuation at time t_f , (determined as a Gaussian input \mathcal{G} independent of θ and λ) which is linked back to the measured variable (x or p) at time t_1 . If, for instance, θ corresponds to \hat{x} , the conditional distribution $Q(p|x)$ at $t = t_1 = 0$ given by (5.1) determines the conditional relation between $q \equiv x$ and $q_c \equiv p$, which is the correlation specified by x, p at time t_1 . That relation then determines the relation for the (unmeasurable) fluctuation δq_c at time t_f . The noise input $\xi_1(t_f)$ is independent of θ .

variable at the time t_f . The relation between X and λ (and θ) is deterministic, ie.

$$X = e^{|g|t} \lambda, \quad (6.1)$$

where $\lambda = x_j$ for some j , if $\theta \equiv \hat{x}$; and $\lambda = p_j$ for some j , if $\theta \equiv \hat{p}$. This causal deterministic relation is represented by the blue forward-going solid arrow in Fig. 18. With the choice of θ , there is a value λ selected, with a certain probability. This may be regarded as a macroscopic causal relation since it relates to a measured quantity. It is important to note that in the simulation, because the relation is deterministic, it can also be considered a backward relation. Hence the solid blue two-way arrows in Figs. 18 and 2.

The system at time t_f includes the fluctuations δq that are not measured by amplification (here q is either x or p). The value of δq is then sampled using a random Gaussian function \mathcal{G} with mean 0 and variance $\sigma_x^2 = 1$ at time t_f . Hence

$$P(\delta q(t_f)) \equiv \mathcal{G}(0, \sigma_x). \quad (6.2)$$

The value of the system variable q is $q = q_j + \delta q(t_f)$, and q_j is either $x_j e^{|g|t_f}$ or $p_j e^{|g|t_f}$, depending on the value of θ . The backward trajectory is given by

$$\frac{dq}{dt_-} = -|g|q + \sqrt{2g}\xi_1(t), \quad (6.3)$$

as in (6.4), with the initial condition being the value of q at time t_f . The Gaussian random noise $\xi_1(t)$ satisfies $\langle \xi_1(t) \xi_1(t') \rangle = \delta(t - t')$ and decouples from the complementary variable q_c (which is either p or x). We note however we can solve (6.4) by substituting $q = q_0 + \delta q$, where q_0 satisfies

$$\frac{dq_0}{dt_-} = -|g|q_0 \quad (6.4)$$

with initial condition $q_0(t_f) = q_j$, and

$$\frac{d(\delta q)}{dt_-} = -|g|\delta q + \sqrt{2g}\xi_1(t), \quad (6.5)$$

with initial condition $\delta q = \delta q(t_f)$. Clearly, the solution for q_0 is the deterministic function $q_0 = q_j e^{-|g|t_-}$, which is either $q_0 = x_j e^{|g|(t_f - t_-)}$ or $q_0 = p_j e^{|g|(t_f - t_-)}$ depending on the value of θ . This decaying solution with respect to t_- is evident in the trajectories for x plotted in Figs. 1 and 7. The trajectory for δq has a stochastic solution involving the noise ξ_1 . This noise does *not* depend on the value of q_0 or q . The consequence is that the δq has the same initial condition and trajectory equations, regardless of setting θ .

The trajectory for δq propagates back to t_1 with a value $\delta q(t_1) = q_p$ (in the present time). Hence, we write

$$P(\delta q(t_1)) \equiv P(\delta q(t_1)|\delta q(t_f)), \quad (6.6)$$

noting that the noise value δq is at the vacuum level, *independent* of the value of the outcome X and *independent* of the measurement setting θ . This defines the microscopic backward retrocausal relation marked by the red dashed arrow in the Fig. 18. The lack of dependence on the setting θ may be part of the explanation for the lack of any observable macroscopic retrocausality, where it might be supposed that a choice of measurement setting can affect the value of λ .

Causal loop: However, q is either x or p - which is determined at the present time t_1 , from θ . The value of the complementary variable that is not measured is denoted q_c . Here, q_c is either p or x . The value $\delta q_c(t_0)$ can be specified according to the conditional $Q(q_c|q)$ at time t_1 . The $\delta q(t_1)$ defines the value of q at time t_1 : $q = \lambda + \delta q(t_1)$. This determines q_c at time t_1 . Denoting the values of x and p at time t_1 as $x(t_1) = x_p$ and $p(t_1) = p_p$ (meaning x and p in the present time), we write if $q = x$ and $q_c = p$ that

$$Q(p(t_1)|x(t_1)) = Q(p(t_1)|x(t_1)) \equiv Q(p_p|x_p), \quad (6.7)$$

and if $q = p$ and $q_c = x$ that $Q(x(t_1)|p(t_1)) = Q(x(t_1)|p(t_1)) \equiv Q(x_p|p_p)$. This conditional relation is given by the short red downward arrow at the boundary $t = t_1$ in Fig. 18, which creates the loop. The value of $q_c(t_1)$ determines the starting point of the trajectory that results in a value $q_c(t_f)$ for the complementary variable q_c at time t_f . The probability

$$P(q_c(t_f)|q_c(t_1)) \quad (6.8)$$

is defined stochastically by the forward dynamics given by equation (3.2), which involves the noise function ξ_2 . This relation is causal and is marked on Fig. 18 by the forward arrow. The relations given by the orange dashed arrows can be regarded as microscopic, or hidden, since they govern quantities unobservable under H_{amp} .

Case II: $\varphi \neq \pi/2$ For different values of φ , the sinusoidal \mathcal{I} term in the Q function for a superposition (as in (2.16) for eigenstates of x) can contribute a cosine rather than a sine term, which also appears in the expression (4.1). When integrated over the complementary variable $q_c = p$, this adds an extra infinitesimal Gaussian term in the marginal (4.3) for $q = x$, which strictly needs to be included in the future boundary condition. This needs further study. While the Gaussian at time t_f is infinitesimal, being damped with amplification, the term Gaussian amplifies in the time reversed direction, from t_f to t_1 . Derived from the \mathcal{I} , it can depend on the settings, as determined by the Q function at time t_1 .

In this paper, we use the term ‘‘causal loop’’ to describe the feedback between the backwards and forward trajectories. This suggests that the value of the complementary variable q_c is *caused* by q . In fact, the simulation proceeds based on a *correlation* between q and q_c , as given by the initial Q function. This correlation is absent for the mixed state (2.11). In [122], the stochastic equations that describe the creation of a superposition state (in the form of entanglement of two systems) are solved. There we find that the correlation in the Q function appears as a result of input noise that is shared as the entanglement is formed.

For the particular Hamiltonian H_{amp} , the equations for x and p decouple at time t_f , which simplifies the nature of the ‘‘causal loop’’. The x and p variables decorrelate with time t_f , as $t_f \rightarrow \infty$. The loop is hence disconnected with respect to x and p at the future boundary. There is no further feedback from p into x . The consistency of the correlations with those of $Q(x, p, t)$, as solved from the Hamiltonian H_{amp} , has been verified (refer Appendix). For more complicated interactions, the variables x and p need not decouple, and a cyclic causation emerges [122].

VII. CONTINUOUS-VARIABLE EPR ENTANGLEMENT

The theorems and stochastic equations derived in Secs. II-III and Appendix A can be applied to treat bipartite systems. In this paper, we examine entanglement and nonlocality as detected using measurements of \hat{x} and \hat{p} .

Einstein, Podolsky and Rosen (EPR) presented an argument on the completion of quantum mechanics in 1935 [101]. The argument can be realised for two separated field modes A and B . Two modes prepared in a two-mode squeezed state

$$|\psi_{epr}\rangle = (1 - \eta^2)^{1/2} \sum_{n=0}^{\infty} \tanh^n r |n\rangle_A |n\rangle_B \quad (7.1)$$

at time t_0 possess EPR correlations [134]. Here $\eta = \tanh r$ where r is the squeeze parameter, and $|n\rangle_{A/B}$ are number states. Boson operators \hat{a} , \hat{b} and quadrature phase amplitudes \hat{x}_A , \hat{p}_A , \hat{x}_B and \hat{p}_B are defined for each mode, where $\hat{x}_A = \hat{a} + \hat{a}^\dagger$, $\hat{x}_B = \hat{b} + \hat{b}^\dagger$, $\hat{p}_A = (\hat{a} - \hat{a}^\dagger)/i$, $\hat{p}_B = (\hat{b} - \hat{b}^\dagger)/i$. The Q function for the two-mode quantum state $|\psi\rangle$ is defined as $Q(\alpha, \beta) = \frac{1}{\pi^2} |\langle \alpha | \langle \beta | \psi \rangle|^2$ where $|\alpha\rangle$ and $|\beta\rangle$ are coherent states of modes A and B respectively. Introducing real coordinates $x_A = \alpha + \alpha^*$, $p_A = (\alpha - \alpha^*)/i$, $x_B = \beta + \beta^*$, $p_B = (\beta - \beta^*)/i$, the Q function of $|\psi_{\text{EPR}}\rangle$ is

$$Q_{\text{EPR}}(\boldsymbol{\lambda}, t_0) = \frac{(1 - \eta^2)}{16\pi^2} e^{-\frac{1}{8}(x_A - x_B)^2(1+\eta)} e^{-\frac{1}{8}(p_A + p_B)^2(1+\eta)} \times e^{-\frac{1}{8}(x_A + x_B)^2(1-\eta)} e^{-\frac{1}{8}(p_A - p_B)^2(1-\eta)} \quad (7.2)$$

where $\boldsymbol{\lambda} = (x_A, x_B, p_A, p_B)$. As $r \rightarrow \infty$, $|\psi_{\text{EPR}}\rangle$ is an eigenstate of $\hat{x}_A - \hat{x}_B$ and $\hat{p}_A + \hat{p}_B$. Following Sections II-III, a measurement of \hat{x}_A or \hat{p}_A is modelled as a direct amplification, given by the Hamiltonian

$$H_{\text{amp}}^A = i\hbar g e^{2i\theta} (\hat{a}^{\dagger 2} - \hat{a}^2)/2 \quad (7.3)$$

with $g > 0$ and $\theta = 0$ or $\pi/2$ respectively. Similarly, $H_{\text{amp}}^B = i\hbar g e^{2i\phi} (\hat{b}^{\dagger 2} - \hat{b}^2)/2$ with $\phi = 0$ or $\pi/2$ allowing measurement of \hat{x}_B or \hat{p}_B .

First we consider joint measurements of \hat{x}_A and \hat{x}_B . Following Sections III, the stochastic equations for the measurements \hat{x}_A and \hat{x}_B are ($K \in \{A, B\}$)

$$\frac{dx_K}{dt_-} = -gx_K + \xi_{K1}(t) \quad (7.4)$$

with boundary conditions in the future t_f and $\frac{dp_K}{dt} = -gp_K + \xi_{K2}(t)$ with boundary conditions in the past. The noises satisfy $\langle \xi_{K\mu}(t) \xi_{K\nu}(t') \rangle = 2|g|\delta_{\mu\nu}\delta(t-t')$, with noise terms for A and B being independent, with magnitudes independent of the measurement setting, whether \hat{x}_K or \hat{p}_k .

The equations can be solved by transforming to $x_{\pm} = x_A \pm x_B$, $p_{\pm} = p_A \pm p_B$. The dynamical equations for x_+ and x_- are

$$\frac{dx_{\pm}}{dt_-} = -gx_{\pm} + \xi_{1\pm}(t) \quad (7.5)$$

with future boundary conditions. Those for p_+ and p_- are $\frac{dp_{\pm}}{dt} = -gp_{\pm} + \xi_{2\pm}(t)$ with boundary conditions at the initial time. Here $\langle \xi_{\mu+}(t) \xi_{\nu+}(t') \rangle = 4|g|\delta_{\mu\nu}\delta(t-t')$ and $\langle \xi_{\mu-}(t) \xi_{\nu-}(t') \rangle = 4|g|\delta_{\mu\nu}\delta(t-t')$ and cross-terms are zero. We examine the solutions for x_{\pm} , since these are of most interest to us, representing the amplified, or measured, quantities. As in previous examples, the dynamics for the x and p separate, so that the amplification of x is determined by the marginals for x_A and x_B . The original distribution (7.2) is a function of x_+ , x_- , p_+ and p_- . Transforming to these variables, the marginal for x_+ and x_- at time t_1 is

$$Q(x_+, x_-, 0) = \frac{1}{2\pi\sigma_+(0)\sigma_-(0)} e^{-x_-^2/2\sigma_-^2(0)} e^{-x_+^2/2\sigma_+^2(0)} \quad (7.6)$$

where $\sigma_{\pm}^2(0) = 2(1 + e^{\mp 2r})$. This function is separable in x_- and x_+ . The boundary condition for the backwards trajectories of x_{\pm} is determined by the marginal at t_f :

$$Q(x_+, x_-, t_f) = \frac{e^{-x_-^2/2\sigma_-^2(t_f)} e^{-x_+^2/2\sigma_+^2(t_f)}}{2\pi\sigma_+(t_f)\sigma_-(t_f)} \quad (7.7)$$

where the gain is $G(t) = e^{gt}$ and the variances are $\sigma_{\pm}^2(t) = 2 + G^2(t) [\sigma_{\pm}^2(0) - 2]$, rewritten as

$$\sigma_{\pm}^2(t) = 2(1 + e^{2|g|t} e^{\pm 2r}). \quad (7.8)$$

The value $\sigma_{\pm}^2(t) = 2$ is the hidden vacuum noise level associated with the Q function.

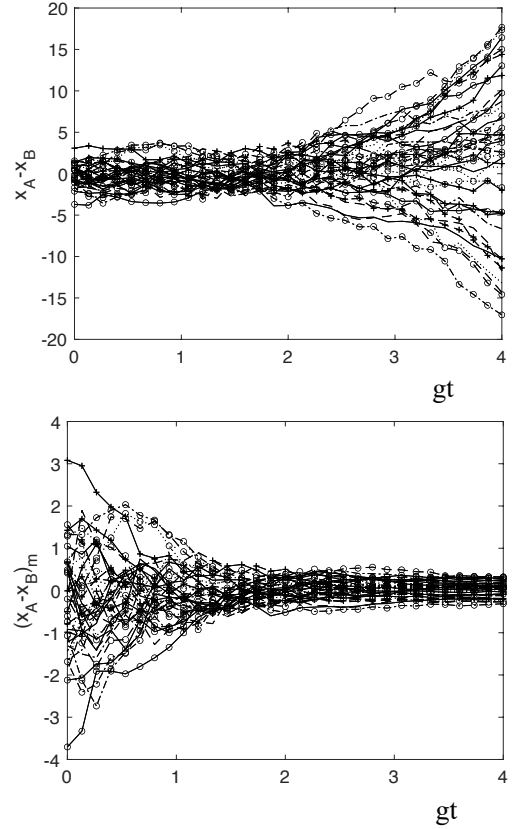


Figure 19. Simulations for the joint measurement of \hat{x}_A and \hat{x}_B on the EPR state $|\psi_{\text{EPR}}\rangle$. The top figure shows trajectories of x_- . The lower figure shows trajectories scaled according to $(x_A - x_B)_m \equiv \bar{x}_- = x_-/e^{gt}$ which is the inferred (“measured”) outcome of the measurement $\hat{x}_- = \hat{x}_A - \hat{x}_B$, as $gt \rightarrow \infty$. Here $r = 2$.

The results of the simulations for x_{\pm} are shown in Figs. 19 and 20. The solutions for x_- reveal the correlation for the EPR state between x_A and x_B . The variance $\sigma_{\pm}^2(t)$ increases with gt due to the gain associated with the measurement. However, the trajectories when scaled according to the amplification factor $G = e^{gt}$ reveal a reduced variance $\sigma_{\pm}^2(t)/G^2 = 2(e^{-2|g|t} + e^{\pm 2r})$. This is consistent with the prediction of zero variance

in the measured quantity \hat{x}_- (Fig. 21). On the other hand, there is an enhanced variance in x_+ beyond that of the vacuum state (as the x_A and x_B are uncorrelated), which becomes larger with measurement, which amplifies the field. The agreement with quantum predictions for the measurements of \hat{x}_A and \hat{x}_B modelled by H_{amp}^K can be demonstrated by introducing the scaled variables $\bar{x}_\pm = x_\pm/e^{gt}$ and $\bar{x}_{A/B} = x_{A/B}/e^{|g|t}$. In the large amplification limit, $\sigma_+^2(t) \rightarrow 2e^{2|g|t+2r}$ and the marginal becomes,

$$\begin{aligned} Q(\bar{x}_+, \bar{x}_-, t_f) &= \frac{e^{-\bar{x}_-^2/(4(e^{-2|g|t} + e^{-2r}))} e^{-\bar{x}_+^2/4e^{2r}}}{2\pi\bar{\sigma}_+(t_f)\bar{\sigma}_-(t_f)} \\ &\rightarrow \frac{1}{4\pi} e^{-\bar{x}_-^2/(4e^{-2r})} e^{-\bar{x}_+^2/4e^{2r}} \end{aligned} \quad (7.9)$$

where we take $gt \rightarrow \infty$ and $\bar{\sigma}_\pm^2(t_f) = 2e^{\pm 2r}$. Once the amplification factor $G = e^{gt}$ is accounted for in the measurement, the final distributions for x_- and x_+ are

$$Q(\tilde{x}_\mp, t_f) = \frac{1}{2e^{\mp r}\sqrt{\pi}} e^{-\tilde{x}_\mp^2/(4e^{\mp 2r})} \quad (7.10)$$

with mean zero and variance $2e^{\mp 2r}$. This is because the hidden vacuum noise terms associated with the Q function, as given by $\sigma_\pm^2(t) = 2$ in the expression (7.8) for $\sigma_\pm^2(t)$, become indiscernible. The limiting variances give precisely the distributions predicted from quantum mechanics. The two-mode squeezed state $|\psi_{epr}\rangle$ predicts $[\Delta(\hat{x}_\pm)]^2 = 2e^{\pm 2r}$, consistent with the observed distribution (Fig. 21).

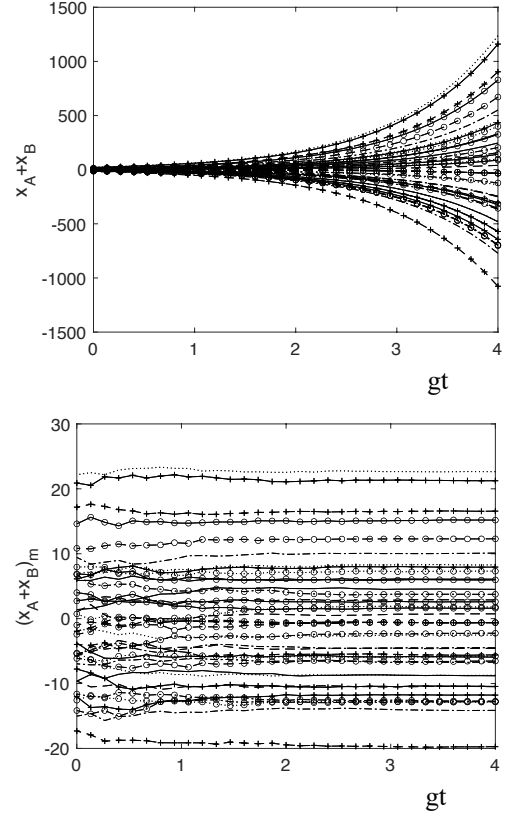


Figure 20. Measurement of \hat{x}_A and \hat{x}_B on the EPR state $|\psi_{epr}\rangle$. The top figure shows trajectories of x_+ . The lower figure plots trajectories of the scaled value $(x_A + x_B)_m \equiv \bar{x}_+ = x_+/e^{gt}$, which becomes the inferred (“measured”) outcome of the measurement $\hat{x}_+ = \hat{x}_A + \hat{x}_B$, as $gt \rightarrow \infty$. Here, $r = 2$.

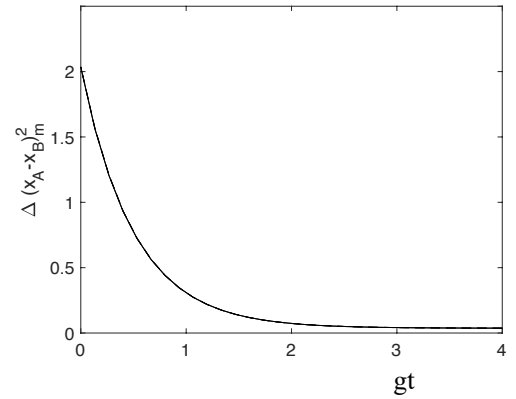


Figure 21. The plot of the variance of the measured values $(x_A - x_B)_m = (x_A - x_B)/e^{gt}$ versus gt . Here, $r = 2$.

The solutions for x_A and x_B are found as $x_A = (x_+ + x_-)/2$ and $x_B = (x_+ - x_-)/2$. For large amplification gt , the solutions are dominated by those of x_+ . In Fig. 22, we plot x_A and x_B , using the same colour for the same run of the simulation. The correlation is evident.

The EPR argument is based not only on the perfect

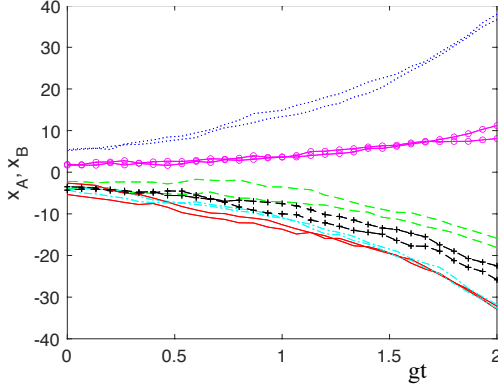


Figure 22. Measurement of \hat{x}_A and \hat{x}_B on the EPR state $|\psi_{\text{EPR}}\rangle$. The figure shows trajectories for x_A and x_B . The pair (x_A, x_B) corresponding to the same run are shown with the same colour (and symbol). The inferred outcome of \hat{x}_A is the value $x_A(t)/e^{gt}$. Similarly, the outcome for \hat{x}_B is $x_B(t)/e^{gt}$. For large r and $G = e^{gt}$, the correlation between x_A and x_B is perfect so that the outcome for \hat{x}_A can be inferred from \hat{x}_B . The trajectories p_A and $-p_B$ for the joint measurement of \hat{p}_A and $-\hat{p}_B$ show the same behavior as those for x_A and x_B , satisfying the same equations.

correlation between \hat{x}_A and \hat{x}_B but also on the the perfect anti-correlation between \hat{p}_A and \hat{p}_B . The stochastic equations for joint measurements of \hat{p}_A and \hat{p}_B are

$$\frac{dp_K}{dt_-} = -gp_K + \xi_{K1}(t) \quad (7.11)$$

and $\frac{dx_K}{dt} = -gx_K + \xi_{K2}(t)$. The equations of interest are those for p_K since these give solutions for the amplified variables that are measured. The marginal for p_{\pm} for the initial state (7.2) is

$$Q(p_-, p_+, 0) = \frac{e^{-p_-^2/2\sigma_+^2(0)} e^{-p_+^2/2\sigma_-^2(0)}}{2\pi\sigma_+(0)\sigma_-(0)} \quad (7.12)$$

where $\sigma_{\mp}^2(0) = 2(1 + e^{\mp 2r})$. The fluctuations are decreased in p_+ . The marginal used for the backwards equation (7.11) is hence

$$Q(p_+, p_-, t_f) = \frac{e^{-p_+^2/2\sigma_+^2(t_f)} e^{-p_-^2/2\sigma_-^2(t_f)}}{2\pi\sigma_+(t_f)\sigma_-(t_f)} \quad (7.13)$$

where the gain is $G(t) = e^{|g|t}$ and the variances are $\sigma_{\pm}^2(t) = 2(1 + e^{2|g|t} e^{\pm 2r})$. The $Q(p_-, p_+, t_f)$ is the same as $Q(x_+, x_-, t_f)$ but replacing x_+ with p_- , and x_- with

p_+ . The solutions for trajectories for measurement of \hat{p}_A and \hat{p}_B are hence the same as those for x_{\pm} , but with p_{\pm} replacing x_{\mp} .

VIII. CV BELL NONLOCALITY

The demonstration of Bell nonlocality involves a choice of measurement setting θ and ϕ for each system, A and B . In this paper, we examine measurements of \hat{x} and \hat{p} , for which the outcomes are continuous variables (CV). It is known that certain states will violate a Bell inequality for such measurements [135–138]. We define the quadrature phase amplitude measurements as $\hat{x}_{\theta A} = \hat{a}e^{-i\theta} + \hat{a}^{\dagger}e^{i\theta}$ and $\hat{x}_{\phi B} = \hat{b}e^{-i\phi} + \hat{b}^{\dagger}e^{i\phi}$ i.e.

$$\begin{aligned} \hat{x}_{\theta A} &= \hat{x}_A \cos \theta + \hat{p}_A \sin \theta \\ \hat{p}_{\theta A} &= -\hat{x}_A \sin \theta + \hat{p}_A \cos \theta \end{aligned} \quad (8.1)$$

for system A and

$$\begin{aligned} \hat{x}_{\phi B} &= \hat{x}_B \cos \phi + \hat{p}_B \sin \phi \\ \hat{p}_{\phi B} &= -\hat{x}_B \sin \phi + \hat{p}_B \cos \phi \end{aligned} \quad (8.2)$$

for system B . Putting $\theta = 0$, we see that $\hat{x}_{0,A} = \hat{x}_A$. Similarly, putting $\theta = \pi/2$, we find $\hat{x}_{\pi/2,A} = \hat{p}_A$ and $\hat{p}_{\pi/2,A} = \hat{x}_{\theta+\pi/2,A}$. Similarly $\hat{x}_{\pi/2,B} = \hat{p}_B$ and $\hat{p}_{\phi B} = \hat{x}_{\phi+\pi/2,B}$.

The outcomes for the amplitudes may be binned to be $+1$ or -1 , according to the sign of the outcome. The assumption of local hidden variable theories allows a Bell inequality to be derived as for spins [135, 136]. An example of a state that will violate the inequality is the squeezed cat state [137],

$$|\psi_B\rangle = N_0^2 e^{-iH_I t_I/\hbar} (|\alpha_0\rangle_A |\alpha_0\rangle_B + |-\alpha_0\rangle_A |-\alpha_0\rangle_B) \quad (8.3)$$

where $H_I = i\kappa\hbar(\hat{a}^{\dagger}\hat{b}^{\dagger} - \hat{a}\hat{b})$, $N_0^2 = 1/[2(1 + e^{-4|\alpha_0|^2})]$ and α_0 is real. The probability of outcomes $x_{\theta A}$ for $\hat{x}_{\theta,A}$ and $\hat{x}_{\phi B}$ for $\hat{x}_{\phi,B}$ is given as $P(x_{\theta A}, x_{\phi B}) = |\langle x_{\theta A} | \langle x_{\phi B} | \psi_B \rangle|^2$ where $|x_{\theta A}\rangle$ and $|x_{\phi B}\rangle$ are eigenstates of $\hat{x}_{\theta A}$ and $\hat{x}_{\phi B}$. The state $|\psi_B\rangle$ may be compared with the mixed state

$$\rho_{\text{non-ent}} = \frac{1}{2} \{\rho_+ + \rho_-\} \quad (8.4)$$

where $\rho_{\pm} = |\pm\alpha_0\rangle_A |\pm\alpha_0\rangle_B \langle \pm\alpha_0|_B \langle \pm\alpha_0|_A$ which is separable (non-entangled) and for which there is no violation of the Bell inequality.

A. CV Bell simulation

We next outline the simulation of the CV Bell violations. The Q function $Q(\alpha, \beta) = \frac{1}{\pi^2} |\langle \alpha | \langle \beta | \psi_B \rangle|^2$ for the state $|\psi_B\rangle$ is expressed in terms of the real variables $\lambda = (x_A, p_A, x_B, p_B)$ as ($r_0 = \kappa t_I$)

$$\begin{aligned}
Q(\alpha, \beta) = & \frac{N_0^2 e^{-p_A^2/4 - p_B^2/4 - \tanh r_0 p_A p_B/2}}{16\pi^2 \cosh^2 r_0} \left\{ e^{-(x_A - 2\alpha_0 e^{r_0})^2/4} e^{-(x_B - 2\alpha_0 e^{r_0})^2/4} \times e^{2(\tanh r_0)[(x_A - 2\alpha_0 e^r)(x_B - 2\alpha_0 e^{r_0})/4]} \right. \\
& + e^{-(x_A + 2\alpha_0 e^{r_0})^2/4} e^{-(x_B + 2\alpha_0 e^{r_0})^2/4} \times e^{2(\tanh r_0)[(x_A + 2\alpha_0 e^{r_0})(x_B + 2\alpha_0 e^{r_0})/4]} \\
& \left. + 2e^{-2(1 - \tanh r_0)\alpha_0^2 e^{2r_0}} e^{-x_A^2/4} e^{-x_B^2/4} e^{\frac{1}{2}(\tanh r_0)[(x_A x_B)]} \cos[(1 - \tanh r_0)\alpha_0 e^{r_0}(p_A + p_B)] \right\} \quad (8.5)
\end{aligned}$$

This function has the form

$$Q(\lambda, t_0) \sim G(p_A, p_B) \{G_1(x_A, x_B) + G_2(x_A, x_B) + \mathcal{I}\}$$

where G is a bivariate Gaussian function and \mathcal{I} is a sinusoidal interference term arising due to the entanglement. The Q function for the non-entangled state $\rho_{non-ent}$ (Eq. (8.4)) comprises the first two Gaussian terms, with $\mathcal{I} = 0$. The interference term is required for the Bell violation.

Measurement settings: For the measurements under consideration here, the device that determines the measurement settings θ and ϕ is a phase-shifter, which can be modelled by the interaction Hamiltonians

$$H_\theta = g\hat{n}_A, \quad H_\phi = g\hat{n}_B \quad (8.6)$$

for systems A and B respectively ($g > 0$). Here, \hat{n}_A and \hat{n}_B are the number operators for the field modes A and B . Straightforward solutions for the operator equations of motion yield for H_θ that $\hat{x}_A = g\hat{p}_A/\hbar$ and $\hat{p}_A = -g\hat{x}_A/\hbar$, and similarly for H_ϕ , leading to

$$\begin{aligned}
\hat{x}_A(t) &= \hat{x}_A(0) \cos \theta + \hat{p}_A(0) \sin \theta \\
\hat{x}_B(t) &= \hat{x}_B(0) \cos \phi + \hat{p}_B(0) \sin \phi \quad (8.7)
\end{aligned}$$

where $\theta = gt_A/\hbar$ and $\phi = gt_B/\hbar$, the t_A and t_B being the times of interaction. This gives the required transformations (8.1) and (8.2). The interactions H_θ and H_ϕ correspond to the unitary operations $U_A(\theta) = e^{-iH_\theta t_A/\hbar} = e^{-i\theta\hat{n}_A}$ and $U_B(\phi) = e^{-iH_\phi t_B/\hbar} = e^{-i\phi\hat{n}_B}$.

After interaction with the phase-shifters, to adjust the settings, the state of the system is

$$|\psi_B(t_1)\rangle = e^{-iH_\theta t_A/\hbar} e^{-iH_\phi t_B/\hbar} |\psi\rangle_{AB} \quad (8.8)$$

The corresponding Q function at time t_1 is

$$\begin{aligned}
Q(\lambda_{rot}, t_1) &= \frac{1}{\pi^2} |\langle \alpha | \langle \beta | e^{-i\theta\hat{n}_A} e^{-i\phi\hat{n}_B} |\psi_B\rangle|^2 \\
&= \frac{1}{\pi^2} |\langle \alpha e^{i\theta} | \langle \beta e^{i\phi} | \psi_B\rangle|^2 \quad (8.9)
\end{aligned}$$

where $\lambda_{rot} = (x_{\theta A}, p_{\theta A}, x_{\phi B}, p_{\phi B})$. The last line follows since $e^{i\theta\hat{n}}|\alpha\rangle = |\alpha e^{i\theta}\rangle$. It is shown in the Appendix C that the Q function $Q(\lambda_{rot}, t_1)$ of the new state at time t_1 corresponds to rotating the coordinates x_A, p_A, x_B, p_B in the original Q function to new coordinates $x_{\theta A}, p_{\theta A}, x_{\phi B}, p_{\phi B}$, defined as

$$\begin{aligned}
x_{\theta A} &= x_A \cos \theta + p_A \sin \theta \\
p_{\theta A} &= -x_A \sin \theta + p_A \cos \theta \quad (8.10)
\end{aligned}$$

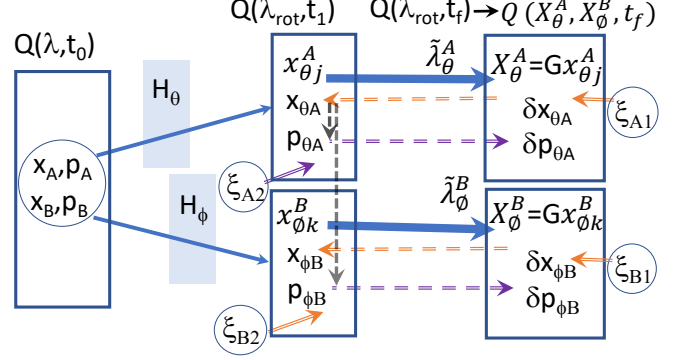


Figure 23. Depiction of the steps in the simulation of the measurement of the CV Bell nonlocality. The system is prepared for measurements \hat{x}_A and \hat{x}_B , at time t_0 . The state is given by $Q(\lambda, t_0)$. There can be a change of measurement setting at each location as given by θ and ϕ , so that the system at time t_1 is prepared for measurements $\hat{x}_{\theta A}$ and $\hat{x}_{\phi B}$. The settings are changed according to H_θ and H_ϕ , which give a causal deterministic relation (thin blue arrows). The system at time t_1 is given by $Q(\lambda_{rot}, t_1)$. After settings are fixed, the measurements $\hat{x}_{\theta A}$ and $\hat{x}_{\phi B}$ are carried out by an amplification, according to H_{amp}^A and H_{amp}^B , giving stochastic forward-backward dynamics which can lead to loops. The solid blue lines denote the causal relations in which the means $x_{\theta j}^A$ and $x_{\phi k}^B$ of the Gaussians in the function $Q(\lambda_{rot}, t_1)$ are amplified to $Gx_{\theta j}^A$ and $Gx_{\phi k}^B$. Any correlation between $x_{\theta j}^A$ and $x_{\phi k}^B$ as described by $Q(\lambda_{rot}, t_1)$ is therefore present in the future boundary condition at t_f (depicted by thick blue lines). The noise inputs at the boundary imply retrocausal trajectories $x_{\theta A}(t) = x_{\theta j}^A + \delta x_{\theta A}$ and $x_{\phi B}(t) = x_{\phi k}^B + \delta x_{\phi B}$ (orange dashed lines). The $Q(\lambda_{rot}, t_1)$ determines the correlations between trajectories, but since the settings give a deterministic relation, the correlations are equivalently determined by $Q(\lambda, t_0)$. Hence, diagram does not imply a direct nonlocal influence at time t_1 . The causal structure is depicted in Figs. 25-28. The correlation between x and p is depicted by the black vertical lines, which is absent for the EPR state $|\psi_{epr}\rangle$.

and coordinates

$$\begin{aligned}
x_{\phi B} &= x_B \cos \phi + p_B \sin \phi \\
p_{\phi B} &= -x_B \sin \phi + p_B \cos \phi \quad (8.11)
\end{aligned}$$

consistent with (8.1) and (8.2). Hence, the adjustment of measurement settings is carried out in the simulation by changing the Q function $Q(\lambda, t_0)$ to obtain a new Q function $Q(\lambda_{rot}, t_1)$ where $\lambda_{rot} = (x_{\theta A}, p_{\theta A}, x_{\phi B}, p_{\phi B})$. These transformations corresponding to the change of setting are hence *local and deterministic*. They give a *causal relation*, from time t_0 to t_1 . This is depicted by the thin blue

arrows. Being deterministic however, there is a two-way relation, since the values of at t_1 imply the values at t_0 with a one-to-one correspondence. The transformations (8.10) and (8.11) to rotated coordinates is equivalent to the change of measurement bases in the qubit Bell state (refer Appendix D).

Comparing with the non-entangled mixed state $\rho_{non-ent}$ of Eq. (8.4), the Q function at time t_0 for $|\psi_B\rangle$ differs only by the term \mathcal{I} . After the change of bases, the integration over the p coordinates leads to a change in the coefficients appearing before the Gaussian terms in x , which explains the change in the joint probabilities after the rotations. As with the example for the Bell state (??), the joint probabilities can be different, after *both* rotations ϕ and θ , because of the term \mathcal{I} . While this term does not contribute to the measured probabilities when $\theta = \phi = 0$, the integration over p of the cosine term in \mathcal{I} leads to a contribution in the marginal function $Q(x_{\theta A}, x_{\phi B}, t_f)$ that is not present for $\rho_{non-ent}$.

Amplification: After the settings are fixed, at a time t_1 , the measurement of \hat{x}_θ and \hat{x}_ϕ proceeds by amplifying $x_{\theta A}$ and $x_{\phi B}$ according to H_{amp} and H_{amp} , followed by a final detection. The transformations for the measured amplitudes are *stochastic and retrocausal*, given by

$$\begin{aligned} \frac{dx_{\theta A}}{dt_-} &= -gx_{\theta A} + \xi_{A1}(t) \\ \frac{dx_{\phi B}}{dt_-} &= -gx_{\phi B} + \xi_{B1}(t) \end{aligned} \quad (8.12)$$

with a boundary condition in the future, where $t_- = -t$. Those for p are

$$\begin{aligned} \frac{dp_{\theta A}}{dt} &= -gp_{\theta A} + \xi_{A2}(t) \\ \frac{dp_{\phi B}}{dt} &= -gp_{\phi B} + \xi_{B2}(t) \end{aligned} \quad (8.13)$$

with a boundary condition in the past. The Gaussian random noises $\xi_{A\mu}(t)$ and $\xi_{B\mu}(t)$ satisfy: $\langle \xi_{A\mu}(t) \xi_{A\nu}(t') \rangle = 2g\delta_{\mu\nu}\delta(t-t')$ and $\langle \xi_{B\mu}(t) \xi_{B\nu}(t') \rangle = 2g\delta_{\mu\nu}\delta(t-t')$, with cross terms zero. The boundary conditions are determined by the Q function $Q(\lambda_{rot}, t_1)$ in the rotated coordinates. As in the earlier simulations, the future boundary condition is determined by the Q function of the amplified state at time t_f . Using **Result 2** of Sec. IV.D for Born's rule, the density of the final amplified amplitudes is the probability of detection $P(x_{\theta A}, x_{\phi B})$ i.e. $Q(x_{\theta A}, x_{\phi B}, t_f) \rightarrow P(x_{\theta A}, x_{\phi B})$, giving a violation of the Bell inequality for certain choices of θ and ϕ [137].

IX. CAUSAL STRUCTURE OF THE EPR AND BELL SIMULATIONS

In the model based on the simulations of EPR and Bell nonlocality, the x_A, x_B, p_A, p_B are the hidden variables. The simulation can be examined to identify a

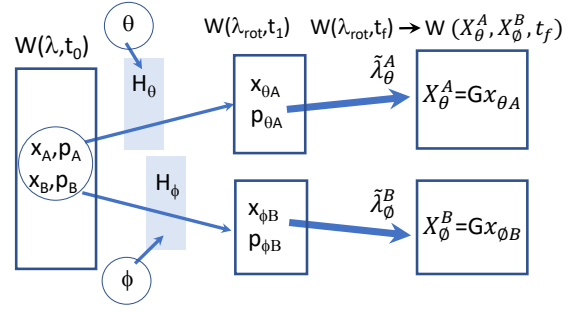


Figure 24. Depiction of the simulation of the measurement of the CV EPR entanglement based on the Wigner function. At time t_0 , hidden variables can be identified that correspond to the outcomes of measurement of \hat{x}_A and \hat{x}_B . The function $W(x_A, p_A, x_B, p_B)$ is a distribution, giving the probability the system is in a hidden variable state $\lambda = (x_A, p_A, x_B, p_B)$.

causal (cause-and-effect) structure consistent with Bell nonlocality.

A. EPR entanglement and the Wigner function

In the EPR experiment, the outcome of the measurement of \hat{x}_B is known from that of \hat{x}_A . Similarly, the outcome of the measurement of \hat{p}_B is known from that of \hat{p}_A . EPR argued that since the systems A and B can be spatially separated, and assuming the measurement at A cannot affect the system B , then both outcomes (of \hat{x}_B and \hat{p}_B) must be predetermined. This led EPR to conclude that quantum mechanics is incomplete [101].

The state $|\psi_{epr}\rangle$ possesses a positive Wigner function $W(x_A, p_A, x_B, p_B)$, which provides a local hidden variable theory that does indeed give simultaneous predetermined values for both \hat{x}_B and \hat{p}_B . The causal structure of a simulation of the EPR correlations based on the Wigner function is given in Fig. 24. However, the Wigner function is negative for Bell states, for which there is no local hidden variable theory explaining all measurements [1].

The Wigner function for the EPR system is not the same as the Q function. The Q function is positive for all quantum states of the field. The causal structure of the simulations based on the Q function is presented in Figs. 25-28 and differs from that of the Wigner distribution, involving retrocausality. The question is: how do the values for x_A and x_B (or p_A and p_B) become correlated if not through the scheme of Fig. 24?

B. Causal structure for EPR and Bell nonlocality

At an initial time t_0 , we assume the systems have been prepared for measurements of \hat{x}_A and \hat{x}_B . The probability distribution for the x_A, x_B, p_A, p_B is given by the Q function $Q(x_A, x_B, p_A, p_B)$. The systems A and B are spatially separated. The first stage of the measure-

ment are the local interactions H_θ and H_ϕ that determine the settings θ and ϕ , which results in the transformed state at the time t_1 : This corresponds to the *local causal deterministic* transformations of the amplitudes x_A, x_B, p_A, p_B to give $x_{\theta A}, p_{\theta A}, x_{\phi B}, p_{\phi B}$, according to (8.10) and (8.11). The amplification that completes the measurement requires the *retrocausal stochastic relations* for variables $x_{\theta A}, p_{\theta A}, x_{\phi B}, p_{\phi B}$ as in (8.12) and (8.13), which separate into a forward and backward propagation (depicted by the orange dashed arrows).

The Bell violation involves three set-ups for joint measurements at A and B : (1) no setting change $\theta = \phi = 0$; (2) a change of setting at one site only; (3) change of setting at both sites. We examine each separately.

1. Measurement of \hat{x}_A and \hat{x}_B

We consider joint measurement of \hat{x}_A and \hat{x}_B (Fig. 25), where $\theta = \phi = 0$. The simulation is consistent with the model explained in Figs. 1 and 7 where, as the system amplifies, the values for the outcomes (if detection takes place) are given by $x_A(t)$ and $x_B(t)$. We denote the predetermined values as $\tilde{\lambda}_x^A$ and $\tilde{\lambda}_x^B$.

The correlation between the outcomes $\tilde{\lambda}_x^A$ and $\tilde{\lambda}_x^B$ for \hat{x}_A and \hat{x}_B is determined by the Q function $Q(\lambda, t_0)$, as written with respect to coordinates x_A, p_A, x_B and p_B . The means x_j^A and x_k^B of the Gaussian functions in $Q(\lambda, t_0)$ are amplified to Gx_j^A and Gx_k^B , and the correlation between them is hence determined by $Q(\lambda, t_0)$. This is because the interference terms \mathcal{I} in $Q(\lambda, t_0)$ are not amplified by H_{amp}^A and H_{amp}^B . Hence, the prediction for joint probabilities of outcomes \hat{x}_A and \hat{x}_B is the same as for the mixed state, $\rho_{non-ent}$ (Eq. (8.4)). The joint probability for outcomes of \hat{x}_A and \hat{x}_B is given by $Q(x_A, x_B, t_{m1})$, which gives the density of amplitudes at time t_{m1} . This result is consistent with the predictions of quantum mechanics and has been generalised [116, 117]. For completeness, we summarise with the following Result given in Refs. [116, 117].

Result 6a: Weak local realism: Suppose at a time t_m , the system is prepared for the measurement of $\hat{x}_{\theta A}$ and $\hat{x}_{\phi B}$, meaning that the system has interacting with a measurement-setting device (e.g. a polariser beam splitter, Stern-Gerlach analyzer, or phase-shifter), so that an amplification followed by detection completes the measurement. Then the joint probabilities for outcomes $x_{\theta A}$ and $x_{\phi B}$ are identical to those of a non-entangled state and are consistent with a hidden variable model in which there is a predetermination of the outcomes.

Proof: The state in the measurement basis is written $|\psi_B\rangle = \sum_{IJ} c_{IJ} |I\rangle_\theta |J\rangle_\phi$ where the c_{IJ} are probability amplitudes, and the $|I\rangle_\theta$ and $|J\rangle_\phi$ are states with definite outcomes for $\hat{x}_{\theta A}$ and $\hat{x}_{\phi B}$ of system A and B respectively. The joint probabilities for the outcomes $x_{\theta A}$ and $x_{\phi B}$ are identical to those of the mixed state $\rho_{mix,\theta,\phi} = \sum_{IJ} |c_{IJ}|^2 \rho_{IJ}$, where $\rho_{IJ} = |I\rangle_\theta |J\rangle_\phi \langle J|_\phi \langle I|_\theta$,

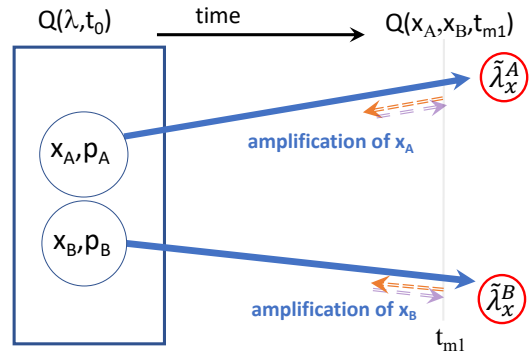


Figure 25. Depiction of the simulation where \hat{x}_A and \hat{x}_B are measured by amplification. The settings have been fixed (at $\theta = 0$ and $\phi = 0$), the system being prepared with respect to the basis \hat{x}_A and \hat{x}_B at time t_0 . The solid blue lines denote the causal relation in which the means x_j^A and x_k^B of the Gaussians in $Q(\lambda, t_0)$ are amplified to Gx_j and Gx_k . After sufficient amplification, at time t_{m1} , there is consistency with the model where the values $x_A(t)$ and $x_B(t)$ determine the outcomes of \hat{x}_A and \hat{x}_B . We identify the predetermined values by $\tilde{\lambda}_x^A$ and $\tilde{\lambda}_x^B$. The marginal $Q(x_A, x_B, t_{m1})$ gives the probability density of amplitudes at time t_{m1} after amplification. Any correlation between the outcomes \hat{x}_A and \hat{x}_B (given by $\tilde{\lambda}_x^A$ and $\tilde{\lambda}_x^B$) is determined by $Q(\lambda, t_0)$, written in the x_A, x_B coordinates. The interference terms \mathcal{I} do not amplify, and the joint probabilities are identical to those of the non-entangled state $\rho_{non-ent}$ of Eq. (8.4).

for which the outcomes I and J are predetermined and occur with probability $|c_{IJ}|^2$. \square

2. Changing the setting at one location: no-signalling

Next, we consider where the setting is changed *at one location*, say at B , but with the setting at A fixed (Fig. 26). Fig. 25 shows the measurement of x_A and x_B , where the system has been prepared at time t_0 in the measurement basis $\theta = \phi = 0$, and we define the predetermined values as $\tilde{\lambda}_x^A$ and $\tilde{\lambda}_x^B$. So, we change the setting at one site, B . The H_{amp} is reversible, and we may de-amplify and change the setting at B . This corresponds to a local rotation of coordinates, as in (8.11). The future boundary condition then changes, but the setting at A is fixed. This leads to the following result which completes the earlier **Result 4a**, of Sec. IV.E.

Result 4b: No-signalling: The simulations modelling the Bell-nonlocal measurements are consistent with no-signalling: Once the measurement setting and value $\tilde{\lambda}_x^A$ for the outcome is determined, after sufficient amplification, the value $\tilde{\lambda}_x^A$ for the outcome is not changed by interactions or dynamics that may then occur at B .

Proof: The transformation (8.11) is local, rotating only the amplitudes x_B and p_B . The future boundary condition changes due to the change of setting at B , but the setting at A is fixed, so the simulation is consistent with

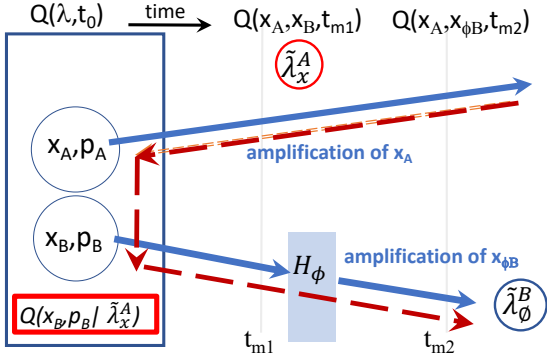


Figure 26. Depiction where there is a change of setting at B to ϕ , while the setting at A is fixed at $\theta = 0$. There is a local rotation of coordinates by a device H_ϕ , according to (8.11) at B . The new Q function $Q(x_A, x_{\phi B}, t_{m2})$ gives the probability density of amplitudes for the system at time t_{m2} . The simulation is consistent with the model that the value for $\tilde{\lambda}_x^A$ giving the outcome of \hat{x}_A is unchanged, which implies *no-signalling*. However, the retrocausal trajectories $x_A(t)$ will correlate (connect) with certain trajectories for system B at the original time t_0 , as consistent with $Q(\lambda, t_0)$. This means that the outcome $\tilde{\lambda}_x^A$ of A gives feedback (red dashed line) which ensures the quantum state given by $Q(x_B, p_B | \tilde{\lambda}_x^A)$ for system B , at time t_{m1} .

the outcome $\tilde{\lambda}_x^A$ of A being unchanged. That the value $\tilde{\lambda}_x^A$, which gives the outcome for \hat{x}_A (as in **Result 3**), is unchanged by the change of setting to ϕ at B is consistent with the observation of *no-signalling*. \square

This result is consistent with the predictions of quantum mechanics and can be generalised [116, 117]. For completeness, we summarise with the following Result given in Refs. [116, 117], completing Result 6a.

Result 6b: Weak local realism: The system is prepared as in **Result 6a**. If there is after time t_m a change of setting at *one site only*, say from ϕ to ϕ' at B , then the probabilities for the joint outcomes of \hat{x}_θ and $\hat{x}_{\phi'}$ are indistinguishable from those of a local hidden variables theory, in which there is a fixed predetermined value for the outcome of system A .

Proof: The probabilities for the outcomes are indistinguishable from those of the non-entangled mixed state $\rho_{mix, \theta, \phi'}$ obtained from a local transformation on $\rho_{mix, \theta, \phi}$ (defined in Result 6a) and can be modelled by a local hidden variables theory. The proof is given in Appendix D for qubit Bell states and in Ref. [116]. \square

However, more can be learned by examining the simulation. If there is a change of setting at B , then there are constraints imposed. The outcomes at B must be correlated with A in the fashion determined by the joint distribution $Q(\lambda_{rot}, t_{m1})$ (where $\theta = 0$), which imposes the future boundary condition in the simulation. Equivalently, we can consider the *retrocausal trajectories that trace back to the initial state* at time t_0 , as in the Sec. V for the superposition states. This gives a feedback (red dashed lines) to restrict the state of system B , as

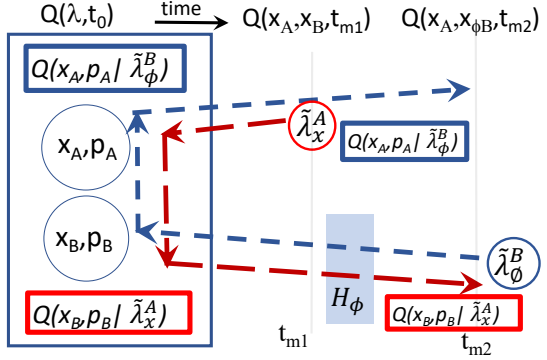
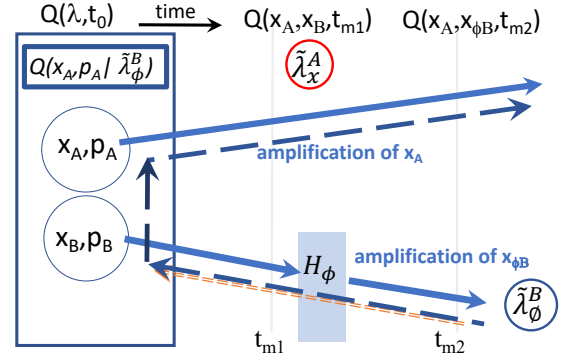


Figure 27. Depiction of the simulation of Bell nonlocality, when there is a change of setting at B to ϕ , while the setting at A is fixed at $\theta = 0$. At the time t_{m2} , after amplification at B , the value $\tilde{\lambda}_\phi^B$ determines the outcome for \hat{x}_ϕ^B . The retrocausal amplitudes at B conditioned on the value $\tilde{\lambda}_\phi^B$ must correlate with certain amplitudes for A at the origin, as determined by $Q(\lambda, t_0)$, and also be consistent with the future boundary condition. There is a feedback from B to A (blue dashed arrows) which ensures the state at A is given as $Q(x_A, p_A | \tilde{\lambda}_\phi^B)$ (top figure). The mutual feedback (lower figure) is consistent with the density of amplitudes at t_{m2} , as given by the Q function $Q(x_A, x_{\phi B}, t_{m2})$.

depicted in Fig. 26. The retrocausal trajectories propagating backwards, conditioned on the outcome $\tilde{\lambda}_x^A$ at A , impose, due to the correlations implied by the Q function $Q(\lambda, t_0)$, a constraint on the outcomes at B , according to

$$Q(\lambda, t_0 | \tilde{\lambda}_x^A) \equiv Q(p_A, x_B, p_B, t_0 | \tilde{\lambda}_x^A)$$

We also refer to this distribution $Q(p_A, x_B, p_B, t_0 | \tilde{\lambda}_x^A)$ as $Q_{loop}(p_A, x_B, p_B, t_0 | \tilde{\lambda}_x^A)$ (to remind us of the feedback). The conditioned state

$$Q(x_B, p_B | \tilde{\lambda}_x^A) \quad (9.1)$$

found on integrating over p_A hence *constrains the outcomes for B* (in relation to that of A) for any future measurement settings, including the particular choice ϕ . This gives the following Result:

Result 7: Weak elements of reality: Suppose the measurement setting at A has been fixed and the system

A amplified, so that outcome $\tilde{\lambda}_x^A$ at A is specified (**Result 3**). The constraints $Q(x_B, p_B | \tilde{\lambda}_x^A)$ on the outcomes for B are in place at (or by) the time t_{m1} , when the outcome $\tilde{\lambda}_x^A$ at A is specified (provided the setting at A remains fixed). The $Q(x_B, p_B | \tilde{\lambda}_x^A)$ implies predictions for B, for any given setting change ϕ at B that might take place. These predictions are in place, regardless of whether the unitary operations U_B that determine the settings at B have actually occurred. \square An evaluation of $Q(x_B, p_B | \tilde{\lambda}_x^A)$ for an entangled system is given in Appendix E.

However, we note that the reverse also holds: there is feedback to A from B (blue dashed line in Fig. 27). After amplification at B, at time t_{m2} , there is a value $\tilde{\lambda}_\phi^B$ for the outcome of measurement $\hat{x}_{\phi B}$. The state at A conditioned on B is determined by the initial Q function

$$Q(\lambda, t_0 | \tilde{\lambda}_\phi^B) \equiv Q(p_B, x_A, p_A, t_0 | \tilde{\lambda}_\phi^B)$$

Integrating over p_B , the state at A is

$$Q(x_A, p_A | \tilde{\lambda}_\phi^B)$$

This leads to the Result 7 as applied to system A: Both $Q(x_A, p_A | \tilde{\lambda}_\phi^B)$ and $Q(x_B, p_B | \tilde{\lambda}_x^A)$ are consistent with the future boundary condition, which is determined by $Q(\lambda, t_1)$, the state defined after the settings are fixed, at $\theta = 0$ and ϕ . Figure 27 (lower) depicts the mutual consistency for the conditioned states.

The question is: does the change of setting at B influence the system or outcome at A i.e. is there a nonlocal effect at A? In the simulation model, there is *no change to the outcome* $\tilde{\lambda}_x^A$ at A due to the change of setting ϕ at B, once the setting at A is fixed.

However, if we examine the Q function (8.5), we see that the change of setting at B imposes a *change* $\Delta\mathcal{I}(\phi)$ to the *hidden terms* in the Q function that represents the state of the system. There is a rotation of coordinates x_B and p_B , according to $Q(\lambda_{rot}, t_{m1})$, from the original $Q(\lambda, t_0)$, that can change the interference terms \mathcal{I} , when the function is written in terms of the new basis. However, similar to a change of basis at one site in a standard Bell state (refer Appendix D), the result for joint probabilities $P(x_A, x_{\phi B})$ is identical to that of the non-entangled state $\rho_{non-ent}$ for which $\mathcal{I} = 0$. There is no nonlocal effect observed in the immediate joint probabilities, $P(x_A, x_{\phi B})$.

3. Changing the setting at both locations: EPR and Bell nonlocality

However, the change $\Delta\mathcal{I}(\phi)$ to the state $Q(\lambda_{rot}, t_0)$ due to the change of setting ϕ at B can manifest as Bell nonlocality *when there is a further change of setting* θ , at A. Bell nonlocality arises because the change of setting θ at A induces a further change in the interference term \mathcal{I} , which can depend on the value ϕ . A careful study of the evaluation of the marginal for $x_{\theta A}$ shows there is

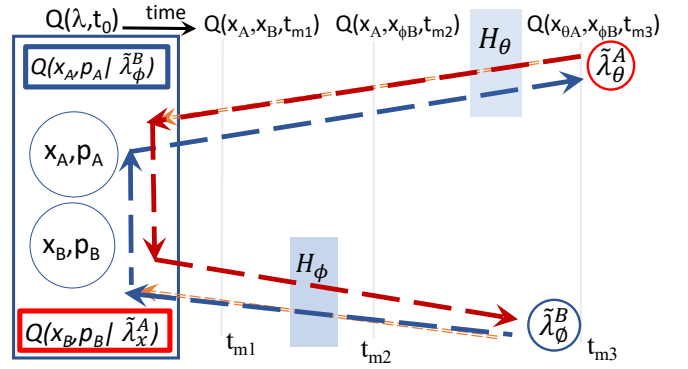


Figure 28. Depiction of the measurement of Bell nonlocality, when there is a change of setting at B to ϕ , and then a change of setting θ at A. The change of setting ϕ at B induces a change to the state, as given by the Q function $Q(x_A, x_{\phi B}, t_{m2})$ which is different to $Q(x_A, x_B, t_{m1})$. The function for the entangled state is different to that of the non-entangled state $\rho_{non-ent}$. This change manifests when there is a change of setting θ at A, when Bell nonlocality can arise. There is a difference in the joint probabilities $Q(x_{\theta A}, x_{\phi B}, t_{m3})$, which can violate a Bell inequality.

a conversion of interference terms into terms which determine the *observable* probabilities under amplification H_{amp} . In other words, the joint probability $P(x_{\theta A}, x_{\phi B})$ can change relative to that for the non-entangled state $\rho_{non-ent}$ (Fig. 28).

We have considered that the setting of A is changed to θ , *after* that of B, but the time order is immaterial for the final observed correlations. In the model, with the settings at B fixed, the value $\tilde{\lambda}_\phi^B$ for outcome at B is not changed by the change of setting θ at A. The state at A is fixed by (blue dashed lines in Fig. 28)

$$Q(x_A, p_A | \tilde{\lambda}_\phi^B)$$

This means that the correlations for A with B are determined by the outcome $\tilde{\lambda}_\phi^B$ at B. The microscopic feedback to the state of the system due to the change of setting at B can induce Bell nonlocality if there is a further change of setting at A. We summarise with the following result:

Result 8: Bell nonlocality can emerge when there is a change of measurement setting ϕ and θ , at both locations A and B respectively. The proof is given by demonstration above. \square

Other strict tests of quantum correlations exist (e.g. [39, 96, 97, 112, 139–143]), some of which have similarly been shown consistent with the premises of weak local realism (as defined in Results 6 and 7), and which require a change of measurement setting at two locations [49, 97, 117, 144].

X. CONCLUSIONS

The simulations given in this paper for CV EPR and Bell entanglement allow Bell nonlocality while giving a model of quantum measurement that is consistent with no-signalling and macroscopic realism. We see from the **Results 1-8** that the simulations are consistent with a model of reality in which the following three premises hold. Following previous work, we refer to this model as *weak macroscopic realism* (wMR) [116]. The model involves a partial relaxation of EPR's and Bell's local realistic premises so that "elements of reality" exist for the systems after the measurement settings have been determined.

Premise (1) The first premise is macroscopic realism: **Result 3** established in Sec. IV.E implies *macroscopic realism*: We suppose that the measurement setting for a system A has been fixed, so that an observable \hat{O} is to be measured. The measurement procedure involves amplification. After sufficient amplification, at a time t_m , the system may be considered to be in a superposition of macroscopically distinct states that have a definite outcome for $\hat{O} \equiv \hat{x}$. As an example, the system initially in a superposition $|\psi\rangle = \sum_{c_i} c_i |x_i\rangle$ of eigenstates of \hat{x} evolves, after amplification of \hat{x} , into the superposition

$$e^{-iH_{amp}t/\hbar}|\psi_{sup}\rangle = \sum_{c_i} e^{-iH_{amp}t/\hbar}|x_i\rangle = \sum_{c_i} |Gx_i\rangle$$

of macroscopically distinct states $|Gx_i\rangle$, where here $G = e^{gt}$ is the amplification factor. Figure 1 illustrates this realization. The premise of *wMR* asserts that the system at the time t_m satisfies macroscopic realism: There is a predetermined value for the outcome of \hat{O} . In the depictions of the simulations, the predetermined value has been denoted by $\tilde{\lambda}_x^A$. The terminology "weak" is introduced in order to distinguish from other stricter definitions of macroscopic realism, which may not assume that the measurement setting has been fixed, and which can be negated.

Premise (2) The second premise is a weak type of locality, established by **Result 4a** and **Result 4b** in Secs. IV.E and IX.B. The premise posits that the value $\tilde{\lambda}_x^A$ for the outcome of system A at time t_m (after the setting at A has been fixed) cannot be changed by a subsequent change of setting at another spacelike-separated system B (consistent with no-signaling). Here, we assume all devices are at rest in a common frame of reference. The model is *macroscopically causal*, since the outcome of the measurement \hat{x} for the system in a macroscopic superposition state is specified (to be $\tilde{\lambda}_x^A$) at time t_m . The causal relation is that this value $\tilde{\lambda}_x^A$ determines the measurement outcome at the later time t_f .

Premise (3) The third premise concerns "elements of reality". The premise is based on **Result 7** established in Sec. IX.B. According to the model, the predicted correlated outcomes for B , given an outcome $\tilde{\lambda}_\theta$ of A , are fixed once the value $\tilde{\lambda}_\theta$ for A is fixed i.e. at the time

t_{mA} , after the setting θ at B is fixed and after sufficient amplification at A . This addresses a common question about the EPR experiment, where the value for \hat{p}_B can be inferred from that of \hat{p}_A of system A : According to the premise, the value for \hat{p}_B is fixed at the time t_{mA} .

Breakdown of Bell's assumptions: The above premises are not conflicted with Bell nonlocality [113, 116, 117]. The question is why does the Bell local-hidden-variable model break down, in terms of the simulations? Bell's local hidden variable condition is

$$P(++|\theta, \phi) = \int d\lambda \rho(\lambda) P_A(+|\lambda, \theta) P_B(+|\lambda, \phi) \quad (10.1)$$

where $P(++|\theta, \phi)$ is the probability of obtaining $+1$ at both sites with settings θ and ϕ ; $\rho(\lambda)$ is the distribution for hidden variables λ , and $P_A(+|\lambda, \theta)$ ($P_B(+|\lambda, \phi)$) is the probability for $+1$ at A (B), given λ and θ (ϕ). The assumption implies Bell's inequality.

In the simulations, the hidden variables λ are the coordinates x_A, p_A, x_B and p_B of the Q function. The interactions H_θ and H_ϕ that determine the measurement settings at A and B respectively are local. The amplitudes x_θ^A, x_ϕ^B of the simulation if directly measurable would lead to moments satisfying Bell's condition, with $\rho(\lambda) \equiv Q(\boldsymbol{\lambda}, t_0)$ where $\lambda = (x_A, p_A, x_B, p_B)$. However, this is not the case, because parts of the amplitudes are "hidden", being associated with noise inputs at the future boundary.

The Bell violations require changes of settings θ and ϕ at both sites, so that the Bell state is considered with respect to rotations to two different bases, one for each system A and B . Over both unitary rotations, we have seen (**Result 7**) that *unobservable hidden terms* [e.g. \mathcal{I} in $Q(\boldsymbol{\lambda}, t_0)$] contribute to probabilities for observable outcomes in the final $Q(\boldsymbol{\lambda}_{rot}, t_1)$ i.e. over the two changes of settings, the Bell condition breaks down:

$$P(++|\theta, \phi) \neq \int d\lambda Q(\boldsymbol{\lambda}, t_0) P_A(+|\boldsymbol{\lambda}, \theta) P_B(+|\boldsymbol{\lambda}, \phi) \quad (10.2)$$

It is possible to check the condition (10.1), by evaluating in the simulation $P(++|\lambda, \theta, \phi)$, $P_A(+|\lambda, \theta)$ and $P_B(+|\lambda, \phi)$. We have seen that for a given θ and ϕ , and for outcomes $+$ at A and B , it is possible to trace *back* the trajectories and evaluate $P(x_{\theta A}, x_{\phi B} | ++)$. It is also possible to evaluate $P(++)$, the probability of outcome $+1$ at both sites for the given θ and ϕ , and hence also the joint distribution $P(x_{\theta A}, x_{\phi B}, ++) = P(x_{\theta A}, x_{\phi B} | ++)P(++)$. Hence, we can evaluate

$$\begin{aligned} P(+, + | x_{\theta A}, x_{\phi B}) &= P(x_{\theta A}, x_{\phi B}, ++) P(x_{\theta A}, x_{\phi B}) \\ &= P(x_{\theta A}, x_{\phi B} | ++) P(++) P(x_{\theta A}, x_{\phi B}) \end{aligned} \quad (10.3)$$

Using the deterministic relation between $x_{\theta A}, x_{\phi B}$ and x_A, x_B, p_A and p_B , the $P(++|\lambda, \theta, \phi)$ can be evaluated.

Experiments: Finally, we consider experimental tests that could be performed. The interaction H_{amp} of

Eq. (2.3) is that of parametric amplification [118], which has been experimentally realized [124, 125]. The states studied in this paper are superpositions of squeezed or coherent states ('cat states') which have also been realised experimentally [110, 121, 130, 145–150]. Hence, the measurement model can be illustrated experimentally.

The prediction of causal consistency can be tested experimentally, as depicted in Fig. 3. The simulation depends on the initial and final Q functions which are measurable by tomography [151]. It is feasible to perform a simulation that matches boundary conditions given by the experimental Q functions. It is also feasible to measure the Q function at any intermediate time t . The prediction of causal consistency (that the density of amplitudes $x(t)$ and $p(t)$ in the simulation match the distribution given by the evolved Q function $Q(x, p, t)$), can be tested. The consistency is demonstrated, by showing that the choice of time t_f of the future boundary does not affect the densities and resulting distributions.

A second experiment is to signify a ‘‘hidden loop’’ and to illustrate the cat paradox (Figs. 2 and 4). A ‘‘hidden loop’’ involves amplitudes that are not amplified (and hence not observed) in the measurement model, and a distribution Q_{loop} that cannot be described by a quantum wavefunction. The Q_{loop} for an individual branch of the superposition can be constructed from the simulation that is based on the experimental Q functions. If Q_{loop} shows a reduction of variances below the Heisenberg uncertainty bound, then, within the constraints of the model, this contributes a signature of a hidden loop.

The simulations give an explanation of the EPR paradox, in terms of the ‘‘weak elements of reality’’ that exist in the model after the measurement settings are fixed, and after sufficient amplification (Premise 1 above) [122]. These weak elements of reality do not conflict with Bell's theorem [116]. The simulations can be used to analyze questions raised by Schrodinger about the EPR argument, as in the recent experiment of Colciaghi et al which reported EPR correlations for Bose-Einstein condensates [103].

ACKNOWLEDGMENTS

We acknowledge support from the Templeton Foundation under Project Grant ID 62843. This research has been supported by the Australian Research Council Grants schemes under Grants DP180102470 and DP190101480. The authors thank NTT Research for their financial and technical support.

APPENDIX A: STOCHASTIC PATH INTEGRAL THEOREMS

A. Definitions and notation

We make use of methods that were first used for diffusive path integrals [152, 153], here generalized to forward-backward trajectories. For M bosonic modes, the phase-space vector $\boldsymbol{\lambda}$ is a $2M$ -dimensional real vector, and \mathbf{p}, \mathbf{x} are M -dimensional real vectors with $\boldsymbol{\lambda} = (\mathbf{x}, \mathbf{p})$. For the measurement interactions treated in this paper, the generalized Fokker-Planck equation (GFPE) satisfied by a Q function is:

$$\dot{Q}(\boldsymbol{\lambda}, t) = \mathcal{L}(\boldsymbol{\lambda}) Q(\boldsymbol{\lambda}, t). \quad (10.4)$$

The differential operator $\mathcal{L}(\boldsymbol{\lambda})$ has first and second order differential terms $\mathcal{L}_1(\boldsymbol{\lambda})$ and $\mathcal{L}_2(\boldsymbol{\lambda})$, each with forward and backward components $\mathcal{L}_{np}(\mathbf{p})$, $\mathcal{L}_{jx}(\mathbf{x})$: so that:

$$\mathcal{L}(\boldsymbol{\lambda}) = \mathcal{L}_1(\boldsymbol{\lambda}) + \mathcal{L}_2(\boldsymbol{\lambda}) \quad (10.5)$$

$$= \sum_n [\mathcal{L}_{np}(\mathbf{p}) - \mathcal{L}_{nx}(\mathbf{x})], \quad (10.6)$$

where $\mathcal{L}_{jp,x}$ are defined as:

$$\mathcal{L}_{1p} = - \sum_j \partial_j^p a_p^j(\mathbf{p}) \quad (10.7)$$

$$\mathcal{L}_{2p} = \frac{1}{2} \sum_j \partial_j^p \partial_j^p d^j. \quad (10.8)$$

Here \mathcal{L}_x is identical to \mathcal{L}_p except for the substitution of x for p , and we define $\partial_j^p \equiv \partial/\partial p^j$, $\partial_j^x \equiv \partial/\partial x^j$. For the Hamiltonians in this paper, we have $\mathbf{a}_p = \mathbf{a}_p(\mathbf{p})$ and $\mathbf{a}_x = \mathbf{a}_x(\mathbf{x})$, with diagonal diffusion \mathbf{d} .

For use in the theorems proved below, we define a phase-space trajectory and stochastic path integral as follows. Firstly, the trajectory is a sequence $[\boldsymbol{\lambda}(t_0), \dots, \boldsymbol{\lambda}(t_N)] \equiv [\boldsymbol{\lambda}_0, \dots, \boldsymbol{\lambda}_N]$, with a total action of:

$$S_{kn} = S_{kn}^p + S_{kn}^x = \sum_{m=k+1}^n S_m. \quad (10.9)$$

The ‘‘one-step’’ action for the n -th step is given by $S_n = S_n^p + S_n^x$, with S_n^p having the same form as S_n^x except for the changed superscripts, where:

$$\begin{aligned} S_n^p &= S^p(\boldsymbol{\lambda}_{n-1}, \boldsymbol{\lambda}_n) \\ &= \sum_j \left[\frac{\epsilon}{2d^j} |v_n^{j,p}|^2 + \ln(\sqrt{\mathcal{N}^j}) \right]. \end{aligned} \quad (10.10)$$

This includes a path-integral normalization factor, $\mathcal{N}^j = (2\pi\epsilon d^j)$, and relative velocity fields $\mathbf{v} \equiv (\mathbf{v}^p, \mathbf{v}^x)$ which are functions of neighboring coordinates:

$$\begin{aligned} \mathbf{v}_n^p &\equiv \frac{1}{\epsilon} (\mathbf{p}_n - \mathbf{p}_{n-1}) - \mathbf{a}^p(\mathbf{p}_{n-1}) \\ \mathbf{v}_n^x &\equiv \frac{1}{\epsilon} (\mathbf{x}_{n-1} - \mathbf{x}_n) - \mathbf{a}^x(\mathbf{x}_n). \end{aligned} \quad (10.11)$$

The N -step total path probability \mathcal{P} for a path $\underline{\lambda} = (\lambda_0, \dots, \lambda_N)$ at times $t_k = t_0 + k\epsilon$, with $k = 0, \dots, N$, is

$$\mathcal{P}[\underline{\lambda}] = e^{-S_{0N}}. \quad (10.12)$$

The two-time propagator G is then defined as:

$$G(\underline{\lambda}, t_k | \tilde{\lambda}, \tilde{t}) = \lim_{\epsilon \rightarrow 0} \int \delta(\lambda - \lambda_k) \delta(\tilde{\lambda} - \lambda_{0N}) \mathcal{P}[\underline{\lambda}] d\underline{\lambda}. \quad (10.13)$$

Here, $d\underline{\lambda} = \prod_{n=0}^N d\lambda_n = \prod_{n=0}^N \prod_{k=1}^M dx_n^k dp_n^k$, $\lambda_{0N} = (\mathbf{x}_N, \mathbf{p}_0)$, while $\underline{\lambda} = (\mathbf{x}_f, \mathbf{p}_i)$ gives the initial momentum \mathbf{p}_i and final position \mathbf{x}_f at times $\tilde{t} = (t_i, t_f) = (t_0, t_N)$.

Marginals have the notation $P(\mathbf{x}, t) = \int Q(\underline{\lambda}, t) d\underline{\lambda}$, with the variables that are integrated removed from the arguments. Boundary conditions are imposed on the final marginal $P(\mathbf{x}, t_f)$ and initial conditional, $P(\mathbf{p} | \mathbf{x}, t_i) = Q(\underline{\lambda}, t_i) P^{-1}(\mathbf{x}, t_i)$. The remainder of this Section shows the equivalence of the differential and path-integral approaches, both analytically and numerically.

B. Path-integral equivalence theorems

Theorem I:

Any path-integral Q function Q_{pi} obtained from multiplication by the joint probabilities at the boundaries satisfies the Q function dynamical equations, where:

$$Q_{pi}(\underline{\lambda}, t) = \int G(\underline{\lambda}, t | \tilde{\lambda}, \tilde{t}) P(\tilde{\lambda}, \tilde{t}) d\tilde{\lambda}. \quad (10.14)$$

The quantum Q function solution, $Q = Q_{pi}$ is found on solving simultaneous equations for the joint distribution $P(\tilde{\lambda}, \tilde{t})$, and hence for Q_{pi} , where:

$$\int Q_{pi}(\underline{\lambda}, t_f) d\underline{\lambda} = P(\mathbf{x}, t_f), \quad (10.15)$$

and:

$$\frac{Q_{pi}(\underline{\lambda}, t_i)}{\int Q_{pi}(\underline{\lambda}, t_i) d\underline{\lambda}} = P(\mathbf{p} | \mathbf{x}, t_i). \quad (10.16)$$

Proof:

We wish to show that $Q_{pi} = Q$, by proving that Q_{pi} satisfies the GFPE (10.4), and has an initial condition that corresponds to the Q function for the initial quantum state. From linearity, proving that $Q_{pi}(\underline{\lambda})$ satisfies the GFPE 10.4 is achieved by verifying this for the propagator, $G(\underline{\lambda}, t | \tilde{\lambda}, \tilde{t})$. To show this, define advanced and retarded propagators for $\underline{\lambda}$ at $t = t_j$ with $\tilde{\mathbf{p}} = \mathbf{p}_0$ at

$t_i = t_0$ and $\tilde{\mathbf{x}} = \mathbf{x}_N$ at $t_f = t_N$, as

$$G^r(\mathbf{p}_j, t | \tilde{\mathbf{p}}, t_i) = \lim_{\epsilon \rightarrow 0} \int e^{-S_{0j}^p} \prod_{n=1}^{j-1} d\underline{\mathbf{p}}_n, \\ G^a(\mathbf{x}_j, t | \tilde{\mathbf{x}}, t_f) = \lim_{\epsilon \rightarrow 0} \int e^{-S_{jN}^x} \prod_{n=j+1}^{N-1} d\underline{\mathbf{x}}_n. \quad (10.17)$$

Due to its path-integral construction, G^r satisfies a forward Kolmogorov equation in \mathbf{p} [154, 155]. By reversing the sign of t , we find that G^a also satisfies a forward Kolmogorov equation in \mathbf{x} , but in the negative time direction:

$$\dot{G}^r(\mathbf{p}, t | \tilde{\mathbf{p}}, t_i) = \mathcal{L}^p G^r(\mathbf{p}, t | \tilde{\mathbf{p}}, t_i) \\ \dot{G}^a(\mathbf{x}, t | \tilde{\mathbf{x}}, t_f) = -\mathcal{L}^x G^a(\mathbf{x}, t | \tilde{\mathbf{x}}, t_f). \quad (10.18)$$

The normalization of the advanced Gaussian propagator terms in the path integral for \mathbf{x}_n with $n < j$ means that all these past time factors integrate to unity. Similarly, the retarded propagator is independent of \mathbf{p}_n for future time points $n > j$, as these also integrate to give unity. As a result, we can write that:

$$G^r(\mathbf{p}, t_k | \tilde{\mathbf{p}}, t_0) = \lim_{\epsilon \rightarrow 0} \int e^{-S_{0N}^p} \delta(\mathbf{p} - \mathbf{p}_k) \delta(\tilde{\mathbf{p}} - \mathbf{p}_0) d\underline{\mathbf{p}}, \\ G^a(\mathbf{x}, t_k | \tilde{\mathbf{x}}, t_f) = \lim_{\epsilon \rightarrow 0} \int e^{-S_{0N}^x} \delta(\mathbf{x} - \mathbf{x}_k) \delta(\tilde{\mathbf{x}} - \mathbf{x}_N) d\underline{\mathbf{x}}. \quad (10.19)$$

From these results and the definitions above, it follows that the total propagator factorizes as $G(\underline{\lambda}, t | \tilde{\lambda}, \tilde{t}) = G^r(\mathbf{p}, t | \tilde{\mathbf{p}}, t_0) G^a(\mathbf{x}, t | \tilde{\mathbf{x}}, t_f)$. Hence, using the chain rule for differentiation and Eq (10.18), the required time-evolution can be written as:

$$\dot{G}(\underline{\lambda}, t | \tilde{\lambda}) = \dot{G}^r(\mathbf{p}, t | \tilde{\mathbf{p}}, t_0) G^a(\mathbf{x}, t | \tilde{\mathbf{x}}, t_f) \\ + G^r(\mathbf{p}, t | \tilde{\mathbf{p}}, t_0) \dot{G}^a(\mathbf{x}, t | \tilde{\mathbf{x}}, t_f) \\ = (\mathcal{L}^p - \mathcal{L}^x) G(\underline{\lambda}, t | \tilde{\lambda}, \tilde{t}). \quad (10.20)$$

Due to linearity, any integral of G over its boundary values also satisfies the GFPE. Therefore, the path integral construction must obey the required GFPE,

$$\dot{Q}_{pi}(\underline{\lambda}, t) = (\mathcal{L}_p(\mathbf{p}) - \mathcal{L}_x(\mathbf{x})) Q_{pi}(\underline{\lambda}, t). \quad (10.21)$$

Provided the joint probability $P(\tilde{\lambda}, \tilde{t})$ satisfies the boundary equations, one can verify that at the initial time, $Q_{pi}(\underline{\lambda}, t_0) = Q(\underline{\lambda}, t_0)$. Due to uniqueness of the solutions to a first order differential equations, Q_{pi} is equal to the quantum-mechanical Q function solution for all times.

As a further check, in the short-time limit of $t_0 = t_f$ we find that

$$\lim_{t_0, t_f \rightarrow t} G(\underline{\lambda}, t | \tilde{\lambda}) = \delta(\underline{\lambda} - \tilde{\lambda}), \quad (10.22)$$

hence, as $t_0, t_f \rightarrow t$, one has that:

$$\begin{aligned} \lim_{t_0, t_f \rightarrow t} Q_{pi}(\boldsymbol{\lambda}, t) &= \int \delta(\boldsymbol{\lambda} - \tilde{\boldsymbol{\lambda}}) P(\tilde{\boldsymbol{\lambda}}, t') d\tilde{\boldsymbol{\lambda}}, \\ &= P(\mathbf{p}|\mathbf{x}, t') P(\mathbf{x}, t'). \end{aligned} \quad (10.23)$$

From the definition of the conditional probability, this is the initial Q function.

Theorem II:

The path-integral solution corresponds to a time-symmetric stochastic differential equation (TSSDE) or forward-backward SDE, with a conditional initial distribution in \mathbf{p} and final marginal distribution in \mathbf{x} :

$$\begin{aligned} p^j(t) &= p^j(t_0) + \int_0^t a_p^j(t') dt' + \int_0^t dw_p^j \\ x^j(t) &= x^j(t_f) + \int_t^{t_f} a_x^j(t') dt' + \int_t^{t_f} dw_x^j. \end{aligned} \quad (10.24)$$

Here $\mathbf{x}(t_f)$ is distributed as $P(\mathbf{x}, t_f)$, while $\mathbf{p}(t_0)$ is distributed conditionally as $C(\mathbf{p}|\mathbf{x}(t_0), t_0)$, and $[dw^\mu] = (d\mathbf{w}_x, d\mathbf{w}_p)$ are independent real Gaussian noises correlated as

$$\langle dw^\mu dw^\nu \rangle = \delta^{\mu\nu} d^\mu \epsilon, \quad (10.25)$$

where $\mu = 1, 2M$ and $d^{j+M} = d^j$.

Proof:

The TSSDE is obtained by discretizing the equation for times $t_k = t_0 + k\epsilon$, with $k = 0, \dots, N$, and then taking the limit of $\epsilon \rightarrow 0$. We define $[\boldsymbol{\lambda}] = [\boldsymbol{\lambda}_0, \boldsymbol{\lambda}_1, \dots, \boldsymbol{\lambda}_N]$ as the stochastic path. The discretized solutions are then given as the simultaneous solutions of the equations, for $k = 1, \dots, N$

$$\begin{aligned} \mathbf{p}_k &= \mathbf{p}_{k-1} + \mathbf{a}^p(\mathbf{p}_{k-1})\epsilon + \boldsymbol{\Delta}_k^p \\ \mathbf{x}_{k-1} &= \mathbf{x}_k + \mathbf{a}^x(\mathbf{x}_k)\epsilon + \boldsymbol{\Delta}_k^x, \end{aligned} \quad (10.26)$$

To obtain an equivalent path integral to the TSSDE, we first obtain the N -step trajectory probability density, conditioned on random noises $[\boldsymbol{\Delta}]$. This is a product of Dirac delta functions,

$$\mathcal{G}([\boldsymbol{\lambda}] | [\boldsymbol{\Delta}]) = \prod_{j=1}^n \delta^{2M}(\epsilon \mathbf{v}_j - \boldsymbol{\Delta}_j), \quad (10.27)$$

which gives a normalized probability conditioned on a specific noise vector $[\boldsymbol{\Delta}]$. Solving for the resulting set of trajectory values $[\boldsymbol{\lambda}]$ that satisfy the delta-function constraints is straightforward in the parametric amplifier case, due to the decoupling of forward and backward equations.

In a Fourier transform representation with $\mathbf{k}_j \equiv (k_j^1, k_j^2, \dots, k_j^{2M})$, one can expand the delta-functions as

$$\mathcal{G}_n([\boldsymbol{\lambda}] | [\boldsymbol{\Delta}]) = \prod_{j=1}^n \int \frac{d\mathbf{k}_j}{(2\pi)^{2M}} e^{-i\mathbf{k}_j(\mathbf{v}_j \epsilon - \boldsymbol{\Delta}_j)}. \quad (10.28)$$

The $2M$ real Gaussian noises $\boldsymbol{\Delta}_k$ at each step in time, for $k > 0$, are distributed as:

$$P(\boldsymbol{\Delta}_k) = \frac{1}{(2\pi\epsilon d)^M} e^{-|\boldsymbol{\Delta}_k|^2/(2\epsilon d)}. \quad (10.29)$$

On integration over \mathbf{k}_j one obtains the path probability result as defined previously:

$$\mathcal{G}_n([\boldsymbol{\lambda}]) = \int \mathcal{G}_n([\boldsymbol{\lambda}] | [\boldsymbol{\Delta}]) P([\boldsymbol{\Delta}]) d[\boldsymbol{\Delta}]. \quad (10.30)$$

By construction, the initial values of \mathbf{x}_N and \mathbf{p}_0 are sampled according to the required joint and conditional probabilities. Hence the probability of a TSSDE solution is Q_{pi} , which is equal to the quantum average Q from Theorem I. Our definitions are similar to those in the mathematics literature [156], except for the use of a conditional probabilistic boundary.

APPENDIX B: NUMERICAL χ^2 TESTS

The analytic theorems obtained in Section (X) were verified numerically using χ^2 tests in several cases described here, with details that are given below. The forward-backward stochastic equations were integrated by first propagating x backwards in time, generating a conditional sample, then propagating p forwards in time.

All trajectories plotted use 40 sample trajectories, to provide an intuitive demonstration of how they behave. In order to verify the quantitative accuracy of the trajectory probability distributions, large numbers of samples were generated and plotted using binning methods.

These samples were statistically tested with χ^2 methods [157, 158] to compare them with analytic solutions. The test cases used $N_s = 2 \times 10^6$ sample trajectories to obtain good statistics for the numerically sampled distributions,

$$p_{ijk}^{samp} = \frac{N_{ijk}}{N_s}. \quad (10.31)$$

Here N_{ijk} is the number of trajectories in the bin at x_i, p_j , and sampled time t_k . Such verification requires binning on a three-dimensional (x, p, t) grid, to obtain numerical estimates of the integrated analytic probabilities p_{ijk} , where:

$$p_{ijk} = \int_A d\delta x d\delta p Q(x_i + \delta x, p_j + \delta p, t_k). \quad (10.32)$$

This was evaluated by numerical integration of the analytic Q distribution, using a two-dimensional Simpson's rule integrator in each bin.

In order to treat the dynamics of the Q-function, time-averages were evaluated to give a definitive overall result. Due to the correlations inside each trajectory, the *range* of fluctuations of time-averaged statistics are reduced compared to one-time tests, which exactly follow the χ^2 distribution. Individual tests at each time-point are in agreement with χ^2 statistics, and will be reported elsewhere.

We therefore define:

$$\bar{\chi}^2 = \frac{1}{N_t} \sum_{i,j,k} \frac{\left\langle [p_{ijk} - p_{ijk}^{samp}]^2 \right\rangle}{\left\langle \sigma_{ijk}^2 \right\rangle}, \quad (10.33)$$

where,

$$\sigma_{ijk}^2 = p_{ijk}/N_s \quad (10.34)$$

is the expected probability variance for N_s total samples and N_t time points, with a phase-space bin area of A .

As an example, the simulations described in Figure (6) used 30 time-steps of $gdt = 0.1$, combined with a midpoint stochastic integration method for improved accuracy [159]. No significant discretization error improvements were found with smaller time-steps. Comparisons were made between the analytic and numerically sampled $Q(x, p, t)$ distributions with $dx = 0.02$ and $dp = 0.05$. This gave an average of $\sim 55,100$ comparison grid-points at each time step, after discarding bins with non-significant sample populations of $N < 10$ [160].

In a typical test with 2×10^6 sample trajectories and $A = 10^{-3}$, the time-averaged statistical error was $\bar{\chi}^2 = 55.2 \times 10^3$, with 1.7×10^6 valid comparisons. There were an average of $k = 55.1 \times 10^3$ significant points per time-step. This shows that $\bar{\chi}^2$ is within the expected range of $\langle \chi^2 \rangle = k \pm \sqrt{2k}$.

Hence, as expected from the path-integral and stochastic theorems, there is excellent agreement between the analytic Q-function probability from quantum theory and the ensemble averaged stochastic trajectories.

APPENDIX C: TRANSFORMATION IN Q FUNCTION DUE TO MEASUREMENT SETTINGS

The Q function $Q(\lambda_{rot}, t_1)$ of the new state at time t_1 after the interactions due to the H_θ and H_ϕ is that obtained by rotating the coordinates x_A, p_A, x_B, p_B in the original Q function, to new coordinates $x_{\theta A}, p_{\theta A}, x_{\phi B}, p_{\phi B}$. We see that

$$\alpha e^{i\theta} = (x_A + ip_A) e^{i\theta} = x'_A + ip'_A \quad (10.35)$$

where $x'_A = x_A \cos \theta - p_A \sin \theta$ and $p'_A = x_A \sin \theta + p_A \cos \theta$. To obtain the Q function at time t_1 , we hence transform an initial Q function $Q(x_A, p_A)$ by substituting α for $\alpha e^{i\theta}$, which means substituting x_A and p_A for x'_A and p'_A , i.e. $x_A \rightarrow x_A \cos \theta - p_A \sin \theta$ and $p_A \rightarrow p'_A =$

$x_A \cos \theta + p_A \sin \theta$ i.e. $x_A = x_{\theta A} \cos \theta - p_{\theta A} \sin \theta$ and $p_A = x_{\theta A} \sin \theta + p_{\theta A} \cos \theta$. The x_A and p_A in the rotated Q function are identified as $x_{\theta A}$ and $p_{\theta A}$, so that in terms of the original coordinates,

$$\begin{aligned} x_{\theta A} &= x_A \cos \theta + p_A \sin \theta \\ p_{\theta A} &= -x_A \sin \theta + p_A \cos \theta \end{aligned} \quad (10.36)$$

consistent with (8.1). Similarly, the change of setting at B induced by the interaction H_ϕ amounts to a rotation of coordinates

$$\begin{aligned} x_{\phi B} &= x_B \cos \phi + p_B \sin \phi \\ p_{\phi B} &= -x_B \sin \phi + p_B \cos \phi \end{aligned} \quad (10.37)$$

consistent with (8.2). Hence, the adjustment of measurement settings is carried out in the simulation by changing the Q function $Q(\lambda, t_0)$ to obtain a new Q function $Q(\lambda_{rot}, t_1)$ where $\lambda_{rot} = (x_{\theta A}, p_{\theta A}, x_{\phi B}, p_{\phi B})$.

APPENDIX D: STANDARD BELL EXAMPLE

Bell violations require adjustments of measurement settings θ and ϕ . It is worth reviewing the role of the measurement settings in standard Bell experiments. The choice of settings θ at A and ϕ at B involves interacting the systems locally with a physical device e.g. a Stern-Gerlach analyzer is orientated so that the spin component $\hat{\sigma}_\theta$ is measured at A and $\hat{\sigma}_\phi$ is measured at B .

We say that after passing through the analyzers, the systems A and B are *prepared with respect to the measurement basis*, for measurements $\hat{\sigma}_\theta$ and $\hat{\sigma}_\phi$ respectively. The Bell state is

$$|\psi_{bell}\rangle = \frac{1}{\sqrt{2}} \{ |+\rangle_A |-\rangle_B - |-\rangle_A |+\rangle_B \} \quad (10.38)$$

where $|\pm\rangle_K$, $K = A, B$, are the spin eigenstates of $\hat{\sigma}_z$ for the system denoted K . The probabilities for outcomes are calculated from (10.38), by rewriting $|\psi_{bell}\rangle$ in terms of the measurement basis, corresponding to the eigenstates of $\hat{\sigma}_{\theta, A}$ and $\hat{\sigma}_{\phi, B}$ (we take $\hat{\sigma}_\theta = \hat{\sigma}_z \cos \theta + \hat{\sigma}_x \sin \theta$). For example, the state after a single rotation ϕ at B is

$$\begin{aligned} |\psi_{bell}\rangle_\phi &= \frac{1}{\sqrt{2}} |+\rangle_A \{ \cos \frac{\phi}{2} |-\rangle_{\phi B} + \sin \frac{\phi}{2} |+\rangle_{\phi B} \} \\ &\quad - \frac{1}{\sqrt{2}} |-\rangle_A \{ -\sin \frac{\phi}{2} |-\rangle_{\phi B} + \cos \frac{\phi}{2} |+\rangle_{\phi B} \} \end{aligned} \quad (10.39)$$

where $|+\rangle_{\phi B} = \cos \frac{\phi}{2} |+\rangle + \sin \frac{\phi}{2} |-\rangle$ and $|-\rangle_{\phi B} = -\sin \frac{\phi}{2} |+\rangle + \cos \frac{\phi}{2} |-\rangle$. The probabilities for outcomes $+-, ++, --, -+$ are $\frac{1}{2} \cos^2 \frac{\phi}{2}$, $\frac{1}{2} \sin^2 \frac{\phi}{2}$, $\frac{1}{2} \sin^2 \frac{\phi}{2}$ and $\frac{1}{2} \cos^2 \frac{\phi}{2}$ respectively. We may compare with predictions for the non-entangled mixed state

$$\rho_{mix}^{(AB)} = \frac{1}{2} \{ |+\rangle_A |-\rangle_B \langle -|_B \langle +|_A + |-\rangle_A |+\rangle_B \langle +|_B \langle -|_A \} \quad (10.40)$$

The state after the rotation ϕ at B is

$$\rho_{mix,\phi} = \frac{1}{2}\{\rho_+^{(A)}\rho_{-\phi}^{(B)} + \rho_-^{(A)}\rho_{+\phi}^{(B)}\} \quad (10.41)$$

where $\rho_{\pm}^{(A)} = |\pm\rangle_A\langle\pm|_A$ and $\rho_{\pm\phi}^{(B)} = |\pm\rangle_{\phi B}\langle\pm|_{\phi B}$, which gives the *same* predictions for the probabilities as $|\psi_{bell}\rangle_{\phi}$.

However, after a *further* change of setting (basis) to θ at A , the predictions between the entangled and non-entangled states diverge. This is seen by writing both $|\psi_{bell}\rangle_{\phi}$ and $\rho_{mix,\phi}$ in the new basis for A , and is evident by the fact that $|\psi_{bell}\rangle$ violates the Bell inequality, whereas $\rho_{mix,AB}$ does not. The interference terms that are present in the density operator (when written in the original basis) for the Bell state $|\psi_{bell}\rangle$, but not for the mixed state $\rho_{mix}^{(AB)}$, do not manifest as a difference in predictions between $|\psi_{bell}\rangle$ and $\rho_{mix}^{(AB)}$ when there are no changes of settings, or only one change of setting. The violation of the Bell inequality requires a change of settings at both sites, A and B .

APPENDIX E: RETROCAUSAL MECHANISM FOR MEASUREMENT WITH A METER

We give an explicit example of calculation of a state $Q(x_B, p_B|\tilde{\lambda}_x^A)$ formed from the retrocausal feedback depicted in Figs. 5 and 26, which illustrates the collapse of the wavefunction with a meter. Consider the entangled state

$$|\psi_{ent}\rangle_{sq} = \frac{1}{\sqrt{2}}\{|\alpha_0\rangle|\frac{x_1}{2}, r\rangle_{sq} + i|-\alpha_0\rangle|-\frac{x_1}{2}, r\rangle_{sq}\}, \quad (10.42)$$

which becomes in the limit of large r

$$|\psi_{ent}\rangle = \frac{1}{\sqrt{2}}\{|\alpha_0\rangle|x_1\rangle + i|-\alpha_0\rangle|-x_1\rangle\}. \quad (10.43)$$

Here, $|\pm\alpha_0\rangle$ are coherent states for field mode A and $|\frac{x_1}{2}, r\rangle$ is the squeezed state for mode B defined by Eqs. (2.12) and (2.14). When α_0 is large, this entangled state models the state created when a macroscopic meter (field A) couples to a system B . The outcome of a measurement \hat{x} on system A gives (for α_0 real) the outcome of the sign of \hat{x} for system B . According to the measurement postulate, if the outcome for \hat{x} at A is positive then, for this superposition, the system B collapses to the eigenstate $|x_1\rangle$ (assuming r is large). We have evaluated the Q function for the system B conditioned on the positive outcome for A i.e. $Q(x_B, p_B|\tilde{\lambda}_x^A)$ where $\tilde{\lambda}_x^A > 0$. The Q function is plotted in Fig. 29.

APPENDIX F: FINE-TUNING

The simulations of this paper give a model in which no-signalling is explained consistently with observation

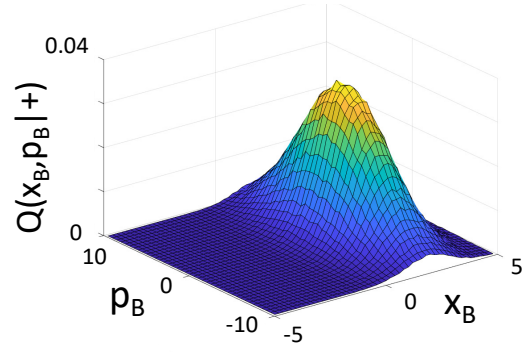


Figure 29. Measurement of \hat{x}_A for the system in the state (10.42). Plot of the inferred state $Q(x_B, p_B|\tilde{\lambda}_x^A) \equiv Q(x_B, p_B|+)$ for B conditioned on positive outcomes of \hat{x} on the meter A i.e. where $\tilde{\lambda}_x^A$ corresponds to the positive branch of \hat{x}_A . Here, we take $\alpha_0 = 2$, $x_1 = 2$ with $r = 1.5$ and 1.2×10^6 trajectories. Even for x_1 small, the Q function is that of $|x_1/2, r\rangle$.

of Bell nonlocality. The result does not however conflict with results that exclude classical causal models that are not fine-tuned: In Ref. [53], it is stated that an “*observed statistical independence between variables should not be explained by fine-tuning of the causal parameters*”.... “*In other words, all conditional independences (CIs) should be a consequence of the causal structure alone, not a result of the causal–statistical parameters taking some particular set of values.*” The authors of [53] showed that in order for a causal model to explain Bell violations consistently with no-signaling, it is necessary that there be a fine-tuning of the causal parameters. The causal parameters include the measurement settings θ and ϕ . The Ref. [53] considers, as an example, a possible superluminal influence from, say, the setting or outcome at one site to that of the other. “*Given the superluminal causal influences from one wing to the other, the only way to explain the lack of superluminal signals, is through a fine-tuning of the causal parameters.*”

We have seen that the simulations of this paper support **Result 4b**, which is the condition of no-signaling. An interaction H_ϕ^B (as in a change of setting) at B can change unobservable hidden terms in the Q function, without changing the outcome $\tilde{\lambda}_x^A$ for the setting $\theta \equiv 0$ (Fig. 27). This ensures no-signaling.

However, with an interaction H_θ^A at A so that $\theta \neq 0$ (i.e. over two rotations), Bell nonlocality can emerge (Fig. 28). Thus, no-signaling does not rule out Bell nonlocality. We see from the analysis of interference terms for the Bell state that specific values of θ and ϕ contribute to the observable probabilities that violate the Bell inequality. The value of θ needs to be adjusted from 0 in order to observe the nonlocality, consistent with the conclusions of Ref. [53]. However, it is not the case that there can be assumed to be no impact on A due to the change of setting at B , in the sense that there is a change

to the interference term in the Q function. We summarise with the following result.

Result 9: Fine-tuning: There is a fine-tuning of the causal parameters (the measurement settings) in order to observe the violation of the Bell inequality consistently with the observation of no-signalling.

Proof: No-signalling is defined as the condition that there is no change to the outcome of A due to a change of setting at B , with the setting at A fixed [53]. This corresponds to fixing the setting of θ at A , which we take without loss of generality to be $\theta = 0$ so that we assume \hat{x} is measured at A (as in Figs. 25-27). **Result 4b** states that the outcome given by $\tilde{\lambda}_x^A$ in the model is unchanged as the setting ϕ at B is changed. In order to detect Bell nonlocality, the simulations (**Result 8**) show that we require to adjust to a nonzero setting $\theta \neq 0$ at A (Fig. 28). Hence, a fine-tuning of the causal parameters

is required. \square

We have been able to explain how the no-signalling arises in the simulation: The no-signaling does not occur due to an engineered cancelation of correlations arising from different causal mechanisms. In explaining the desire to establish a causal model that does not require fine-tuning, the authors of Ref. [53] explain with reference to Figure 5 of their paper that: “...there are two causal mechanisms by which A and B could become correlated, and it could be that the two types of correlations combine in such a way as to leave A and B marginally independent. For this to happen, however, the parameters in the causal model cannot be chosen arbitrarily and it is in this sense that the explanation is less natural”. We are able to confirm from our simulation that the observed conditional independence of no-signaling does not occur due to such a cancellation.

-
- [1] J. S. Bell, Phys. **1**, 195 (1964).
 - [2] N. Brunner, D. Cavalcanti, S. Pironio, V. Scarani, and S. Wehner, Rev. Mod. Phys. **86**, 419 (2014).
 - [3] J. F. Clauser and A. Shimony, Rep. Prog. Phys. **41**, 1881 (1978).
 - [4] J. S. Bell, *Speakable and unspeakable in quantum mechanics: Collected papers on quantum philosophy* (Cambridge University Press, 2004).
 - [5] D. Pegg, Phys. Lett. A **78**, 233 (1980).
 - [6] J. G. Cramer, Phys. Rev. D **22**, 362 (1980).
 - [7] D. T. Pegg, Physica Scripta **1986**, 14 (1986).
 - [8] J. G. Cramer, Rev. Mod. Phys. **58**, 647 (1986).
 - [9] K. Schwarzschild, Nachrichten von der Gesellschaft der Wissenschaften zu Göttingen, Mathematisch-Physikalische Klasse **1903**, 132 (1903).
 - [10] A. D. Fokker, Zeitschrift für Physik **58**, 386 (1929).
 - [11] H. M. Tetrode, Zeitschrift für Physik **10**, 317 (1922).
 - [12] P. A. M. Dirac, Rev. Mod. Phys. **17**, 195 (1945).
 - [13] J. A. Wheeler and R. P. Feynman, Rev. Mod. Phys. **17**, 157 (1945).
 - [14] J. A. Wheeler and R. P. Feynman, Rev. Mod. Phys. **21**, 425 (1949).
 - [15] N. Bohr, *Essays 1958-1962 on Atomic Phys. and Human Knowledge*, Bohr, Niels: Philosophical writings, Vol. 3 (Ox Bow Press, Woodbridge, USA, 1987).
 - [16] X.-s. Ma, J. Kofler, and A. Zeilinger, Rev. Mod. Phys. **88**, 015005 (2016).
 - [17] J. A. Wheeler, in *Mathematical foundations of quantum theory* (Elsevier, 1978) pp. 9–48.
 - [18] J. A. Wheeler and W. H. Zurek, *Quantum theory and measurement*, Vol. 40 (Princeton University Press, 2014).
 - [19] P. H. Eberhard and R. R. Ross, Foundations of Phys. Lett. **2**, 127 (1989).
 - [20] Y. Aharonov, P. G. Bergmann, and J. L. Lebowitz, Phys. Rev. **134**, B1410 (1964).
 - [21] M. O. Scully and K. Drühl, Phys. Rev. A **25**, 2208 (1982).
 - [22] M. O. Scully, B.-G. Englert, and H. Walther, Nature **351**, 111 (1991).
 - [23] U. Mohrhoff, Am. J. Phys. **64**, 1468 (1996).
 - [24] B.-G. Englert, M. O. Scully, and H. Walther, Am. J. Phys. **67**, 325 (1999).
 - [25] Y.-H. Kim, R. Yu, S. P. Kulik, Y. Shih, and M. O. Scully, Phys. Rev. Lett. **84**, 1 (2000).
 - [26] S. P. Walborn, M. O. T. Cunha, S. Pádua, and C. H. Monken, Phys. Rev. A **65**, 033818 (2002).
 - [27] V. Jacques, E. Wu, F. Grosshans, F. Treussart, P. Grangier, A. Aspect, and J.-F. Roch, Science **315**, 966 (2007).
 - [28] H. Price, Studies in History and Philosophy of Science Part B: Studies in History and Philosophy of Modern Phys. **39**, 752 (2008).
 - [29] N. Argaman, American Journal of Physics **78**, 1007 (2010).
 - [30] Y. Aharonov and L. Vaidman, Time in quantum mechanics , 399 (2008).
 - [31] R. Ionicioiu and D. R. Terno, Phys. Rev. Lett. **107**, 230406 (2011).
 - [32] J.-S. Tang, Y.-L. Li, X.-Y. Xu, G.-Y. Xiang, C.-F. Li, and G.-C. Guo, Nature Photonics **6**, 600 (2012).
 - [33] A. Peruzzo, P. Shadbolt, N. Brunner, S. Popescu, and J. L. O’Brien, Science **338**, 634 (2012).
 - [34] F. Kaiser, T. Coudreau, P. Milman, D. B. Ostrowsky, and S. Tanzilli, Science **338**, 637 (2012).
 - [35] X.-S. Ma, J. Kofler, A. Qarry, N. Tetik, T. Scheidl, R. Ursin, S. Ramelow, T. Herbst, L. Ratschbacher, A. Fedrizzi, *et al.*, Proceedings of the National Academy of Sciences **110**, 1221 (2013).
 - [36] R. Ionicioiu, T. Jennewein, R. B. Mann, and D. R. Terno, Nature Communications **5**, 1 (2014).
 - [37] A. G. Manning, R. I. Khakimov, R. G. Dall, and A. G. Truscott, Nature Phys. **11**, 539 (2015).
 - [38] S.-B. Zheng, Y.-P. Zhong, K. Xu, Q.-J. Wang, H. Wang, L.-T. Shen, C.-P. Yang, J. M. Martinis, A. N. Cleland, and S.-Y. Han, Phys. Rev. Lett. **115**, 260403 (2015).
 - [39] R. Chaves, G. B. Lemos, and J. Pienaar, Phys. Rev. Lett. **120**, 190401 (2018).
 - [40] R. Rossi Jr, Phys. Rev. A **96**, 012106 (2017).
 - [41] A. S. Rab, E. Polino, Z.-X. Man, N. Ba An, Y.-J. Xia, N. Spagnolo, R. Lo Franco, and F. Sciarrino, Nature Communications **8**, 1 (2017).

- [42] W. Qin, A. Miranowicz, G. Long, J. Q. You, and F. Nori, *npj Quantum Information* **5**, 1 (2019).
- [43] E. Polino, I. Agresti, D. Poderini, G. Carvacho, G. Milani, G. B. Lemos, R. Chaves, and F. Sciarrino, *Phys. Rev. A* **100**, 022111 (2019).
- [44] R. Kastner, *Foundations of Phys.* **49**, 717 (2019).
- [45] H.-L. Huang, Y.-H. Luo, B. Bai, Y.-H. Deng, H. Wang, Q. Zhao, H.-S. Zhong, Y.-Q. Nie, W.-H. Jiang, X.-L. Wang, *et al.*, *Phys. Rev. A* **100**, 012114 (2019).
- [46] S. Yu, Y.-N. Sun, W. Liu, Z.-D. Liu, Z.-J. Ke, Y.-T. Wang, J.-S. Tang, C.-F. Li, and G.-C. Guo, *Phys. Rev. A* **100**, 012115 (2019).
- [47] K. B. Wharton and N. Argaman, *Rev. Mod. Phys.* **92**, 021002 (2020).
- [48] B. R. La Cour and T. W. Yudichak, *Phys. Rev. A* **103**, 062213 (2021).
- [49] M. Thenabadu and M. D. Reid, *Phys. Rev. A* **105**, 062209 (2022).
- [50] T. J. Herzog, P. G. Kwiat, H. Weinfurter, and A. Zeilinger, *Phys. Rev. Lett.* **75**, 3034 (1995).
- [51] O. Oreshkov, F. Costa, and Č. Brukner, *Nature Communications* **3**, 1 (2012).
- [52] R. Chaves and T. Fritz, *Phys. Rev. A* **85**, 032113 (2012).
- [53] C. J. Wood and R. W. Spekkens, *New J. Phys.* **17**, 033002 (2015).
- [54] E. G. Cavalcanti, *Phys. Rev. X* **8**, 021018 (2018).
- [55] J. C. Pearl and E. G. Cavalcanti, arXiv preprint arXiv:1909.05434 (2019).
- [56] J. Pearl and E. Cavalcanti, *Quantum* **5**, 518 (2021).
- [57] F. Costa and S. Shrapnel, *New J. Phys.* **18**, 063032 (2016).
- [58] J.-M. A. Allen, J. Barrett, D. C. Horsman, C. M. Lee, and R. W. Spekkens, *Phys. Rev. X* **7**, 031021 (2017).
- [59] S. Shrapnel and F. Costa, *Quantum* **2**, 63 (2018).
- [60] S. Shrapnel, *The British Journal for the Philosophy of Science* **70**, 1 (2019).
- [61] J. Barrett, R. Lorenz, and O. Oreshkov, *Nature Communications* **12**, 1 (2021).
- [62] J. Pienaar, *Phys. Rev. A* **101**, 012104 (2020).
- [63] J.-M. A. Allen, J. Barrett, D. C. Horsman, C. M. Lee, and R. W. Spekkens, *Phys. Rev. X* **7**, 031021 (2017).
- [64] M. Weilenmann and R. Colbeck, *Quantum* **4**, 236 (2020).
- [65] G. Chiribella, *Phys. Rev. A* **86**, 040301(R) (2012).
- [66] G. Chiribella, G. M. D'Ariano, P. Perinotti, and B. Valiron, *Physical Review A* **88**, 022318 (2013).
- [67] F. A. Pollock, C. Rodríguez-Rosario, T. Frauenheim, M. Paternostro, and K. Modi, *Phys. Rev. Lett.* **120**, 040405 (2018).
- [68] M. Araújo, F. Costa, and Č. Brukner, *Phys. Rev. Lett.* **113**, 250402 (2014).
- [69] M. Araújo, C. Branciard, F. Costa, A. Feix, C. Giarmatzi, and Č. Brukner, *New J. Phys.* **17**, 102001 (2015).
- [70] O. Oreshkov and C. Giarmatzi, *New J. Phys.* **18**, 093020 (2016).
- [71] C. Giarmatzi, in *Rethinking Causality in Quantum Mechanics* (Springer, 2019) pp. 125–150.
- [72] M. Gachechiladze, N. Miklin, and R. Chaves, *Phys. Rev. Lett.* **125**, 230401 (2020).
- [73] P. J. Daley, K. J. Resch, and R. W. Spekkens, *Phys. Rev. A* **105**, 042220 (2022).
- [74] M. Araújo, P. A. Guérin, and Ä. Baumeler, *Physical Review A* **96**, 052315 (2017).
- [75] K. Wharton, *Information* **5**, 190 (2014).
- [76] S. Weinstein, arXiv preprint arXiv:1707.03114 (2017).
- [77] J. Barrett, R. Lorenz, and O. Oreshkov, arXiv preprint arXiv:1906.10726 (2019).
- [78] D. Bohm, *Phys. Rev.* **85**, 166 (1952).
- [79] W. Struyve, *Rep. Prog. Phys.* **73**, 106001 (2010).
- [80] B. F. Toner and D. Bacon, *Phys. Rev. Lett.* **91**, 187904 (2003).
- [81] V. Scarani, J.-D. Bancal, A. Suarez, and N. Gisin, *Foundations of Phys.* **44**, 523 (2014).
- [82] J.-D. Bancal, S. Pironio, A. Acín, Y.-C. Liang, V. Scarani, and N. Gisin, *Nature Physics* **8**, 867 (2012).
- [83] W. Struyve and H. Westman, *Proceedings of the Royal Society A: Mathematical, Physical and Engineering Sciences* **463**, 3115 (2007).
- [84] K. B. Wharton, *Foundations of Physics* **40**, 313 (2010).
- [85] K. Wharton, *Entropy* **20**, 10.3390/e20060410 (2018).
- [86] S. Donati and S. Hossenfelder, *Phys. Rev. A* **106**, 022212 (2022).
- [87] D. Almada, K. Ch'ng, S. Kintner, B. Morrison, and K. Wharton, *Int. J. Quant. Found* **2**, 1 (2016).
- [88] R. I. Sutherland, *Studies in History and Philosophy of Science Part B: Studies in History and Philosophy of Modern Physics* **39**, 782 (2008).
- [89] H. Price, *Time's arrow & Archimedes' point: new directions for the physics of time* (Oxford University Press, USA, 1996).
- [90] V. Vilasini and R. Colbeck, *Physical Review A* **106**, 032204 (2022).
- [91] V. Vilasini and R. Colbeck, *Physical Review Letters* **129**, 110401 (2022).
- [92] G. Castagnoli, *Phys. Rev. A* **104**, 032203 (2021).
- [93] G. Castagnoli, *Foundations of Physics* **48**, 333 (2018).
- [94] G. Castagnoli, E. Cohen, A. Ekert, and A. Elitzur, *Foundations of Physics* **49**, 1200 (2019).
- [95] S. Hossenfelder and T. Palmer, *Frontiers in Phys.* **8**, 139 (2020).
- [96] A. J. Leggett and A. Garg, *Phys. Rev. Lett.* **54**, 857 (1985).
- [97] M. Thenabadu and M. D. Reid, *Phys. Rev. A* **105**, 052207 (2022).
- [98] E. Schrödinger, *Naturwissenschaften* **23**, 823 (1935).
- [99] K. Husimi, *Proc. Physical Math. Soc. Jpn.* **22**, 264 (1940).
- [100] R. J. Glauber, in *Frontiers in Quantum Optics*, Malvern Physics Series, Vol. 534, edited by E. Pike and S. Sarkar (Adam Hilger, Bristol and Boston, 1986).
- [101] A. Einstein, B. Podolsky, and N. Rosen, *Phys. Rev.* **47**, 777 (1935).
- [102] M. D. Reid, P. D. Drummond, W. P. Bowen, E. G. Cavalcanti, P. K. Lam, H. A. Bachor, U. L. Andersen, and G. Leuchs, *Rev. Mod. Phys.* **81**, 1727 (2009).
- [103] P. Colciaghi, Y. Li, P. Treutlein, and T. Zibold, *Physical Review X* **13**, 021031 (2023).
- [104] P. D. Drummond and M. D. Reid, *Phys. Rev. Research* **2**, 033266 (2020).
- [105] P. D. Drummond and M. D. Reid, *Entropy* **23**, 749 (2021).
- [106] P. D. Drummond, *Phys. Rev. Research* **3**, 013240 (2021).
- [107] S. Friederich, *The British Journal for the Philosophy of Science* **0**, null (2021), <https://doi.org/10.1086/716196>.
- [108] J. Bell, *Phys. world* **3**, 33 (1990).
- [109] G. C. Knee, K. Kakuyanagi, M.-C. Yeh, Y. Matsuzaki, H. Toida, H. Yamaguchi, S. Saito, A. J. Leggett, and

- W. J. Munro, *Nature Communications* **7**, 1 (2016).
- [110] H.-Y. Ku, N. Lambert, F.-J. Chan, C. Emary, Y.-N. Chen, and F. Nori, *npj Quantum information* **6**, 98 (2020).
- [111] H. Jeong, M. Paternostro, and T. C. Ralph, *Phys. Rev. Lett.* **102**, 060403 (2009).
- [112] M. Thenabadu, G.-L. Cheng, T. L. H. Pham, L. V. Drummond, L. Rosales-Zárate, and M. D. Reid, *Phys. Rev. A* **102**, 022202 (2020).
- [113] J. Fulton, M. Thenabadu, R. Y. Teh, and M. D. Reid, *Entropy* **26**, 10.3390/e26010011 (2024).
- [114] D. Deutsch, *Physical Review D* **44**, 3197 (1991).
- [115] M. Ringbauer, M. A. Broome, C. R. Myers, A. G. White, and T. C. Ralph, *Nature Communications* **5**, 1 (2014).
- [116] J. Fulton, R. Y. Teh, and M. Reid, *Physical Review A* **110**, 022218 (2024).
- [117] R. R. Joseph, M. Thenabadu, C. Hatharasinghe, J. Fulton, R.-Y. Teh, P. Drummond, and M. Reid, *Physical Review A* **110**, 022219 (2024).
- [118] H. P. Yuen, *Phys. Rev. A* **13**, 2226 (1976).
- [119] R. R. Joseph, L. E. Rosales-Zárate, and P. D. Drummond, *J. Phys. A* **51**, 245302 (2018).
- [120] L. E. C. Rosales-Zárate and P. D. Drummond, *New J. Phys.* **17**, 032002 (2015).
- [121] M. Brune *et al.*, *Phys. Rev. Lett.* **77**, 4887 (1996).
- [122] M. D. Reid and P. D. Drummond, Einstein-podolsky-rosen-bell correlations with forward-backward stochastic phase-space simulations, arXiv:2303.02373 (2023).
- [123] B. Yurke and D. Stoler, *Phys. Rev. Lett.* **57**, 13 (1986).
- [124] L.-A. Wu, H. Kimble, J. Hall, and H. Wu, *Physical Review Letters* **57**, 2520 (1986).
- [125] B. Yurke, L. R. Corruccini, P. G. Kaminsky, L. W. Rupp, A. D. Smith, A. H. Silver, R. W. Simon, and E. A. Whittaker, *Phys. Rev. A* **39**, 2519 (1989).
- [126] M. Raymer and S. Yang, *Journal of Modern Optics* **39**, 1221 (1992).
- [127] P. D. Drummond and M. Hillery, *The quantum theory of nonlinear optics* (Cambridge University Press, 2014).
- [128] G. J. Milburn and C. A. Holmes, *Phys. Rev. Lett.* **56**, 2237 (1986).
- [129] R. R. Joseph, P. D. Drummond, and L. E. C. Rosales-Zárate, *Phys. Rev. A* **104**, 062208 (2021).
- [130] F. Fröwis, P. Sekatski, W. Dür, N. Gisin, and N. Sangouard, *Rev. Mod. Phys.* **90**, 025004 (2018).
- [131] C. Emary, N. Lambert, and F. Nori, *Rep. Prog. Phys.* **77**, 016001 (2013).
- [132] M. D. Reid, *J. Phys. A* **50**, 41LT01 (2017).
- [133] E. G. Cavalcanti and M. D. Reid, *Phys. Rev. A* **77**, 062108 (2008).
- [134] M. D. Reid, *Phys. Rev. A* **40**, 913 (1989).
- [135] U. Leonhardt and J. A. Vaccaro, *Journal of Modern Optics*, *Journal of Modern Optics* **42**, 939 (1995).
- [136] A. Gilchrist, P. Deuar, and M. D. Reid, *Phys. Rev. Lett.* **80**, 3169 (1998).
- [137] A. Gilchrist, P. Deuar, and M. D. Reid, *Phys. Rev. A* **60**, 4259 (1999).
- [138] K. Banaszek and K. Wódkiewicz, *Phys. Rev. Lett.* **82**, 2009 (1999).
- [139] M. F. Pusey, J. Barrett, and T. Rudolph, *Nature Phys.* **8**, 475 (2012).
- [140] Č. Brukner, *Nature Reviews Physics* **4**, 628 (2022).
- [141] M. J. Hall, *Physical Review A* **110**, 022209 (2024).
- [142] D. Frauchiger and R. Renner, *Nature communications* **9**, 3711 (2018).
- [143] K.-W. Bong, A. Utreras-Alarcón, F. Ghafari, Y.-C. Liang, N. Tischler, E. G. Cavalcanti, G. J. Pryde, and H. M. Wiseman, *Nature Phys.* **16**, 1199 (2020).
- [144] C. Hatharasinghe, M. Thenabadu, P. D. Drummond, and M. D. Reid, *Entropy* **25**, 1620 (2023).
- [145] A. Ourjoumtsev, H. Jeong, R. Tualle-Brouiri, and P. Grangier, *Nature* **448**, 784 (2007).
- [146] C. Monroe, D. M. Meekhof, B. E. King, and D. J. Wineland, *science* **272**, 1131 (1996).
- [147] Z. Leghtas, G. Kirchmair, B. Vlastakis, M. H. Devoret, R. J. Schoelkopf, and M. Mirrahimi, *Physical Review A—Atomic, Molecular, and Optical Physics* **87**, 042315 (2013).
- [148] T. Palomaki, J. Teufel, R. Simmonds, and K. W. Lehnert, *Science* **342**, 710 (2013).
- [149] A. Omran, H. Levine, A. Keesling, G. Semeghini, T. T. Wang, S. Ebadi, H. Bernien, A. S. Zibrov, H. Pichler, S. Choi, *et al.*, *Science* **365**, 570 (2019).
- [150] E. Wright, D. Walls, and J. Garrison, *Phys. Rev. Lett.* **77**, 2158 (1996).
- [151] O. Landon-Cardinal, L. C. G. Govia, and A. A. Clerk, *Phys. Rev. Lett.* **120**, 090501 (2018).
- [152] N. Wiener, *Acta mathematica* **55**, 117 (1930).
- [153] R. Graham, *Zeitschrift für Physik B* **26**, 397 (1977).
- [154] R. Stratonovich, *SIAM J. Control* **4**, 362 (1966).
- [155] R. Graham, *Zeitschrift für Physik B* **26**, 281 (1977).
- [156] J. Ma, P. Protter, and J. Yong, *Probability theory and related fields* **98**, 339 (1994).
- [157] K. Pearson, *The London, Edinburgh, and Dublin Philosophical Magazine and Journal of Science* **50**, 157 (1900).
- [158] P. D. Drummond, B. Opanchuk, A. Dellios, and M. D. Reid, *Phys. Rev. A* **105**, 012427 (2022).
- [159] P. D. Drummond and I. K. Mortimer, *J. Comput. Phys.* **93**, 144 (1991).
- [160] A. L. Rukhin, J. Soto, J. R. Nechvatal, M. E. Smid, E. B. Barker, S. D. Leigh, M. Levenson, M. Vangel, D. L. Banks, *et al.*, *A statistical test suite for random and pseudorandom number generators for cryptographic applications*, Tech. Rep. (2010).